THE EFFECTS OF DYNAMIC CAPILLARY PRESSURE ON TWO-PHASE FLOW AND BLOB MOBILIZATION IN POROUS MEDIA

by

Shao-Yiu Hsu

A dissertation submitted to The Johns Hopkins University in conformity with the requirements for the degree of Doctor of Philosophy.

Baltimore, Maryland

April, 2012

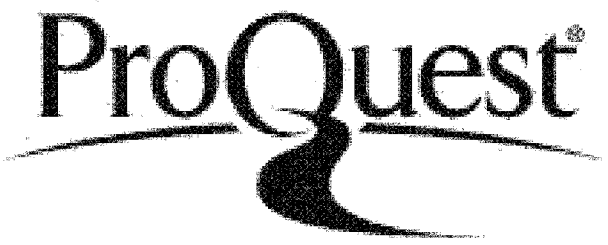

ProQuest LLC
789 East Eisenhower Parkway
P.O. Box 1346
Ann Arbor, MI 48106-1346

Abstract

Studies have shown that, in porous media, contact angles can be vary due to contact angle hysteresis, and capillary pressure could be dynamic during the processes of drainage and imbibition. The research presented here examined the effect of contact angle hysteresis and dynamic capillary pressure on multiscale two-phase flow in porous media. This dissertation is composed of three essays: "Pore-scale analysis of the effects of contact angle hysteresis on blob mobilization in a pore doublet," "Theoretical and experimental study of resonance of blobs in porous media," and "Incorporation of dynamic capillary pressure into the Green-Ampt model for infiltration."

The first essay focuses on the Jamin effect which is the main barrier to the mobilization of residual blobs in porous media. Experiments performed within a model pore doublet showed that the Jamin effect on a blob can be explained entirely through contact angle hysteresis. A blob is able to sustain pressure gradients by changing its interfacial shape and contact angles while maintaining its contact line position. The sustained pressure gradient was not only directly measured with pressure transducers but also well predicted by the theory. We also developed methods to measure contact angles and mean interfacial curvatures in three dimensions.

In the second essay, we propose a theoretical model supported by experimental data describing the frequency response of blobs in porous media subjected to an oscillatory pressure difference. The simple model pore system consists of a blob in a capillary tube and accounts for frequency-dependent viscous pressure drops in the blob and in the surrounding liquid. In this model, the capillary pressure is variable due to contact line pinning. Using the planar laser-induced fluorescence technique, the dynamic response of blobs in porous media was visualized in a series of two-dimensional cross-sectional images. In a capillary tube, both air and liquid blobs exhibited resonance as predicted by the model. Furthermore, for the first time, the experimental results showed that a liquid blob in a sphere-packing medium exhibits resonance.

The third essay proposes a modified Green-Ampt model to account for a capillary pressure that depends on the flow velocity. A functional form for dynamic capillary pressure is postulated, based on dimensional analysis and physical considerations. In this form, the nonequilibrium capillary pressure is assumed to depend on the capillary number according to a power law. This model for dynamic capillary pressure describes previously published measurements of capillary pressure versus Darcy velocity. In addition, by using dimensional analysis, the three dynamic capillary pressure curves measured by Geiger and Durnford (Soil Sci. Soc. Am. J., 2000) in sand columns of different grain size are collapsed onto a single curve. The model also describes Tabuchi's capillary rise experiments (Rec. Land Reclam. Res., 1971) well. An implicit analytical solution was also derived for calculating the front velocity.

Committee Chair: Professor Andrea Prosperetti

Advisor: Associate Professor Markus Hilpert

Reader: Professor Joseph Katz

Acknowledgments

"How to find a right Ph.D. advisor?", I asked.

"How did you find your wife?", Charlie O'Melia replied.

Six years ago, I was very lucky that a conversation with Dr. O'Melia lead me to work with my advisor, Markus Hilpert, and joined his research group. I would like to express my sincere gratitude to him for his guidance, encouragement, and support throughout the journey of pursuit my Ph.D. degree. During this journey, his patience give me a chance to learn scientific writing from him when we sat together to revised my paper sentence by sentence, his critiques push me to think deep for my research when I indulged myself in some immature results, his knowledge lead me go through these difficulties one after one, and his kindness help me to balance my life between school and home after my wife gave birth to my daughter.

I would like to thank Dr. Joseph Katz for his invaluable advise to build up my entire experimental setup. I would like to thank Drs. Andrea Prosperetti, Mark Robbins, Charles O'Melia, Peter Wilcock, Benjamin Hobbs, and Kai Loon Chen for serving on my thesis, GBO, and DQE committee. Their suggestions and comments are greatly appreciated.

I would like to thank Dr. William Ball and Dr. Avishai Ben-David for borrowing me their expensive equipments: syringe pumps and a He-Ne laser. Without their help, I won't

finish most part of my experiments.

I would like to thank Mr. Yury Rhonzes and Mr. Walter Krug for their assistant to design and build the acrylic flow cells. Mr. Walter were always able to fixed my flow cells.

I thank Dr. Roland Glantz for assistance and suggestions on the image analysis and Matlab coding. I greatly benefited from our many discussions. I thank the Hilpert group members, both past and present. Elizabeth, Wei, Yaqi, Zhi Feng have all shared their precious research experience, Matlab/Latex tricks, and many funny stories.

The whole DoGEE department, professors, students, the staff from the front office and especially the members of the DoGEE softball team deserve a warmest thanks for all the assistance and joyful time together. In addition, I especially thank my DoGEE colleagues, Jessica Lawson, Rebecca Murphy, Kathryn Onesios for proof reading my dissertation. Appreciation is extended to my Taiwanese friend in JHU! Yihsu, Ming-Che, Jim Yu, Su-Hsin,Yung-Li, Tim, An Ch, and Yi-Ping.

Finally, I thank my family for all their love and encouragement. Especially my wife, Chi-Fang, without her, I can not finish my Ph.D. degree and enjoy my parenthood with my daughter, Alisa, at same time.

This work is supported by the National Science Foundation Grant EAR-0739038 and Ministry of Education of Taiwan "Study Abroad"

Contents

List of Tables

List of Figures

Chapter 1. Introduction

1.1 Motivation

The migration of non-aqueous phase liquids (NAPLs) in the subsurface is a multiphase flow process that is relevant to groundwater contamination and remediation, and to oil recovery. During NAPL migration, liquid blobs are left behind, trapped in some of the pores and fractures. This remaining NAPL is said to be at residual saturation. The residual saturation of a NAPL is a function of porous medium and liquid properties and varies from 0.71% to 60% [22]. Since NAPLs in the subsurface will slowly dissolve into groundwater, and since their solubility is typically more than two orders of magnitude higher than their maximum contaminant levels (MCLs) in drinking water, the presence of NAPLs affects groundwater quality and poses a great risk to human health [32]. Furthermore, their low aqueous solubility means they can remain in the subsurface for a long time while continuously contaminating groundwater.

The goal of this dissertation is to improve the understanding of mobilization of NAPL blobs and multiphase flow in porous media. We paid particular attention to the effects of variable contact angles which may be due to contact angle hysteresis or a non-zero velocity of the three-phase contact line. The following sections present background material for this thesis which deals with the Jamin effect (related to blob mobilization), the resonance

of NAPL blobs in porous media, and the infiltration of liquids into dry soil, all of which are related to a non-constant contact angle. This introduction also provides some background on flow visualization in porous media, a technique used in this research to image two-fluid flow and to infer contact angles from the images.

1.2 The Jamin effect and the NAPL residual blobs

Jamin effect is the observed phenomenon where blobs in porous media can resist pressure gradients in the surrounding liquid, even in a cylindrical capillary tube. Taber [52] pointed out that the trapping of residual blobs is due to this Jamin effect. Smith and Crane [50] suspected that the maximum or critical pressure that blobs in a capillary tube can sustain without moving is a function of the tube radius, the interfacial tension, the advancing, and receding contact angles.

The traditional technology used to clean up NAPL-contaminated groundwater involves pumping the water to the surface and then treating it [27]. The action of pumping water generates a pressure gradient that can potentially be used to mobilize the funicular NAPL liquid and the residual NAPL blobs. In a packing of uniform spheres, Melrose and Brandner [30] theoretically predicted that the critical pressure gradient needed to remobilize a trapped blob is related to the radius of the spherical particles, the length of the blob in the flow direction, and the critical total curvatures of the blob's downstream and upstream menisci (fluid-fluid interfaces). By assuming contact angles of zero, Melrose and Brandner [30] linked the critical pressure gradient to the corresponding critical capillary

number. Ng et al. [35] expressed the critical capillary number as a function of the average pore-throat radius, the average pore-body radius, and the effective permeability of the porous medium.

In the past decades, Melrose and Brandner [30]'s and Ng et al. [35]'s theories have been used to study immiscible flow and blob mobilization in the subsurface in order to examine methods that enhance oil recovery (EOR) and groundwater remediation. These methods include surfactant flushing, polymer flooding, and vibratory or acoustical enhancement [31, 45, 42, 26, 6]. However, most studies treated the contact angle as constant or even assumed a contact angle of zero.

The link between the Jamin effect and blob mobilization has also been experimentally investigated. Both Smith and Crane [50] and Gardescu [14] performed experiments to show the Jamin effect and suggested that it is related to contact angle hysteresis. The experiments in a single glass tube done by Dong et al. [12] examined the change of the pressure drop during the mobilization of a nonwetting oil blob. They attributed the Jamin effect to the viscous pressure drop of slug flow. However, the studies mentioned above neither measured contact angles nor compared the constant pressure drop to the calculated pressure drop. Thus contact angle hysteresis has not been directly proven to be the sole cause of the Jamin effect in a straight capillary tube.

Since the 1960s, studies on blob mobilization primarily have focused on the effects of interfacial tension, pressure gradient, liquid density, and pore geometry. Although contact angle hysteresis tends to increase the capillary forces and the difficulty of mobilizing

trapped blobs [34], experiments such as those reported here to determine the effect of contact angle hysteresis on the Jamin effect and blob mobilization have not to our knowledge been published.

Further research on blob mobilization is needed, particularly in a multiply-connected porous medium that allows for a bypass or background flow. This situation would be typical during the flooding method commonly used for groundwater remediation, but the complex geometry of 3D porous media packing presents challenges. A pore doublet is a simplified model of a complex multiply-connected medium with bypass flow. It allows easy visualization of the blob, thus permitting investigation of the the effects of contact angle hysteresis on blob mobilization. Furthermore, once a blob is mobilized, it has not been clearly shown whether the contact angles everywhere on the contact lines will assume the values of the equilibrium advancing or receding contact angles.

1.3 Resonance of residual NAPL blobs

In the subsurface, porous media are usually saturated by two or more immiscible fluids. One of these fluids may exist as disconnected blobs which possibly occupy one or more pores [29]. For example, after being pumped or water-flooded, contaminated groundwater or oil reservoirs often contain residual NAPL blobs. Since trapped NAPL blobs cannot be mobilized by pumping alone [22], a promising method, originally developed by petroleum engineers, uses seismic/acoustic waves to enhance the effects of water flooding method. The method has been shown to improve NAPL removal in laboratory

experiments [6, 47, 45, 46, 44, 24].

Due to contact angle hysteresis, a blob in a capillary tube can sustain a pressure drop by changing the shape of its menisci. The menisci perform like springs, and the restoring force is the capillary force. Therefore, when a NAPL blob is subjected to oscillatory pressure drops or seismic waves, the blob might perform like a spring-mass system and exhibit resonance. Hilpert et al. [18] hypothesized that the mobilization of trapped blobs can be enhanced by exploiting resonance. Pioneering experiments on the resonance of a meniscus in a capillary tube, in which oscillatory flow had been established, were conducted by Dimon et al. [10] and Charlaix and Gayvallet [5]. Hilpert et al. [18] predicted that blobs in porous media exhibit capillarity-induced resonance. By performing lattice-Boltzmann simulations in three different pore geometries, Hilpert [16] showed that trapped blobs can be mobilized by excitation at their resonant frequency.

Holzner et al. [19] linked blob resonance to the detection of hydrocarbon reservoirs by a passive seismic technology, attributing high correlations between the presence of hydrocarbon reservoirs and low-frequency spectral anomalies computed from passively recorded seismic data to the resonance of hydrocarbon blobs. However, Broadhead [4] used various resonance amplification models to show that the frequency range of hydrocarbon microtremor is much lower than the resonant frequency of blobs. Therefore, there is a need for further investigation of the occurrence of blob resonance in the subsurface, and of the frequency response of liquid blobs to seismic excitation.

There are only a few studies that have experimentally demonstrated the occurrence

of blob resonance in porous media. Hilpert and Miller [17] and Bian et al. [3] both showed that water slugs in circular tubes can exhibit resonance. However, it has not been experimentally shown that blobs may also resonate in complex porous media, such as sphere packings.

1.4 Flow visualization and planar laser-induced fluorescence

Studying blob or meniscus movement in a porous medium requires an noninvasive flow visualization technique. This is not without experimental challenges. When the solid and liquid phases have different optical refractive indices, the resulting reflection of light in common 3D porous media (e.g. sphere packing) usually distorts any image of the blobs, preventing accurate quantitative analysis. This is true even for a transparent solid phase like glass. In order to avoid/reduce the light reflection, most experiments on studying the dynamics of menisci/blobs in porous media have been performed in the simple geometry of capillary tubes and mono-layer sphere packings [41, 10, 5, 6, 36, 2].

Ng et al. [35] examined blob mobilization in a sphere packing by matching the refractive index of the liquid that surrounded the blob with the one of the solid phase. They then illuminated their flow cell with background light. This measure significantly improved the image quality by reducing the reflection of light from the spheres. However, different menisci of a 3D blob projected on the 2D camera sensor may have overlapped in the

acquired images. If one manages to match all refractive indices of the solid and liquid phases, the entire visual domain will be unobstructed, but the liquid of interest will be indistinguishable. This problem can be solved by adding a laser-induced fluorescent dye into one of the liquids and then using a laser light sheet to excite the dye and illuminate the liquid. This is the basic concept of the laser-induced fluorescence (LIF) technique which was introduced in the late 70's [8, 39, 25, 11].

The two-dimensional planar LIF (PLIF) technique, a noninvasive method which is the most common application of LIF, has been widely used for studying different flow types [48, 55, 40, 7, 28, 1, 37, 54]. PLIF is also used to investigate multiphase flow in porous media [33, 43, 13, 51, 38, 21].

The LIF technique involves matching the optical refractive indices of the various phases that make up a multiphase system. For PLIF, a laser light beam is transformed into a thin sheet by a series of optical lenses. At a certain distance from the lens from which the sheet of laser light originates, the width of the sheet will be much larger than the original laser beam diameter. Once the laser light sheet is directed towards a liquid containing a laser-induced fluorescent dye, a two-dimensional cross-section of the flow will be illuminated. Normally, a camera is placed normal to the laser light sheet to capture images of the liquid flow. For multiphase flow in porous media, the recorded images can be used to determine the liquid-liquid interfaces and their movement. PLIF can also be extended to three dimensions by subsequently moving the laser light sheet perpendicular to the plane of the sheet and reconstructing the recorded images in parallel plans.

Compared with other noninvasive flow visualization methods for studying multiphase flow in porous media, e.g., MRI, NMR and X-ray tomography imaging, PLIF is relatively simple and inexpensive. In addition, it is capable of imaging the dynamics of fluid-fluid interfaces at high temporal resolution. However, the main disadvantage of this technique is the requirement of matching refractive indices in all phases. This restriction limits the range of materials that can be used as study targets. Fortunately, once the refractive-index-matched multiphase system is built, it can be used to perform particle image velocimetry (PIV), a technique which is widely used to measure the velocity field and other related properties in fluids. Furthermore, experiments have been designed to simultaneously perform PIV and PLIF for studying multiphase flow problems [40].

1.5 Dynamic capillary pressure and Green-Ampt model

It is equally important to investigate the effect of dynamic contact angle or dynamic capillary pressure at the pore scale as well as the Darcy scale. One of the major multiphase flow scenarios in the subsurface is the infiltration of a liquid into soil, e.g., rain water or a liquid contaminant seeping into dry soil.

The Green-Ampt (GA) model is a classical model to describe water infiltration into porous media. This one-dimensional model assumes a sharp moving interface between the water-saturated porous medium and the unsaturated porous medium. It also assumes a uniform satiated water content behind the interface and a uniform initial water content in front of the interface. One of the assumptions made in the GA approach is that the

hydraulic pressure head at the front is constant. Since the model assumes that the air pressure in the unsaturated soil ahead of the front is uniform and constant, it implies that the capillary pressure at the front is constant. This assumption, however, is not consistent with the idea that contact angle and capillary pressure are dynamic at the pore scale.

Several studies point out that the classical GA model cannot well describe the water front velocity during infiltration. Iwata et al. [23] suggest that deviations between the late stage of infiltration experiments performed by Tabuchi [53] and modeling based on the GA approach could be explained by a dynamic hydraulic pressure head at the wetting front that is due to a dynamic contact angle.

Weitz et al. [57] performed column experiments and proposed that the capillary pressure at a liquid-liquid interface depends on the average pore-scale fluid velocity according to a power law. Downward infiltration experiments done by Geiger and Durnford [15] have also shown that the capillary pressure at the infiltration front is Darcy velocity dependent. Siebold et al. [49] attributed the differences between capillary rise experiments in powder packings and the Washburn theory for infiltration into a capillary tube to a flow velocity dependent contact angle. DiCarlo [9] also observed that the capillary pressure at an infiltrating water front is not constant and is associated with the flow velocity. Weisbrod et al. [56] found that a GA model with a contact angle which is significantly larger than the equilibrium contact angle can well describe the early stage of upward infiltration. Therefore, there is a need to generalize the GA model to account for a dynamic capillary pressure at the wetting front that depends on the front velocity.

1.6 Outline of the dissertation

Chapter 2, "Pore-scale analysis of the effects of contact angle hysteresis on blob mobilization in a pore doublet", contains a published paper [21], and presents a series of experiments to visualize a blob in a model pore doublet under different external pressure differences. This pore model allows for a bypass or background flow of the wetting phase to generate the external pressure gradients that act on a trapped blob. The main objectives of the experiments are to measure the distribution of the contact angles and the curvatures of the menisci of a blob that is being mobilized, and to test the hypothesis that the Jamin effect on a blob in a straight tube is indeed due to contact angle hysteresis.

Chapter 3 of the dissertation, "Theoretical and experimental study of resonance of blobs in porous media" consists of a paper which is currently under review. I investigate the frequency response of blobs in a capillary tube and a sphere packing to oscillatory pressure differences. The PLIF technique is used to visualize the dynamics of blobs in the porous media. Along with the measured pressure data, I determine the frequency response of the blobs.

Chapter 4 of the dissertation, "Incorporation of dynamic capillary pressure into the Green-Ampt model for infiltration," contains a published paper which proposes a modified GA model to describe infiltration [20]. In this chapter, I formulate a general GA model accounting for a dynamic capillary pressure which depends on the flow velocity through a power law. With semi-analytical solutions, I reanalyze the infiltration experiments performed by Geiger and Durnford [15] and infer functional forms for dynamic capillary

pressure. Furthermore, I show that the new theory describes infiltration experiments by Tabuchi [53] better than the classical GA approach.

Chapter 5 summarizes the findings and conclusions of the three essays. The potential applications of combining these findings to enhance blob mobilization are also discussed. Furthermore, future work on blob mobilization and dynamic capillary pressure is mentioned in this chapter.

Bibliography

[1] P. E. Arratia and F. J. Muzzio. Planar laser-induced fluorescence method for analysis of mixing in laminar flows. *Industrial & Engineering Chemistry Research*, 43(20): 6557–6568, 2004.

[2] I. A. Beresnev, A. Gaul, and R. D. Vigil. Direct pore-level observation of permeability increase in two-phase flow by shaking. *Geophysical Research Letters*, 38:L20302, 2011. doi: 10.1029/2011GL048840.

[3] X. Bian, M. Perlin, W. W. Schultz, and M. Agarwal. Axisymmetric slosh frequencies of a liquid mass in a circular cylinder. *Physics of Fluids*, 15:3659–3664, 2003.

[4] M. K. Broadhead. Oscillating oil drops, resonant frequencies, and low-frequency passive seismology. *Geophysics*, 75(1):1–7, 2010.

[5] E. Charlaix and H. Gayvallet. Dynamics of a harmonically driven fluid interface in a capillary. *Journal de Physique II*, 2(11):2025–2038, 1992.

[6] C. V. Chrysikopoulos and E. T. Vogler. Acoustically enhanced ganglia dissolution and mobilization in a monolayer of glass beads. *Transport in Porous Media*, 64(1): 103–121, 2006.

[7] J. P. Crimaldi and J. R. Koseff. High-resolution measurements of the spatial and temporal scalar structure of a turbulent plume. *Experiments in Fluids*, 31(1):90–102, 2001.

[8] C. Dewey. Qualitative and quantitative flow field visualization utilizing laser-induced fluorescence. *In: Proceedings of the AGARD conference of non-intrusive instrumentation in fluid flow research, AGARD-CP-193*, 1976.

[9] DiCarlo. Capillary pressure overshoot as a function of imbibition flux and initial water content. *Water Resources Research*, 43:W08402, 2007. doi: 10.1029/2006WR005550.

[10] P. Dimon, A. P. Kushnick, and J. P. Stokes. Resonance of a liquid-liquid interface. *Journal de Physique*, 49(5):777–785, 1988.

[11] P. E. Dimotakis, R. C. Miakelye, and D. A. Papantoniou. Structure and dynamics of round turbulent jets. *Physics of Fluids*, 26(11):3185–3192, 1983.

[12] M. Dong, Q. Fan, and L. Dai. An experimental study of mobilization and creeping flow of oil slugs in a water-filled capillary. *Transport in Porous Media*, 80:455–467, 2009. doi: 10.1007/s1122-009-9374-5.

[13] M. M. Fontenot and R. D. Vigil. Pore-scale study of nonaqueous phase liquid dissolution in porous media using laser-induced fluorescence. *Journal of Colloid and Interface Science*, 247:481–489, 2002.

[14] D. R. Gardescu. Behavior of gas bubbles in capillary spaces. *Trans. AIME*, 86:351, 1930.

[15] S.L. Geiger and D.S. Durnford. Infiltration in homogeneous sands and a mechanistic model of unstable flow. *Soil Science Society of America Journal*, 64(2):460–469, 2000.

[16] M. Hilpert. Capillarity-induced resonance of blobs in capillary porous media: analytical solutions, lattice-Boltzmann modeling, and blob mobilization. *Journal of Colloid and Interface Science*, 309:493–504, 2007.

[17] M. Hilpert and C. T. Miller. Experimental investigation on the resonance of a liquid column in a capillary tube. *Journal of Colloid and Interface Science*, 219(1):62–68, 1999.

[18] M. Hilpert, G. H. Jirka, and E. J. Plate. Capillarity-induced resonance of oil blobs in capillary tubes and porous media. *Geophysics*, 65:874–883, 2000.

[19] R. Holzner, P. Eschle, S. Dangel, M. Frehner, C. Narayanan, and D. Lakehal. Hydrocarbon microtremors interpreted as nonlinear oscillations driven by oceanic background waves. *Communications in Nonlinear Science and Numerical Simulation*, 14: 160–173, 2009.

[20] S. Y. Hsu and M. Hilpert. Incorporation of dynamic capillary pressure into the green-ampt model for infiltration. *Vadose Zone Journal*, 10:642–653, 2011.

[21] S. Y. Hsu, R. Glantz, and M. Hilpert. Pore-scale analysis of the effects of contact angle hysteresis on blob mobilization in a pore doublet. *International Journal of Oil, Gas and Coal Technology*, in-press, 2012.

[22] J. R. Hunt, N. Sitar, and K. S. Udell. Nonaqueous phase liquid transport and cleanup 1. Analysis of mechanisms. *Water Resources Research*, 24(8):1247–1258, 1988.

[23] S. Iwata, T. Tabuchi, and B.P. Warkentin. *Soil-water interactions: mechanisms and applications*. Marcel Dekker, New York, 2nd edition, 1995.

[24] W. Li, D. V. Vigil, I. A. Beresnev, P. Iassonov, and R. Ewing. Vibration-induced mobilization of trapped oil ganglia in porous media: experimental validation of a capillary-physics mechanism. *Journal of Colloid and Interface Science*, 289:193–199, 2005.

[25] H. T. Liu, J. T. Lin, D. P. Delisi, and F. A. Robben. Application of a fluorescence technique to dye-concentration measurements in a turbulent jet. *In: Proceedings of the symposium on flow measurement in open channels and closed conduits. NBS Special Publication*, 484:423–446, 1977.

[26] B. L. Longino and B. H. Kueper. Effects of capillary pressure and use of polymer solutions on dense non-aqueous-phase liquid retention and mobilization in a rough-walled fracture. *Environmental Science & Technology*, 33(14):2447–2455, 1999.

[27] D. M. Mackay and J. A. Cherry. Groundwater contamination: Pump-and-treat remediation. *Environmental Science & Technology*, 23(6):630–636, 1989.

[28] R. Matsumoto, H. F. Zadeh, and P. Ehrhard. Quantitative measurement of depth-averaged concentration fields in microchannels by means of a fluorescence intensity method. *Experiments in Fluids*, 39(4):722–729, 2005.

[29] A. S. Mayer and C. T. Miller. The influence of porous medium characteristics and measurement scale on pore-scale distributions of residual nonaqueous-phase liquids. *Journal of Contaminant Hydrology*, 11(3/4):189–213, 1992.

[30] J. C. Melrose and C. F. Brandner. Role of capillary force in determining microscopic displacement efficiency for oil recovery by waterflooding. *Can. J. Petrol. Technol.*, 13(4):54–62, 1974.

[31] J. W. Mercer and R. M. Cohen. A review of immiscible fluids in the subsurface: properties, models, characterization and remediation. *Journal of Contaminant Hydrology*, 6(2):107–163, 1990.

[32] C. T. Miller, M. M. Poirier-McNeill, and A. S. Mayer. Dissolution of trapped nonaqueous phase liquids: Mass transfer characteristics. *Water Resources Research*, 26 (11):2783–2796, 1990.

[33] C. D. Montemagno and W. G. Gray. Photoluminescent volumetric imaging –A tech-

nique for the exploration of multiphase flow and transport in porous media. *Geophysical Research Letters*, 22(4):425–428, 1995.

[34] N. R. Morrow. The effects of surface roughness on contact angle with special reference to petroleum recovery. *The Journal of Canadian Petroleum Technology*, 14(4): 42–53, 1975.

[35] K. M. Ng, H. T. Davis, and L. E. Scriven. Visualization of blob mechanics in flow through porous media. *Chemical Engineering Science*, 33(8):1009–1017, 1978.

[36] P. K. Niven and K. Singh. Mobilization and rupture of LNAPL ganglia during freeze-thaw: two-dimensional cell experiments. *Environmental Science & Technology*, 42: 5467–5471, 2008.

[37] R. Onishi and S. Komori. Thermally stratified liquid turbulence with a chemical reaction. *AIChE Journal*, 52(2):456–468, 2006.

[38] H. Ovdat and B. Berkowitz. Pore-scale study of drainage displacement under combined capillary and gravity effects in index-matched porous media. *Water Resources Research*, 42:W06411, 2006. doi: 10.1029/2005WR004553.

[39] F. Owen. Simultaneous laser measurement of instantaneous velocity and concentrations in turbulent mixing flows. *In: Proceedings of the AGARD conference of non-intrusive instrumentation in fluid flow research, AGARD-CP-193*, 1976.

[40] G. Pan and H. Meng. Experimental study of turbulent mixing in a tee mixer using PIV and PLIF. *AIChE Journal*, 47(12):2653–2665, 2001.

[41] A. C. Payatakes. Dynamics of oil ganglia during immiscible displacement in water-wet porous media. *Annual Review Fluid Mechanics*, 14:365–393, 1982. doi: 10.1146/annurev.fl.14.010182.002053.

[42] K. D. Pennell, G. A. Pope, and L. M. Abriola. Influence of viscous and buoyancy force on the mobilization of residual tetrachloroethylene during surfactant flushing. *Environmental Science & Technology*, 30(4):1328–1335, 1996.

[43] M. Rashidi, L. Peurrung, A. F. B. Tompson, and T. J. Kulp. Experimental analysis of pore-scale flow and transport in porous media. *Advances in Water Resources*, 19 (3):163–180, 1996.

[44] L. N. Reddi. Feasibility of in situ implementation of vibrations to mobilize NAPL ganglia. *Journal of Soil Contamination*, 3(1):29–46, 1994.

[45] L. N. Reddi and S. Challa. Vibratory mobilization of immiscible liquid ganglia in sands. *Journal of Environmental Engineering ASCE*, 120(5):1170–1190, 1994.

[46] L. N. Reddi and H. Wu. Mechanisms involved in vibratory destabilization of NAPL ganglia in sands. *Journal of Environmental Engineering*, 122(12):1115–1119, 1996.

[47] P. M. Roberts, A. Sharma, V. Uddameri, M. Monagle, D. E. Dale, and L. K. Steck.

Enhanced DNAPL transport in a sand core during dynamic stress stimulation. *Environmental Science & Technology*, 18(2):67–69, 2001.

[48] K. Shiono and T. Feng. Turbulence measurements of dye concentration and effects of secondary flow on distribution in open channel flows. *Journal of Hydraulic Engineering ASCE*, 129(5):373–384, 2003. doi: 10.1061/(ASCE)0733-9429(2003)129:5(373).

[49] A. Siebold, M. Nardin, J. Schultz, A. Walliser, and M. Oppliger. Effect of dynamic contact angle on capillary rise phenomena. *Colloids and Surfaces A: Physicochemical and Engineering Aspects*, 161(1):81–87, 2000.

[50] W. O. Smith and M. D. Crane. The Jamin effect in cylindrical tubes. *J. Am. Chem. Soc.*, 52(4):1345–1349, 1930.

[51] M. Stöhr, K. Roth, and B. Jähne. Measurement of 3D pore-scale flow in index-matched porous media. *Experiments in Fluids*, 35:159–166, 2003.

[52] J. J. Taber. Dynamic and static forces required to remove a discontinuous oil phase from porous media containing both oil and water. *Soc. Pet. Eng. J.*, 9(3):3–12, 1969.

[53] T. Tabuchi. Infiltration and capillarity in the particle packing [in Japanese]. *Rec. Land Reclam. Res.*, 19:1–121, 1971.

[54] C. D. Troy and J. R. Koseff. The instability and breaking of long internal waves. *Journal of Fluid Mechanics*, 543:107–136, 2005.

[55] D. R. Webster, S. Rahman, and L. P. Dasi. Laser-induced fluorescence measurements of a turbulent plume. *Journal of Engineering Mechanics ASCE*, 129(10):1130–1137, 2003.

[56] N. Weisbrod, T. McGinnis, M.L. Rockhold, and M.R. Niemet. Effective darcy-scale contact angles in porous media imbibing solutions of various surface tensions. *Water Resources Research*, 45(W00D39), 2009. doi: 10.1029/2008WR006957.

[57] D. A. Weitz, J.P. Stokes, R.C. Ball, and A.P. Kushick. Dynamic capillary pressure in porous media: Origin of the viscous-fingering length scale. *Physical Review Letters*, 59(26):2967–2970, 1987.

Chapter 2. Pore-scale Analysis of the Effects of Contact Angle Hysteresis on Blob Mobilization in a Pore Doublet

Abstract

The mobilization of residual oil blobs in porous media is hampered by the so-called Jamin effect. We studied the Jamin effect experimentally in a pore doublet model and explain it through contact angle hysteresis. We measured the contact angles (in 2D and 3D) and the mean curvatures of a blob trapped in the pore doublet model. Due to gravity effects and hysteresis, the contact angles were initially (subject to zero pressure gradient) nonuniform and exhibited a pronounced altitude dependence. As the pressure gradient was increased, both the altitude dependence and nonuniformity of contact angles decreased, and the mean curvature of the drainage and imbibition interfaces increased and decreased, respectively. The predicted pressure drops inferred from our theory were in line with the directly measured ones. We also developed methods to measure contact angles and mean curvatures in 3D.

2.1 Introduction

When an oil reservoir is water flooded, the displaced oil leaves behind significant numbers of residual blobs trapped in pores [15]. The petroleum industry has a major economic interest in mobilizing these blobs. Taber [30] pointed out that the trapping is due to the "Jamin effect," i.e., nonwetting blobs can sustain pressure gradients in the surrounding wetting phase, even in a cylindrical capillary tube. Smith and Crane [29] derived a theory for a tube exposed to the atmosphere on one end and acted upon by a pressure p on the other end. The maximum or critical pressure p' which n bubbles in a capillary tube can sustain is a function of interfacial tension and the tube radius, as well as advancing and receding contact angles. However, no experiments have been performed to investigate the link between the Jamin effect and contact angle hysteresis.

Melrose and Brandner [15] theoretically predicted the critical pressure gradient needed to remobilize a blob trapped in a packing of uniform spheres:

$$\left(\frac{\Delta p}{\Delta L}\right)_{crit} = \frac{\sigma\left[J'_{dr} - J'_{im}\right]}{2Nr_{sp}} \tag{2.1}$$

where r_{sp} is the radius of the spherical particles, ΔL is the length of the blob in the flow direction, N is this length measured in units of the particle diameter $2r_{sp}$, and J'_{dr} and J'_{im} are the critical total curvatures of the blob's downstream and upstream fluid-fluid interfaces that undergo drainage and imbibition, respectively. (Note that the total curvature J is twice the value of the mean curvature H.) These curvatures are related

to contact angle through $J'_{dr} = 2\hat{J}_{dr} Z_{dr} \cos(\theta)/R$ and $J'_{im} = 2\hat{J}_{im} Z_{im} \cos(\theta)/R$ where Z_{dr} and Z_{im} are correction functions that account for differences between the underlying model pore system and the sphere packing, $\hat{J}_{dr}$ and $\hat{J}_{im}$ are the normalized values of the two limiting curvatures for the case of zero contact angle, and R is a characteristic distance for the pore model. For the case of zero contact angle, $\theta = 0$, Melrose and Brandner [15] related the critical pressure gradient given by Eq. (2.1) to the corresponding critical capillary number

$$\mathrm{Ca}_{crit} = \left(\frac{\eta v}{\sigma}\right)_{crit} = \frac{k_{rw}\kappa}{N\phi R^2}\left(\hat{J}_{dr} - \hat{J}_{im}\right) \tag{2.2}$$

where η is dynamic viscosity of the liquid, v is Darcy velocity, k_{rw} is the relative permeability of water, κ is the intrinsic permeability, and ϕ is the porosity. Similarly, Ng et al. [22] derived an expression for the critical capillary number that is based on the average pore-throat radius r_t and the average pore-body radius r_b:

$$\mathrm{Ca}_{crit} = \frac{2\kappa_e}{\Delta L}\left(\frac{1}{r_t} - \frac{1}{r_b}\right) \tag{2.3}$$

where κ_e is the effective permeability of the porous medium. Ng and Payatakes [21] accounted for contact angle hysteresis when calculating a so-called appendix mobilization number. When determining the critical blob mobilization condition, however, they used the further simplification that $\theta_R^{(eq)} = \theta_A^{(eq)} = \theta_e$ where θ_e is the intrinsic contact angle, and $\theta_R^{(eq)}$ and $\theta_A^{(eq)}$ are the equilibrium receding and advancing contact angles.

Over decades, Eq. (2.2) and Eq. (2.3) have been used to study immiscible flow in the

subsurface [16] and blob mobilization during enhanced oil recovery based on surfactant flushing [23], polymer flooding [14], and vibratory or acoustical enhancement [24, 6]. Although the contact angle in oil reservoirs is quite variable and affects oil recovery [20], most of these studies have neglected contact angle hysteresis or even assumed a contact angle of zero.

Blob mobilization has also been investigated experimentally. Both Smith and Crane [29] and Gardescu [9] experimentally verified the Jamin effect in a capillary tube with circular cross-section where water was a partially wetting fluid. They suggested that the Jamin effect is due to contact angle hysteresis. Rose and Heins [26] showed that the difference in the receding and advancing contact angles caused a pressure drop in addition to the viscous pressure drop. Dong et al. [8] studied the variation of the pressure drop during the mobilization of a nonwetting oil blob in a single glass tube. They then imposed a very small constant flow and observed the mobilization process. They have shown that the "Jamin effect is an external expression of the resistance of the tube wall to the viscous pressure drop of slug flow." They mentioned that the constant pressure drop during the hold-up stage, which precedes blob movement, is due to contact angle hysteresis. However, they neither measured contact angles nor compared the constant pressure drop to the calculated pressure drop from Eq. (2.1). Thus contact angle hysteresis has not been proven to be the only cause of the Jamin effect.

After the 1960s, most blob mobilization studies investigated the effects of interfacial tension, pressure gradient, liquid density, and pore geometry. Although Morrow [18]

had mentioned that contact angle hysteresis tends to increase the capillary forces which control oil recovery, none of the above-mentioned experimental studies directly measured the contact angles and determined the effect of contact angle hysteresis on the Jamin effect and blob mobilization.

To summarize, there is a need for blob mobilization experiments in a multiply connected porous medium that allows for a bypass or background flow of the wetting phase and that allows one to study the effects of contact angle hysteresis on blob mobilization. It is also not yet clear whether the contact angles on the contact lines of the drainage and imbibition interfaces will assume, everywhere on the contact lines, the values of the equilibrium advancing and receding contact angles $\theta_A^{(eq)}$ and $\theta_R^{(eq)}$, respectively, once a blob is mobilized due to a gradually increasing pressure gradient. This point is important because the contact angle of an interface of a stationary blob could be nonuniform even when the blob is mobilized. Thus one could argue that a blob can still be mobilized once $\theta_A^{(eq)}$ and $\theta_R^{(eq)}$ are assumed on only part of all points of the drainage and imbibition interfaces, respectively, which in turn would critically affect the mobilization condition.

The main objectives of this chapter are to measure the distribution of the contact angles and the curvatures of the liquid-liquid interfaces of a blob that is being mobilized and to test the hypothesis that the Jamin effect on a blob in a straight tube is indeed due to contact angle hysteresis. Due to experimental limitations, a relatively large tube diameter had to be chosen, such that gravity affected the shape of the fluid-fluid interfaces, even though gravity did not significantly affect blob mobilization, because the pore doublet

model was oriented horizontally. Given the difficulty of modeling curved interfaces in three dimensions (3D), we pursue a 1D modeling approach. We assume that an interface of a blob can be described by a spherical cap that possesses a single effective contact angle. We divide the tube into three sections: the wetting liquid in front of the receding interface, the blob itself, and the wetting liquid behind the advancing interface. We use Poiseuille's law to model flow in each of the three tube sections. In Section 2.2, we extend [5] theory for immiscible flow in a pore doublet model to calculate the relationship between the flow rate and the pressure drops across the pore doublet model with and without a trapped blob in one of the tubes. Section 2.3 is devoted to the introduction of the pore doublet model, a non-invasive Planar Laser-Induced Fluorescence (PLIF) visualization technique for measuring contact angles and curvatures, and the experimental procedure. In Section 2.4, we present experimental results about the dynamics of the 2D and 3D contact angles and mean curvatures of a blob's interfaces if the blob is subjected to different pressure gradients. In Section 2.5, we confirm that the Jamin effect in a straight tube is indeed due to contact angle hysteresis.

2.2 Theory

Chatzis and Dullien [5] used pore doublet models in a series of pioneering theoretical analyses and experiments of immiscible displacement in porous media. In contrast to Chatzis and Dullien, who investigated blob trapping, we focus on the mobilization of the trapped blob due to a bypass flow of the continuous liquid. Thus our study mimics the

mobilization of blobs trapped in porous media by the water flooding method.

All contact angles used in this chapter, except for the intrinsic contact angle θ_e, are apparent contact angles which can be observed with standard optical equipment. The contact angles on the contact line of an interface depend on the flow process that formed the interface. Even though gravity does not affect θ_e according to Young's equation, Sasges and Ward [28] and Gu and Yang [10] have shown that gravity affects both the apparent equilibrium contact angle and the curvatures of the interfaces in a capillary tube. Therefore contact angles along the same contact line can be nonuniform due to gravity. Since contact angle and curvature are actually nonuniform, we must therefore infer effective/average contact angles and curvatures that we can then use in the modeling.

Our pore doublet model consists of two capillary tubes (Tube 1 and Tube 2) connected to a syringe pump and a liquid reservoir, both of which contain the continuous liquid that creates the bypass flow (see **Figure 2.1)**. The imposed steady-state flow rates are sufficiently small so that the Reynolds number Re $\ll 1$. Therefore single-phase flow in a tube is described by the Poiseuille equation. The flow rate in any section of a tube is

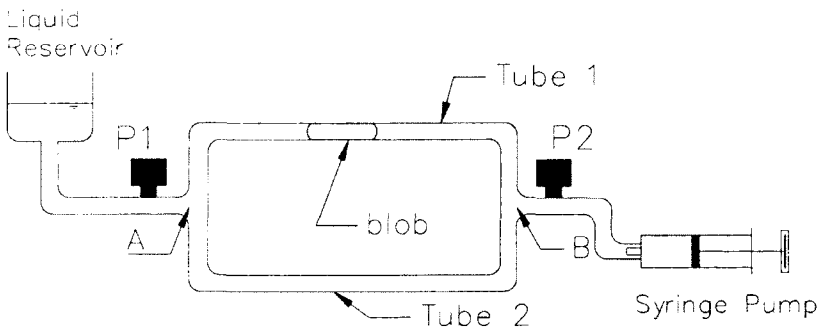

Figure 2.1: Sketch of our experimental pore doublet model. P1 and P2 are pressure transducers.

given by $Q = -kr^4 dp/dz$ where r is the radius of the tube, $k = \pi/(8\eta)$, and dp/dz is the pressure gradient [2]. The system of equations of flow rates and pressure gradients is

$$\begin{aligned} Q_t &= \sum_{j=1}^{2} Q_j \\ Q_j &= -kr_j^4 \frac{\Delta p}{L_j}, \qquad j = 1, 2 \end{aligned} \tag{2.4}$$

where Q_t is the total flow rate in the system, i.e. the pumping rate, Q_j is the flow rate in Tube j, Δp is the pressure drop across the pore doublet model (between points A and B in **Figure 2.1)**, and L_j is the length of tube j also between A and B. If Q_t is known, we can calculate Δp for single-phase flow:

$$\Delta p = -\frac{Q_t}{k} \left(\sum_{j=1}^{2} \frac{r_j^4}{L_j} \right)^{-1} \tag{2.5}$$

Figure 2.2 illustrates the interfaces of a trapped blob in a horizontal tube and our coordinate system. By cutting the blob with x-y planes $z = z_i$ we obtain profiles as the ones shown in **Figure 2.3a**. Gravity and surface heterogeneity lead to non-spherical interfaces and nonuniform contact angles. **Figure 2.3a** illustrates how a trapped blob responds to a gradually increasing pressure drop Δp. For zero forcing, $\Delta p = 0$, the blob is assumed to be symmetric, i.e. the bottom as well as the top contact angles are equal. When $|\Delta p|$ increases, the contact points remain pinned, but the liquid-liquid interfaces change their shapes. The contact angles on the interfaces also change from initial values

θ_0^b and θ_0^t to θ_{im}^b and θ_{im}^t on the imbibition interfaces, and to θ_{dr}^b and θ_{dr}^t on the drainage interfaces. **Figure 2.3b** shows the average (arithmetic mean) of the top and bottom contact angles of the drainage and imbibition interfaces, i.e., the values $(\theta_{dr}^b + \theta_{dr}^t)/2$ and $(\theta_{im}^b + \theta_{im}^t)/2$, as a function of Δp.

For a trapped blob, $Q_1 = 0$, $Q_t = Q_2$, and the pressure drop amounts to

$$\Delta p = -\frac{Q_t}{k}\left(\frac{r_2^4}{L_2}\right)^{-1} = -\sigma\left[J_{dr} - J_{im}\right] \tag{2.6}$$

where J_{dr} and J_{im} are the total curvatures of the drainage and the imbibition interfaces, respectively. Note that J_{dr} and J_{im} are usually not equal to J'_{dr} and J'_{im} in Eq. (2.1), because a trapped blob does not have to be in the critical condition for mobilization. The

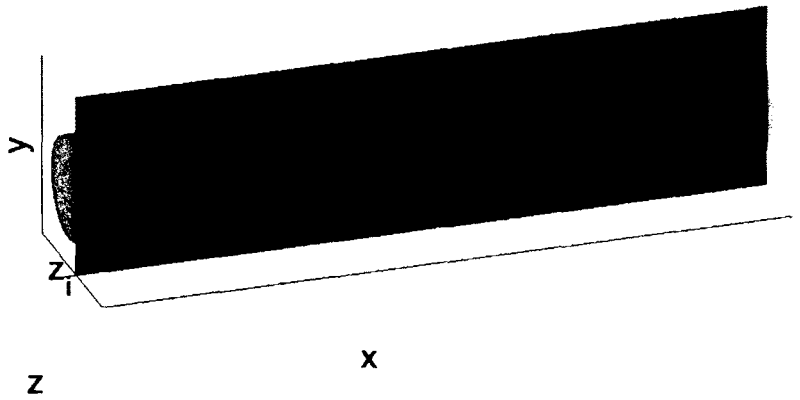

Figure 2.2: Schematic representation of a blob in a cylindrical tube. The x-axis of our orthogonal coordinate system is parallel to the axis of the horizontal tube, and the y-axis is vertical. The blob is shown in blue. The intersection, which is shown in the dark blue cross-section, of the blob and the light green plane $z = z_i$ yields profiles as the ones shown in Figure 2.3a.

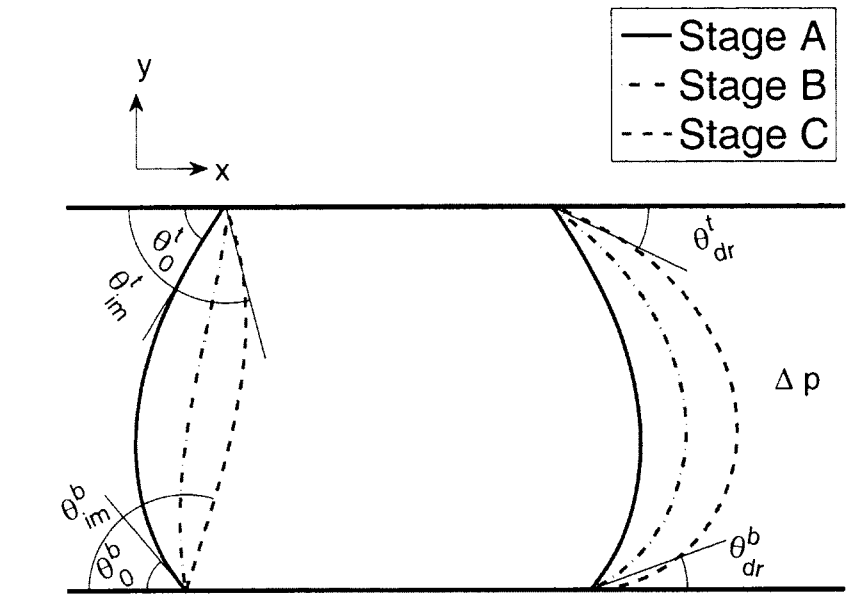

(a)

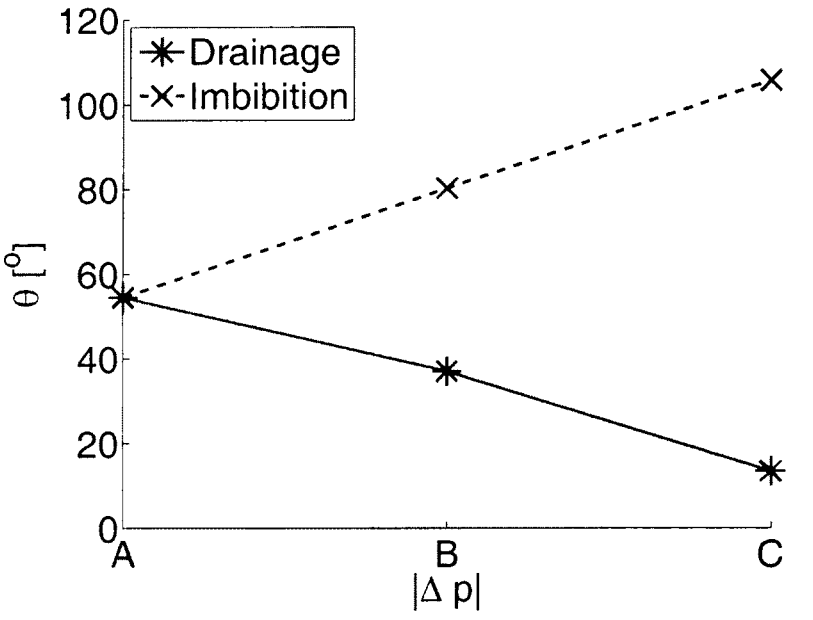

(b)

Figure 2.3: (a) Cross-section of a blob subject to a pressure drop Δp accomplished by a change in wetting phase pressure on the right side of the blob. The two solid horizontal line segments represent the boundary of the tube. The solid curves (Stage A) show the profiles of the gravity-distorted interfaces for $\Delta p = 0$. The non-solid curves (Stages B and C) show the profiles of the gravity-distorted interfaces for $|\Delta p| > 0$. (b) Average contact angle of the drainage and imbibition interfaces as a function of Δp.

Δp given by Eq. (2.6) represents not only the driving force of Q_t in Tube 2 but also the sustained pressure due to the Jamin effect on the blob.

Before reaching the critical condition for mobilization, the contact angles on both interfaces can be between the equilibrium advancing and receding contact angles, $\theta_A^{(eq)}$ and $\theta_R^{(eq)}$. If the interfaces are spherical and contact angles are uniform on the contact lines, $J_{dr} = 2\cos(\theta_{dr})/r_1$ and $J'_{im} = 2\cos(\theta_{im})/r_1$ where θ_{dr} and θ_{im} are contact angles on the drainage and imbibition interfaces. If not, θ_{dr} and θ_{im} can be determined by using average or effective contact angles.

In order to move a blob, the pressure drop across the blob needs to overcome the difference between the capillary pressures at the drainage and imbibition interfaces when the contact angles reach the receding and advancing contact angles, respectively. The critical pressure drop is

$$\Delta p_{crit} = -\sigma \left[J'_{dr} - J'_{im}\right] \tag{2.7}$$

while the critical flow rate is given by

$$Q_{crit} = \sigma \left[J'_{dr} - J'_{im}\right] \frac{k r_2^4}{L_2} \tag{2.8}$$

where J'_{dr} and J'_{im} are critical curvatures and $J'_{dr} > J'_{im}$. If contact angles were uniform on each of the two contact lines, $J'_{dr} = 2\cos(\theta_R^{(eq)})/r$ and $J'_{im} = 2\cos(\theta_A^{(eq)})/r$.

Once $|\Delta p| > |\Delta p_{crit}|$, the blob moves, that is, $Q_1 > 0$, and the pressure drop across

the model becomes

$$\begin{aligned}\Delta p &= -\frac{Q_t - Q_1}{k_c}\left(\frac{r_2^4}{L_2}\right)^{-1} \\ &= -\sigma\left[J_{dr} - J_{im}\right] - \frac{Q_1}{k_b}\left(\frac{r_1^4}{L_{1b}}\right)^{-1} - \frac{Q_1}{k_c}\left(\frac{r_1^4}{L_{1c}}\right)^{-1} \end{aligned} \tag{2.9}$$

where L_{1c} is the total length of the continuous liquid in Tube 1, $k_c = \pi/(8\eta_c)$, η_c is the viscosity of the continuous liquid, L_{1b} is the length of the blob in Tube 1, $k_b = \pi/(8\eta_b)$, and η_b is the viscosity of the liquid that forms the blob. If contact angles were uniform on each of the two contact lines, $J_{dr} = 2\cos(\theta_R^{(dyn)})/r_1$ and $J_{im} = 2\cos(\theta_A^{(dyn)})/r_1$ where $\theta_R^{(dyn)}$ and $\theta_A^{(dyn)}$ are the dynamic contact angles of the drainage and imbibition interfaces which depend on the capillary number Ca $= \eta v/\sigma$ [26, 25, 11].

The critical pressure drop and flow rate can be inversely determined from the measured contact angles or the measured interface curvatures by using Eqs. (2.7) and (2.8). Also once the blob moves, we can invert Eq. (2.9) to estimate Q_1 and the velocity of the blob for a given Q_t or pressure drop Δp.

2.3 Methods

2.3.1 Pore doublet model

Our pore doublet model consists of two different tubes (see **Figure 2.1**). While Tube 2 is a simple PTFE axially symmetric tube with an inside diameter of 1.9 mm, Tube 1 is

more complex in order to allow for an unobstructed visual observation of a blob therein. Tube 1 consists of three sections. Like Tube 2, both the first and third section consist of PTFE tubing. The second section, however, is made from an acrylic rectangular prism through which a hole with a diameter of 2 mm was drilled parallel to the long axis of the prism. The length of each tube (from A to B) is 242 mm. Tubes 1 and 2 are connected at one end by a T-connector at point A and then to a syringe pump. The other ends are also connected by a T-connector at point B and then to a liquid reservoir. Pressure transducers (PX 170, Omega) are installed on both sides of the pore doublet.

2.3.2 Blob visualization

We applied the PLIF technique, a non-invasive method of flow observation [17], to visualize the blob dynamics. PLIF experiments require that the refractive indices of the two liquid phases and the solid phase (acrylic flow cell) match. The choices of two immiscible liquids, both of which have the refractive index of 1.49 and at least one of which must be compatible with laser dyes, is limited. We chose oil-based *Code 5095* and water-based *OHZB* from Cargille Lab whose densities are, however, very different. The two liquids cannot visually be distinguished from one another. To do so, we added the fluorescent dye *Sulforhodamine G*, which can be excited by lasers with wavelengths around 532 nm, into the liquid *OHZB*, and injected it into the liquid *code 5095*-filled tube to form a blob. The blob became visible by illumination with a laser light sheet which was generated by a 1.5 W DPSS laser (532 nm wavelength) beam passing through a series of lenses. The

properties of the two liquids are shown in **Table 2.1**. The interfacial tension between the two liquids (one with the fluorescent dye) was measured by the sessile drop method [4].

Table 2.1: Properties of liquid phases at 25°C.

	Wetting phase liquid *code 5095*	Nonwetting phase liquid *OHZB*
Density ρ (g/cm^3)	0.869	2.055
Kinematic Viscosity ν (cSt)	15	5
Interfacial tension σ (dyne/cm)	6.72	

A PC-controlled high-speed CMOS digital camera (Basler 504Kc), 500 frames/sec at full spatial resolution of 1280x1024 pixels, was used to record the dynamics of the fluorescent blob. The images of a blob's cross-sections were analyzed to detect phase boundaries with edge detection software tools.

In 3D PLIF, the higher the number of cross-sectional images at different positions in the z-direction, the better the quality of the reconstructed 3D blob image is. However, the thickness of the laser light sheet which cannot be arbitrarily lowered limits the number of the cross-sectional images. Therefore, the thickness of the light sheet, but not the resolution of the digital camera, determines the maximum achievable quality of the 3D images. We managed to create sheets that were 50 μm thick. In order to obtain high quality 3D blob images, we chose a tube diameter in which a blob in the tube was discretized by 40 cross-sectional images at different positions in the z-direction. Therefore, Tube 1 had to have a relatively large diameter of 2 mm that allowed gravity to affect the blob shape.

We reconstructed 3D blob images from a series of images of equally spaced and

parallel cross-sections. The intersection between the vertical plane and the blob in **Figure 2.2** shows an example of a cross-section. The intersections of the laser sheets with the blobs were up to 6 mm wide and 50 μm thick. After an image was recorded, a precision translation stage moved the camera, the optical lenses, and the light sheet in the direction normal to the light sheet. Thus, the diameter of the blob, i.e. 2 mm, was covered in 40 steps of 50 μm. The whole scanning process was completed in 1 min. The resulting 3D image was then segmented into the two liquid phases and the solid phase. Thus, we were able to identify the solid-liquid interface and the two liquid-liquid interfaces.

2.3.3 Contact angle and curvature measurement

Liquid-liquid interfaces of a sessile drop or an axially symmetric blob in a capillary tube can be delineated, and 2D contact angles can be determined from the meridian profile of the interfaces [26, 28, 10, 3]. Specifically, we fitted polynomial curves to the blob's meridian profiles and determined the angles θ between the tangents of the fitted curves and the cylindrical walls at the contact points. In the Cartesian x-y plane this amounts to

$$\theta = \text{arccot}\left(\frac{dx(y')}{dy}\right) \tag{2.10}$$

where the x-axis coincides with the lower wall of the tube, the y-axis is normal to the wall, and y' is the location of contact point [3]. Two contact angles were determined from a single interface: the top one is at a contact point on the upper wall of the tube, and the bottom one is on the lower wall.

We further developed a method to measure 3D contact angles on an entire contact line of a 3D blob not restricting ourselves to the meridian profile. The contact angles in the continuous/wetting liquid can be estimated through the angles between two normals along the contact lines: a normal of the liquid-liquid interface pointing into the nonwetting phase and a normal of the solid-liquid interface pointing into the liquid.

The method is based on analyzing the series of 2D images from which 3D images of the blob are reconstructed. The imaged 2D cross-sections are defined in the x-y plane and were acquired for different z-positions. The liquid-liquid interfaces of the cross-sections, which are curves, were fitted by polynomial curves $X^{xy}(y,z)$. The superscript xy means that the fitted 2D polynomial functions were on the x-y plane. After processing all 2D images, we had a set of polynomial curves $X_i^{xy}(y,z_i)$ in x-y planes for different z values z_i where $i=1,\ldots,N$, and N is the number of 2D images. The x,z coordinates of the curves on the 3D interface in the x-z planes with different values of y_i were interpolated from $X_i^{xy}(y,z_i)$ and fitted by polynomial curves $X_i^{xz}(y_i,z)$ in the x-z plane with different y_i, which now form x-z curves on the liquid-liquid interfaces. At a point $\vec{r'}=(x',y',z')$, where the curves X_i^{xy} and X_i^{xz} intersect on a three-phase contact line, we have the two tangential vectors

$$\begin{aligned}\vec{v}_i^{xy}(x',y',z') &= \begin{pmatrix}\dfrac{dX_i^{xy}(y',z')}{dy} & 1 & 0\end{pmatrix}\\ \vec{v}_i^{xz}(x',y',z') &= \begin{pmatrix}\dfrac{dX_i^{xz}(y',z')}{dz} & 0 & 1\end{pmatrix}\end{aligned} \tag{2.11}$$

while the normal vector of the tangential plane of the liquid-liquid interface is

$$\vec{n}_{int}(x', y', z') = \vec{v}_i^{xy}(x', y', z') \times \vec{v}_i^{xz}(x', y', z') \tag{2.12}$$

The 3D contact angle $\theta_{3D}(x', y', z')$ at the point $\vec{r'}$ is defined to be the angle between the normal vector of the capillary tube surface $\vec{n}_t$ and $\vec{n}_{int}$:

$$\theta_{3D}(x', y', z') = \cos^{-1}\left(\frac{\vec{n}_{int} \cdot \vec{n}_t}{|\vec{n}_{int}|\,|\vec{n}_t|}\right) \tag{2.13}$$

Without measuring contact angles, one can determine the capillary pressure by using the general Young-Laplace equation which holds true for an arbitrarily curved fluid-fluid interface:

$$p_c = 2\sigma H \tag{2.14}$$

where H is the mean curvature. The curvature at a point $\vec{r'}$ equals

$$H = \frac{1}{2}(k_1 + k_2) = \frac{EN + GL - 2FM}{2(EG - F^2)} \tag{2.15}$$

where k_1 and k_2 are two principal curvatures, and E, F, G, L, M, and N are the coefficients of the first and second fundamental form evaluated at $\vec{r'}$ [13]. From a parameterization of the interface, $\vec{x} = \vec{x}(u, v)$, one can determine the coefficients of the first fundamental form via $E = \vec{x}_u \cdot \vec{x}_u$, $F = \vec{x}_u \cdot \vec{x}_v$, and $G = \vec{x}_v \cdot \vec{x}_v$. Using the unit

normal $\vec{n} = \frac{\vec{x}_u \times \vec{x}_v}{|\vec{x}_u \times \vec{x}_v|}$, the coefficients of the second fundamental form are $L = \vec{x}_{uu} \cdot \vec{n}$, $M = \vec{x}_{uv} \cdot \vec{n}$, and $N = \vec{x}_{vv} \cdot \vec{n}$. In order to estimate the derivatives of the parameterization, e.g., $\vec{x}_u$ or $\vec{x}_{uu}$, via difference quotients, we first approximated the fluid-fluid interface by a mesh $\bar{X}$, $\bar{Y}$ and $\bar{Z}$ using the fitted polynomial functions X^{xy}. The mesh covers a rectangular 2D domain that contains the circular domain C over which the approximation of the fluid-fluid interface is defined. We used the mesh as an input and computed, among other things, the mean curvature H via difference quotients. We considered only those values of H that were obtained at points p in the interior of C, i.e., p and all neighbors of p in the mesh must be in C.

2.3.4 Experimental procedure and measurements

Performing a blob mobilization experiment involved the following major actions: (1) the tubes and flow cell were cleaned with DI water and carefully dried; (2) after filling the entire pore doublet model with liquid *code 5095*, we formed a blob by injecting 15 μl fluorescent *OHZB* liquid into Tube 1; (3) after giving the blob 2 to 3 hrs to reach equilibrium, we applied a small pumping rate of 0.03 ml/min so that the blob was not observably moved from its original position; (4) we measured the pressure on both sides of the pore doublet model; (5) we illuminated the central x-y cross-section of the blob with a laser light sheet, recorded it, and measured the 2D contact angles of the two liquid interfaces on both sides of the blob; (6) we recorded the blob's shape in 3D by recording the blob's x-y cross-sections at steps of 50 μm normal to the laser light sheet; (7) we

increased the pumping rate by an increment of 0.03 ml/min, waited 3 minutes for the flow to reach steady state, and (8) repeated steps (4) to (7) until the blob velocity exceeded 10 pixels (73 μm) per minute. At Step (5), we were able to check whether the blob was mobilized and, if so, determined the blob velocity from the 2D blob images.

2.4 Results and conclusion

2.4.1 Pressure transducer calibration

The two pressure transducers P1 and P2 were calibrated with known hydrostatic pressures. The calibration curves in **Figure 2.4** illustrate the linear response of the two pressure transducers. Their pressure/voltage ratios are 0.14651 inch(water)/mV and 0.14273

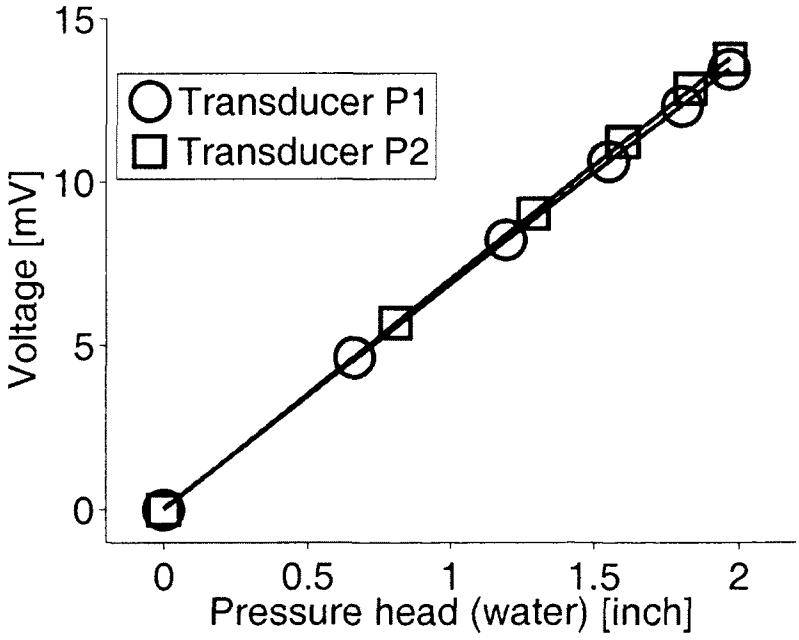

Figure 2.4: Calibration curves of the two pressure transducers P1 and P2.

inch(water)/mV with $R^2 = 0.99993$ and $R^2 = 0.99998$, respectively. The calibration curves were used to invert measured voltages to pressures.

We measured the pressure drop during steady-state single-phase flow of the liquid *code 5095* (without blob) across our pore doublet model. **Figure 2.5a** shows that the measured pressure drop agrees well with the one modeled according to Eq. (2.5) for pumping rates ranging from $Q_t = 0.01$ ml/min to 0.09 ml/min. The Reynolds number ranged from 3.5×10^{-3} to 3.15×10^{-2}. The capillary length, which is $\sqrt{\sigma/(\Delta\rho\, g)}$, was 0.076 cm, where $\Delta\rho$ is the density difference between the two liquids, and g is the gravitational acceleration. Increasing Q_t by 0.01 ml/min increased the pressure drop across the model by about 2 Pa (0.2 mm of a water column). Flow velocities in the tubes ranged from 2.3 to 20.7 m/day which roughly corresponds to flows that occur during the water flooding of oil reservoirs [19]. However, the tube radius is orders of magnitude larger than the pore size in typical reservoir rock. Therefore the pressure gradient in real reservoirs is also orders of magnitude larger than the one used in the experiment.

2.4.2 2D contact angles and blob mobilization in pore doublet model

After injecting a blob into Tube 1, we recorded the blob dynamics and pressure drop across the pore doublet model, Δp, for different pumping rates Q_t: 0, 0.03, 0.06, 0.09, 0.12, 0.15, and 0.2 ml/min. The pressure drop across the pore doublet model as a function of Q_t is shown in **Figure 2.5b** where the modeling is based on Eq. (2.9). The blob was

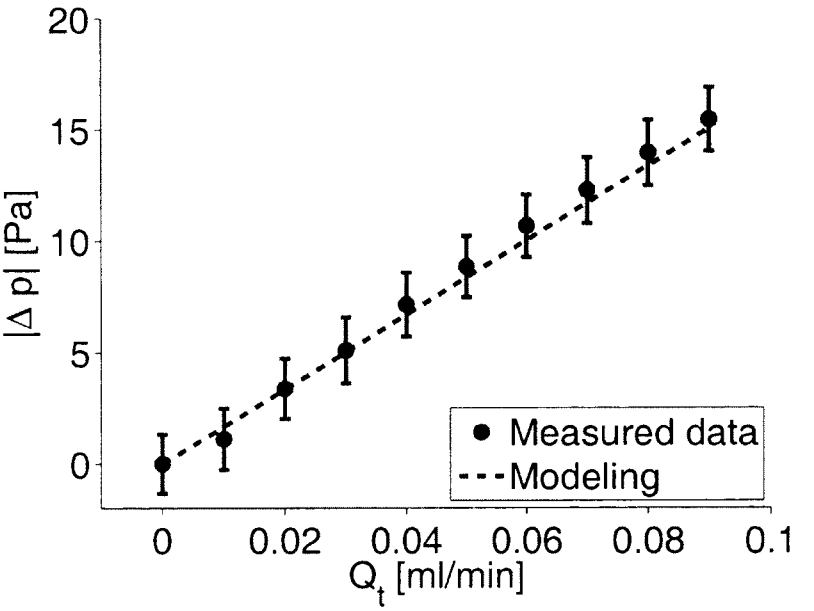

(a)

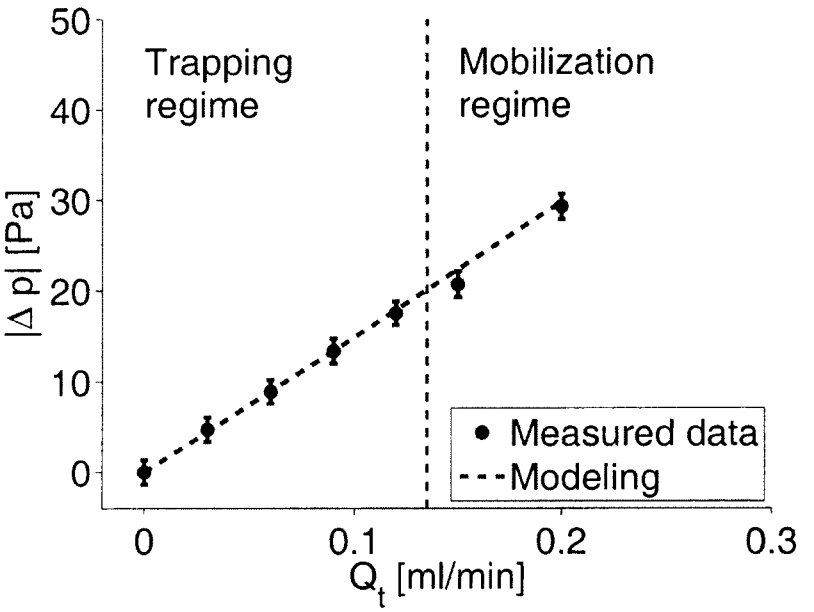

(b)

Figure 2.5: Q_t versus Δp across the pore doublet model (a) without and (b) with a 15-μl blob.

measurably mobilized at flow rates larger than a critical flow rate of 0.12 ml/min. Here "measurably" means that the blob moved more than 1 pixel (7.3 μm) per minute. The measured critical pressure drop at the critical flow rate was 17.5 Pa. A comparison of

Figure 2.5a and **b** shows that the pressure drop in the pore doublet model with a blob was larger than without a blob for all flow rates, because the blob in Tube 1 was sustaining a pressure gradient without any movement, and all the flow was through Tube 2. For flow rates $Q_t \leq 0.12$ ml/min, the measured pressure drops in **Figure 2.5b** equal the sustained pressures of the trapped blob due to the Jamin effect.

We used the image analysis tool box of Matlab^{TM} to segment the liquid and solid phases and to identify the interfaces of the blobs. We have visually compared the results of the interface identification with the original image and are confident that our image analysis did not generate significant errors.

The drainage and imbibition interfaces are shown in **Figure 2.6a/b** for different Q_t. In the pore doublet model with one blob, imbibition takes place on one side of the blob, and drainage takes place at the same time on the other side. As Q_t increases, the drainage and imbibition interfaces move to the left toward the wetting phase liquid and the nonwetting phase liquid, respectively.

The contact angles were determined through fitting polynomial curves to the interfaces. The fitted polynomial curves were represented as functions $x(y)$. There are infinitely many contact angles along the contact line of an 3D interface, but in 2D we can measure only two: at the top and the bottom of the meridian profile. These contact angles seem to be the largest and the smallest ones of all contact angles on the contact line. The top and bottom contact angles for different flow rates were calculated using Eq. (2.10) and are shown in **Figure 2.7a/b**. As Q_t increases, both the top and bottom contact angles

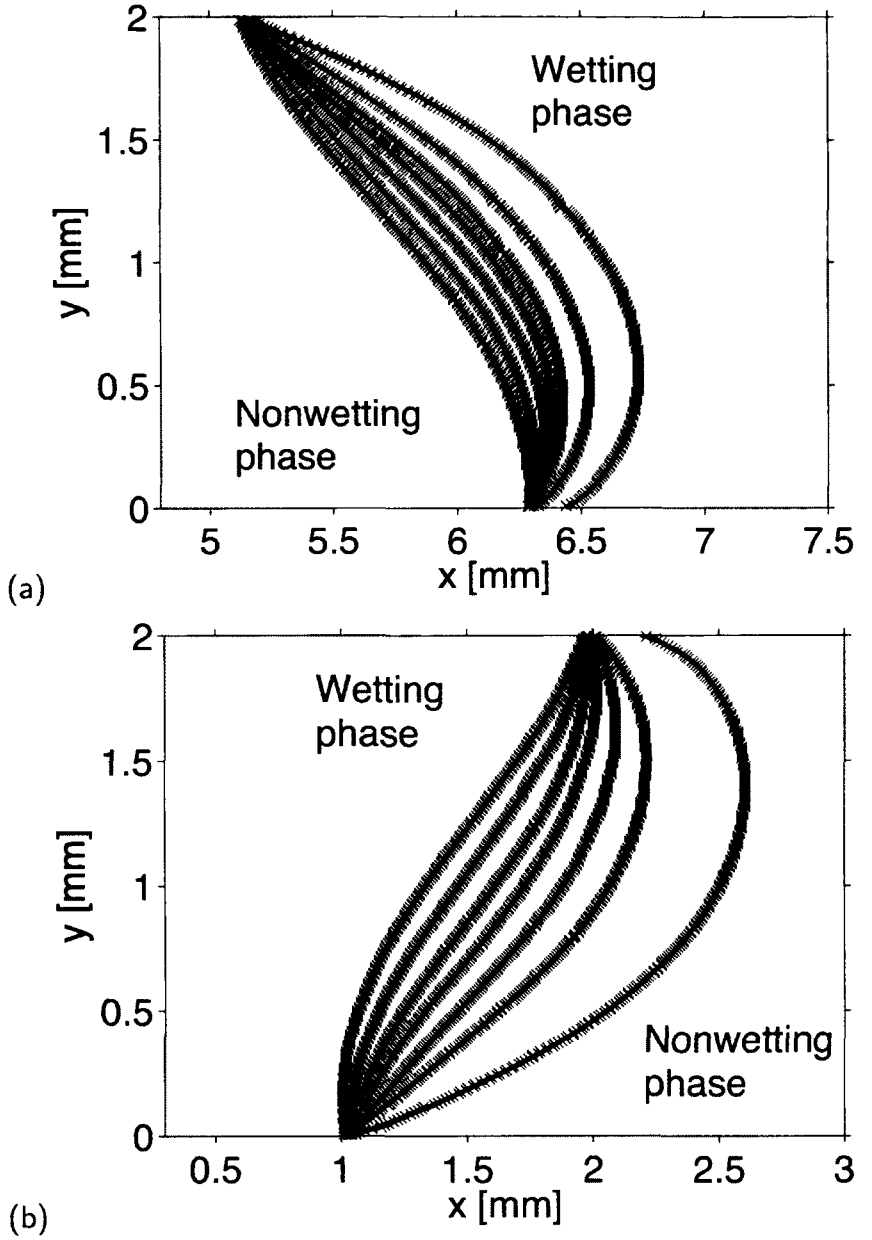

Figure 2.6: Meridian profiles of (a) drainage and (b) imbibition interfaces for different Q_t. The stars are identified interface points, and the solid lines are fitted curves. The blob is on the right side of the drainage interface and on the left side of the imbibition interface. In both plots the meridian profiles from right to left correspond to Q_t = 0, 0.03, 0.06, 0.09, 0.12, 0.15 and 0.2 ml/min.

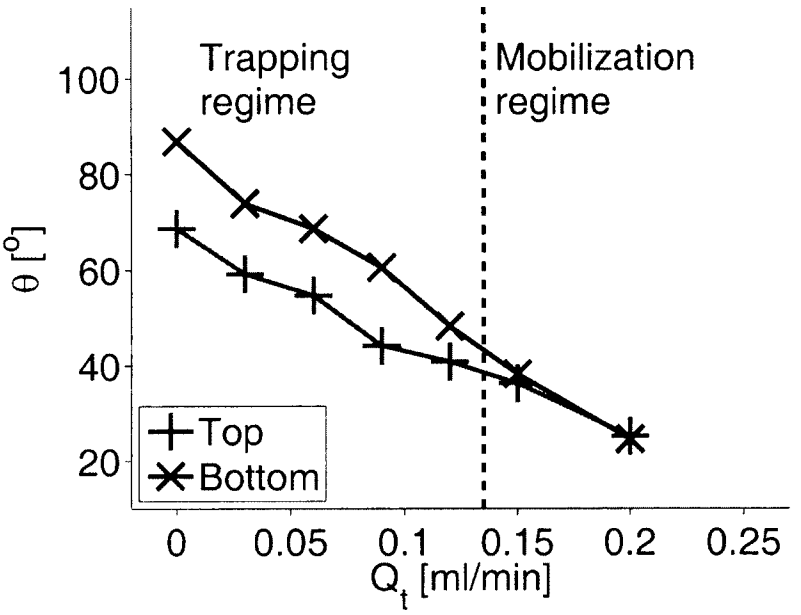

(a)

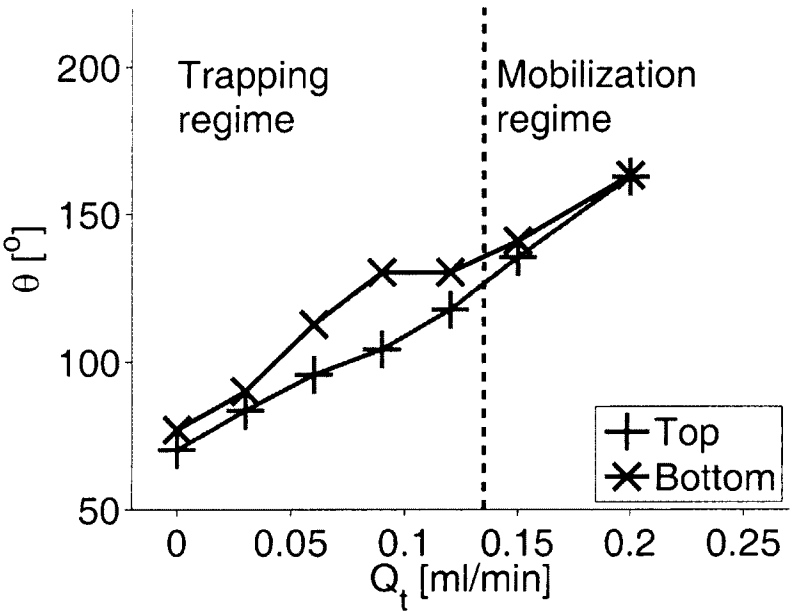

(b)

Figure 2.7: Top and bottom contact angles on (a) drainage and (b) imbibition interfaces as a function of Q_t.

decrease on the drainage interface but increase on the imbibition interface. For the same Q_t, the two 2D contact angles differ for a stationary blob (trapping regime) on both the

drainage and imbibition interfaces. This might be mainly due to contact angle hysteresis and gravity. Once a blob is mobilized (mobilization regime), the two contact angles on the drainage and imbibition interfaces are approximately equal. This suggests that a blob is only be mobilized once contact angles reach the advancing/receding contact angles.

In order to get an idea of the effect of gravity on contact angles, we relate the gravitational pressure difference across the interface, Δp_g, to the capillary pressure, p_c, [7]

$$\frac{|\Delta p_g|}{|p_c|} = \frac{|\Delta \rho g R^2|}{|\sigma \cos\theta|} \tag{2.16}$$

where $\Delta\rho$ is the density difference between the liquids, and θ is a typical contact angle. In our experiments, $|\Delta p_g|/|p_c| \approx 5$ to 7. Clearly, the effect of gravity on the meridian profiles of liquid-liquid interfaces is important, and it explains why the measured contact angles on top differ from the ones at the bottom for the same Q_t.

Using Eq. (2.9) and assuming the contact angle to be uniform on each fluid-fluid interface, the pressure drop across the pore doublet containing a blob can be written as

$$\Delta p = -\frac{2\sigma}{r_1}\left[\cos(\theta_{dr}) - \cos(\theta_{im})\right] - \frac{Q_1}{k_b}\left(\frac{r_1^4}{L_{1b}}\right)^{-1} - \frac{Q_1}{k_c}\left(\frac{r_1^4}{L_{1c}}\right)^{-1} \tag{2.17}$$

where θ_{dr} and θ_{im} are contact angles on the drainage and imbibition interfaces (in the case of a trapped blob $Q_1 = 0$). However, the two contact angles (top and bottom) measured on the meridian profile of an interface of the blob are different.

To deal with the nonuniform contact angles, three different strategies were pursued.

We replaced θ_{dr} and θ_{im} with top contact angles, bottom contact angles, and averages of the two (top and bottom) contact angles on meridians of the drainage and imbibition interfaces. The pressure drops Δp calculated by the different strategies are shown in **Figure 2.8.** The measured and predicted pressure drops resulting from the use of three different contact angles are quite similar to one another except for $Q_t = 0.2$ ml/min, at which the mobilized blob moved with the highest velocity. The three predicted pressure drops converge at the end of the trapping regime, because then the top and bottom contact angles are very close to one another. In addition, although the top and bottom contact angles differ by about 20 degrees in the blob trapping regime, the predicted pressure drops are still close to one another. This is because the pressure drops depend

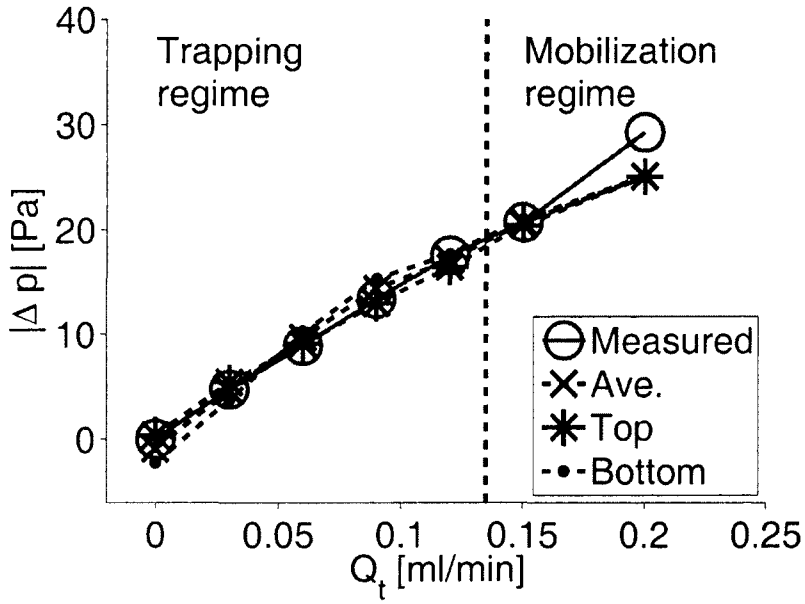

Figure 2.8: Measured and predicted pressure drops Δp versus Q_t. The modeling is based on Eq. (2.17) and uses different measured contact angles θ as an input: "Ave." is the average of top and bottom contact angles; "Top" is the top contact angle; and "Bottom" is the bottom contact angle.

on the differences of $\cos(\theta_{dr})$ and $\cos(\theta_{im})$ and not on the difference between the contact angles on the same interface. The results in **Figure 2.8** support the use of 2D contact angles to determine the pressure drop across blobs in capillary tubes even if, due to gravity, the interface of a blob is not axially symmetric.

2.4.3 3D contact angle and mean curvature

Sample 3D images of blobs reconstructed from a series of 2D images are shown in **Figure 2.9**. **Figures 2.10** and **2.11** show the distribution of the 3D contact angles calculated from Eq. (2.13) on the drainage and imbibition interfaces along the contact lines for different altitudes y. For $Q_t = 0$ when the blob was trapped, contact angles at a high altitude are smaller than the ones at a low altitude on both interfaces. We again attribute the altitude dependence of the contact angles to the effects of gravity on the initial shape of the blob. For $Q_t = 0.2$ ml/min, where the blob moved at an extremely slow pace (1.13 μm/s), the contact angles are independent of the altitude and approach what we believe to be the advancing and receding contact angles. However, two contact angles even at the same altitude (two data points with the same y values) may differ by up to $30°$. Theoretically, there should be unique values of the advancing and receding contact angles. The discrepancy between our experimental observations and our theoretical expectations are mainly due to image noise; however, microscale heterogeneity in wetting properties could also be a reason, even though we attempted to achieve homogeneous systems.

In **Figure 2.12**, we plotted the average 3D contact angles and their standard deviations

(error bars) on both contact lines as a function of Q_t. As Q_t increases, the average 3D contact angles on the drainage interface decrease, and the ones on the imbibition interface increase. The values of the average 3D contact angles are close to the average 2D contact

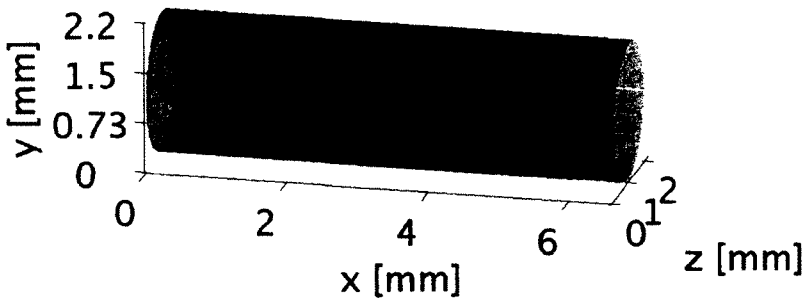

(a)

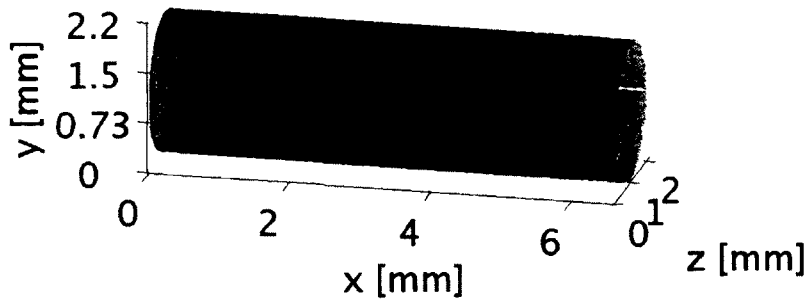

(b)

Figure 2.9: 3D blob images for (a) $Q_t = 0$ ml/min and (b) $Q_t = 0.2$ ml/min.

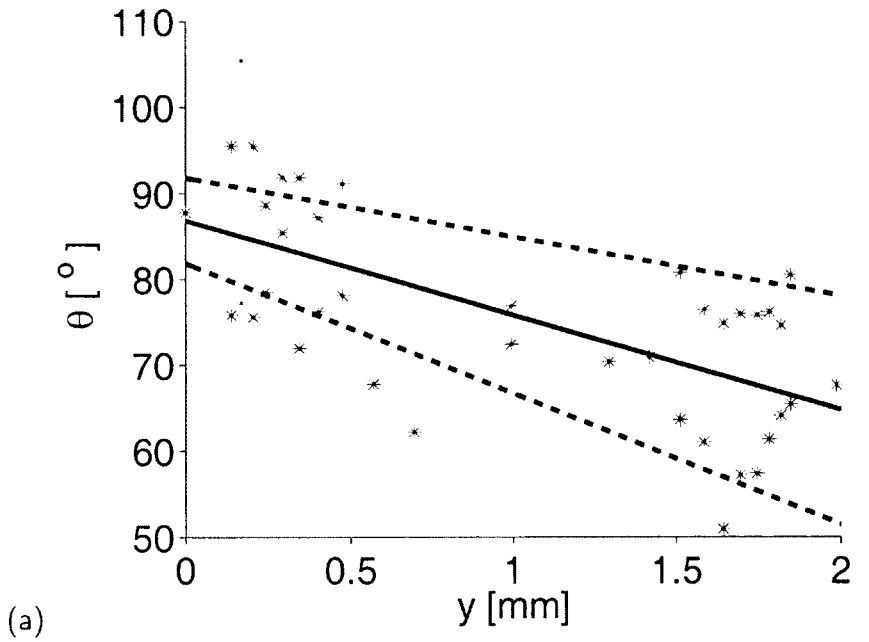

(a)

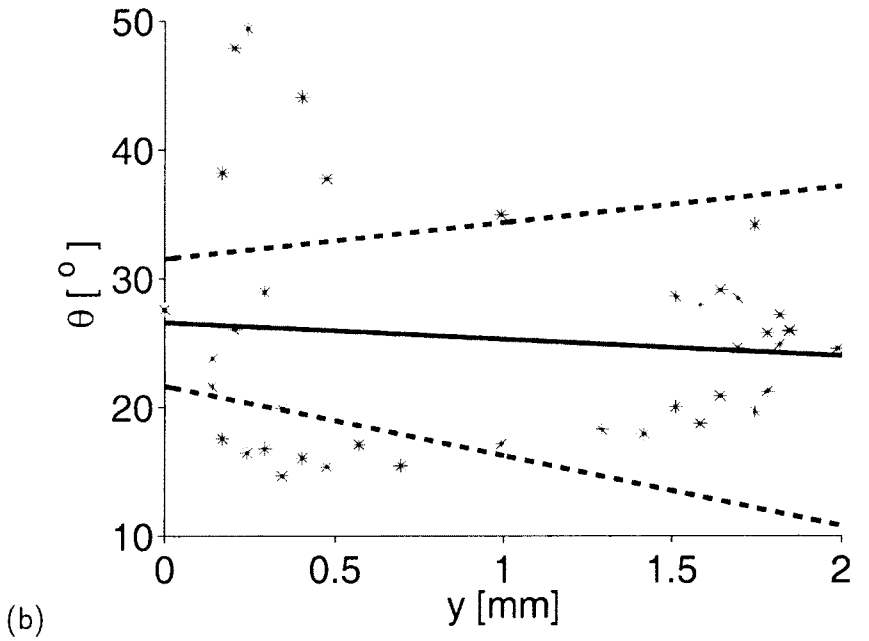

(b)

Figure 2.10: 3D contact angle θ_{3D} on drainage interface along the contact line at different heights y subject to Q_t of (a) 0 ml/min and (b) 0.2 ml/min. The solid lines are the linear regression lines and the dashed lines are the 95% confidential bounds of the regression.

angles. However, the error bars of the contact angles on both interfaces do not decrease as Q_t increases. On the imbibition interface, the error bars of contact angles even increase

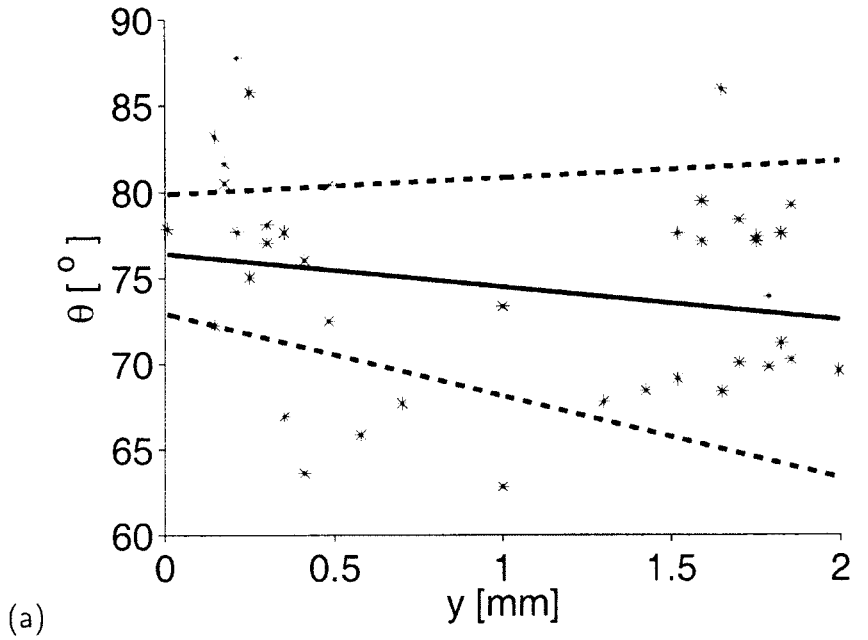

(a)

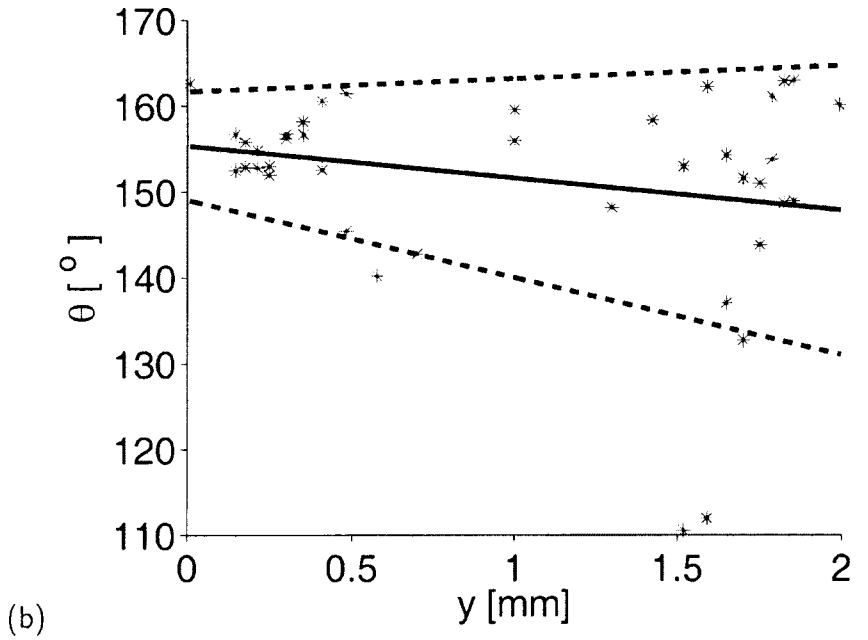

(b)

Figure 2.11: θ_{3D} on imbibition interface along the contact line at different heights y subject to Q_t of (a) 0 ml/min and (b) 0.2 ml/min. The solid lines are the linear regression lines and the dashed lines are the 95% confidential bounds of the regression.

as Q_t increases. This differs from the results for the 2D contact angles. Due to the significant image noise, we are not able to show whether the 3D contact angles along the

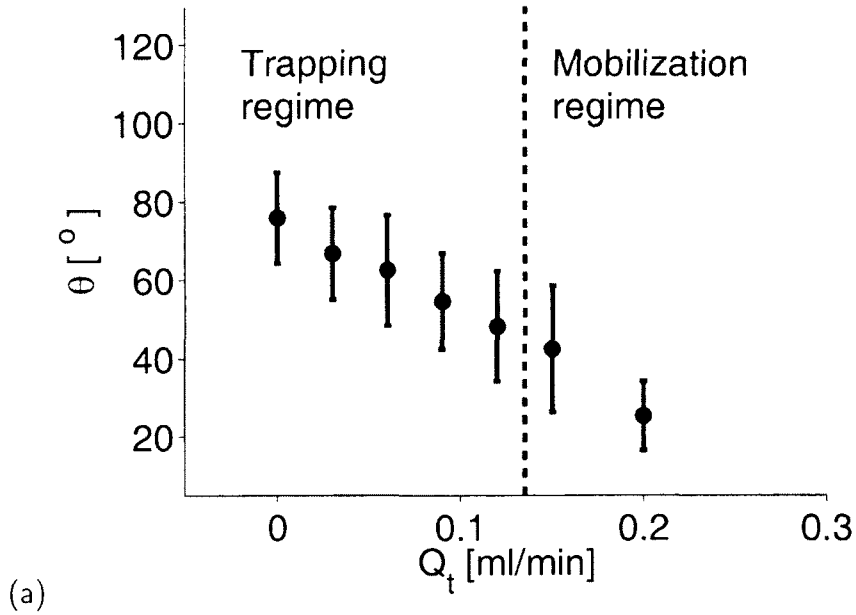

(a)

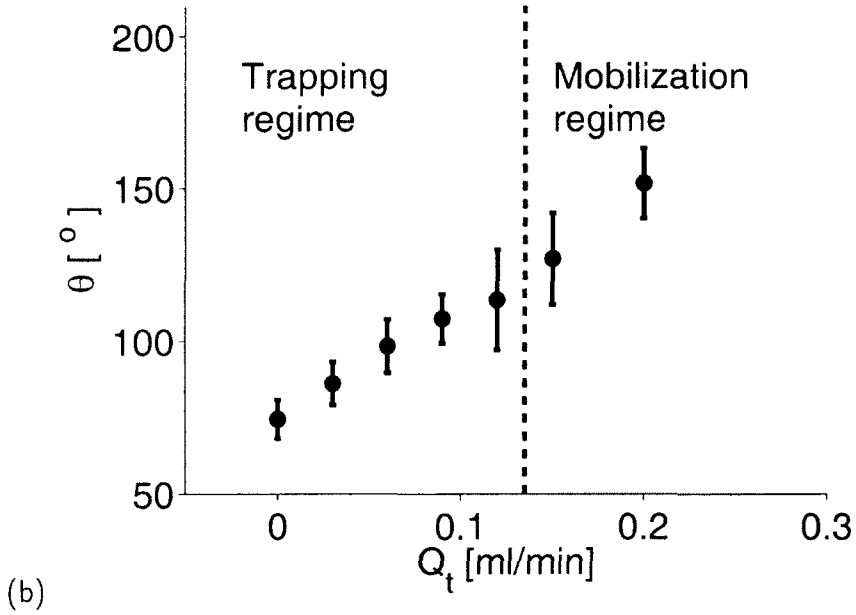

(b)

Figure 2.12: Average 3D contact angle θ_{3D} with error bar (standard deviation) at different Q_t on (a) the drainage interface and (b) the imbibition interface.

contact lines were uniform once the blob was mobilized.

The image noise might be due to the low quality of the image data used to fit the x-z polynomial curves $X^{xz}(y, z)$. In the future, we could setup another optical system

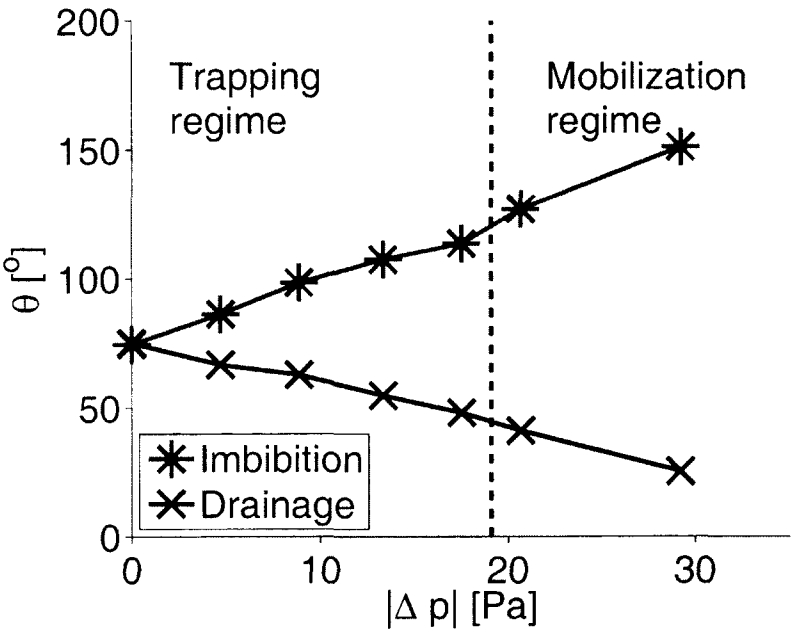

Figure 2.13: Average 3D contact angle θ_{3D} for the drainage and imbibition interfaces versus Δp.

perpendicular to the original one to simultaneously scan and record a series of 2D cross-sectional images of the blob in both the y and the z directions. This measure would increase the image resolution in the x-z plane and reduce the measurement error of the 3D contact angles.

Figure 2.13 shows how the average 3D contact angle depends on the measured pressure difference Δp. The figure clearly illustrates that the Jamin effect can be caused by a pressure gradient which results in a change in contact angles that eventually leads to blob mobilization.

To predict the pressure drop Δp from 3D contact angles via Eq. (2.17), we used the average contact angles on the two contact lines for θ_{dr} and θ_{im}. **Figure 2.14** shows that the predicted Δp agree well with the values inferred from average 2D contact angles

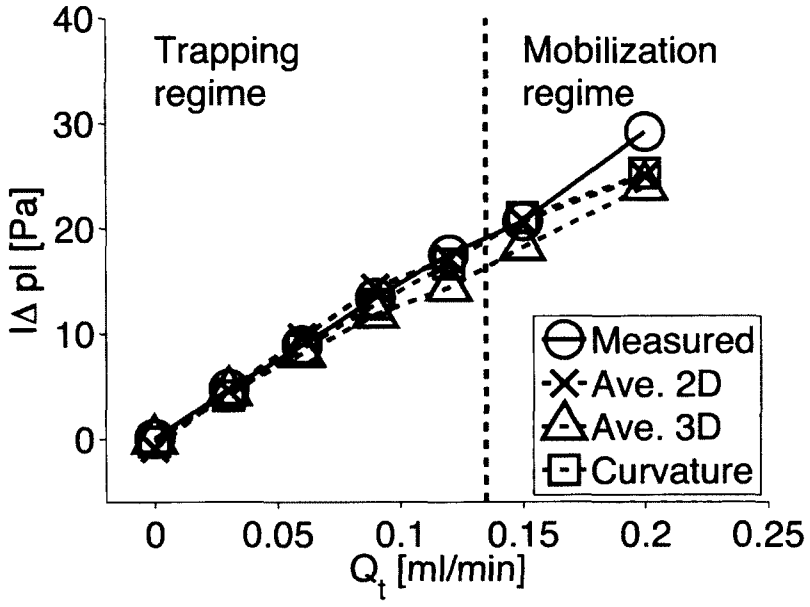

Figure 2.14: Pressure drop predictions by different methods: "ave. 2D" is the average of the 2D contact angles, "ave. 3D" is the average of the 3D contact angles, and "curvature" is the average of mean curvatures.

on the meridian profiles. Moreover, **Figure 2.8** has shown that Δp inferred from either the bottom or the top 2D contact angles on the meridian profiles agree well with the values inferred from average 2D contact angles. Therefore the predictions of the pressure drops depend only a little on the choice of the kind of contact angle, i.e. measured at the top, the bottom, or averaged. However, with the exception of $Q_t = 0.2$ ml/min, the predictions are most accurate if the average of top and bottom contact angles from the blob's meridian profile in 2D is used. Note that the blob's meridian profile is the longest of all profiles and also has the most sampling points. The predictions based on truly 3D contact angles were very close to the measured data for $Q_t = 0$ ml/min and 0.03 ml/min but deviate more from the measured data as Q_t increases. The largest deviation occurs

for $Q_t = 0.12$ ml/min and 0.15 ml/min, likely because the blob was being mobilized. For $Q_t = 0.2$ ml/min, the pressure predictions from all kinds of contact angles are very similar, although they all differ considerably from the measured value. Besides the measurement errors, we believe that Eq. (2.17) cannot full describe the pressure drops when the blob is moving. However, we have not been able to identify the physical mechanisms that our model does not adequately describe.

By using Eq. (2.15), we calculated the mean curvature H of all points on the drainage and imbibition interfaces (see **Figure 2.15** and **2.16**). Since the densities of the two liquids are significantly different, H on an interface is nonuniform in order to balance the hydrostatic pressure distributions on both sides of an interface. Unlike contact angles which involve physical-chemical complexity between liquid and solid phases, the profile of equilibrium H versus y of the interfaces of the blob is controlled only by the hydrostatic pressures [10]:

$$-\Delta\rho g y + (p_{N0} - p_{W0}) = 2\sigma H \tag{2.18}$$

where p_{N0} and p_{W0} are reference pressures of the nonwetting and the wetting phases at $y = 0$. Therefore

$$\frac{dH}{dy} = -\frac{\Delta\rho g}{2\sigma} \tag{2.19}$$

The average slope of H, dH/dy, as determined by linear regression of the data shown in **Figure 2.15a** and **2.16a** is -0.70 ± 0.02 mm^{-2}. From Eq. (2.19), we could back calculate $\sigma = 8.30 \pm 0.24$ dyne/cm. We also measured the interfacial tension with the sessile drop

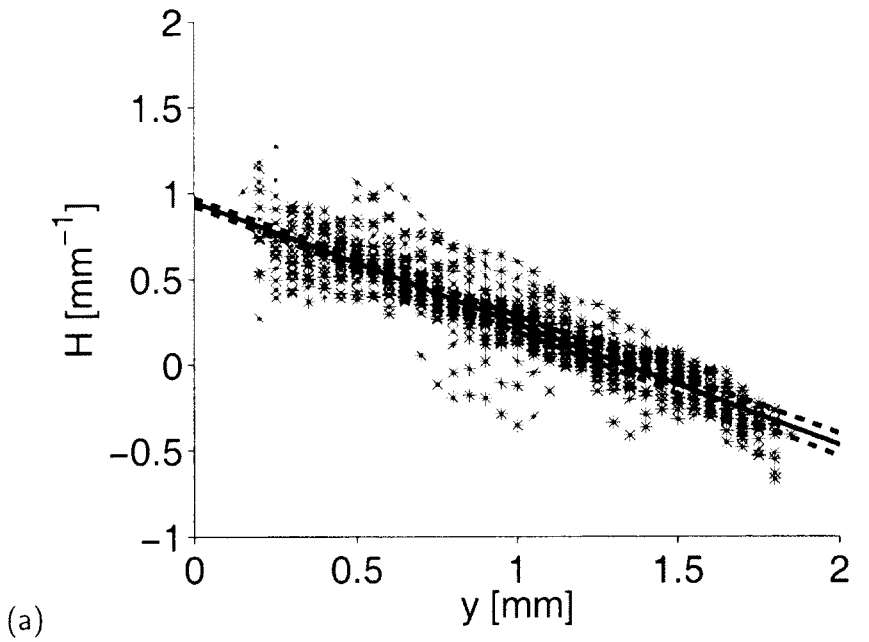

(a)

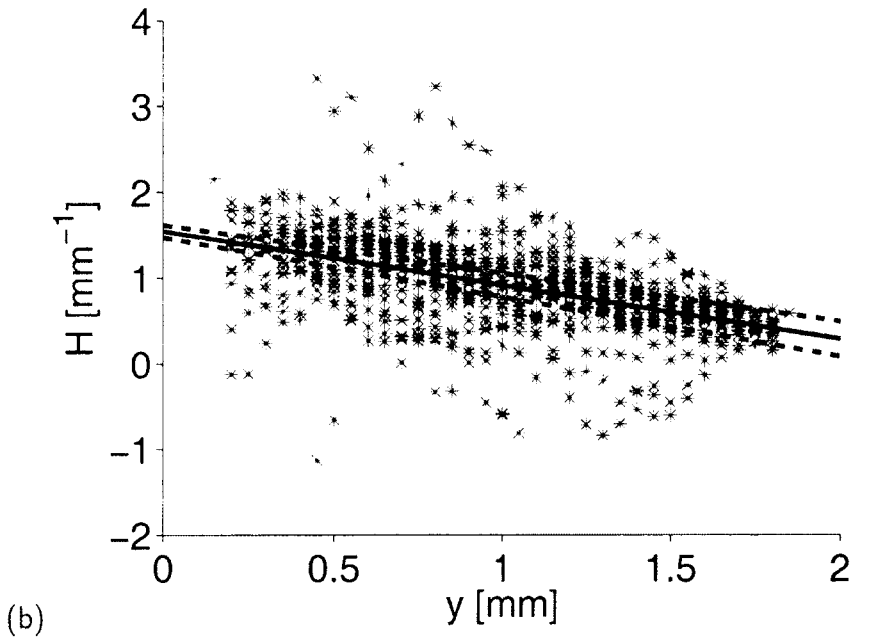

(b)

Figure 2.15: Mean curvature H on drainage interface along the contact line at different heights y subject to Q_t of (a) 0 and (b) 0.2 ml/min. The solid lines are linear regression lines and the dashed lines are the 95% confidential bounds of the regression.

method [1]. We could calculate σ by using Table I in Chapter I in Bikerman [4], because the contact angle and the aspect ratio of our sessile drop were within a certain range, and

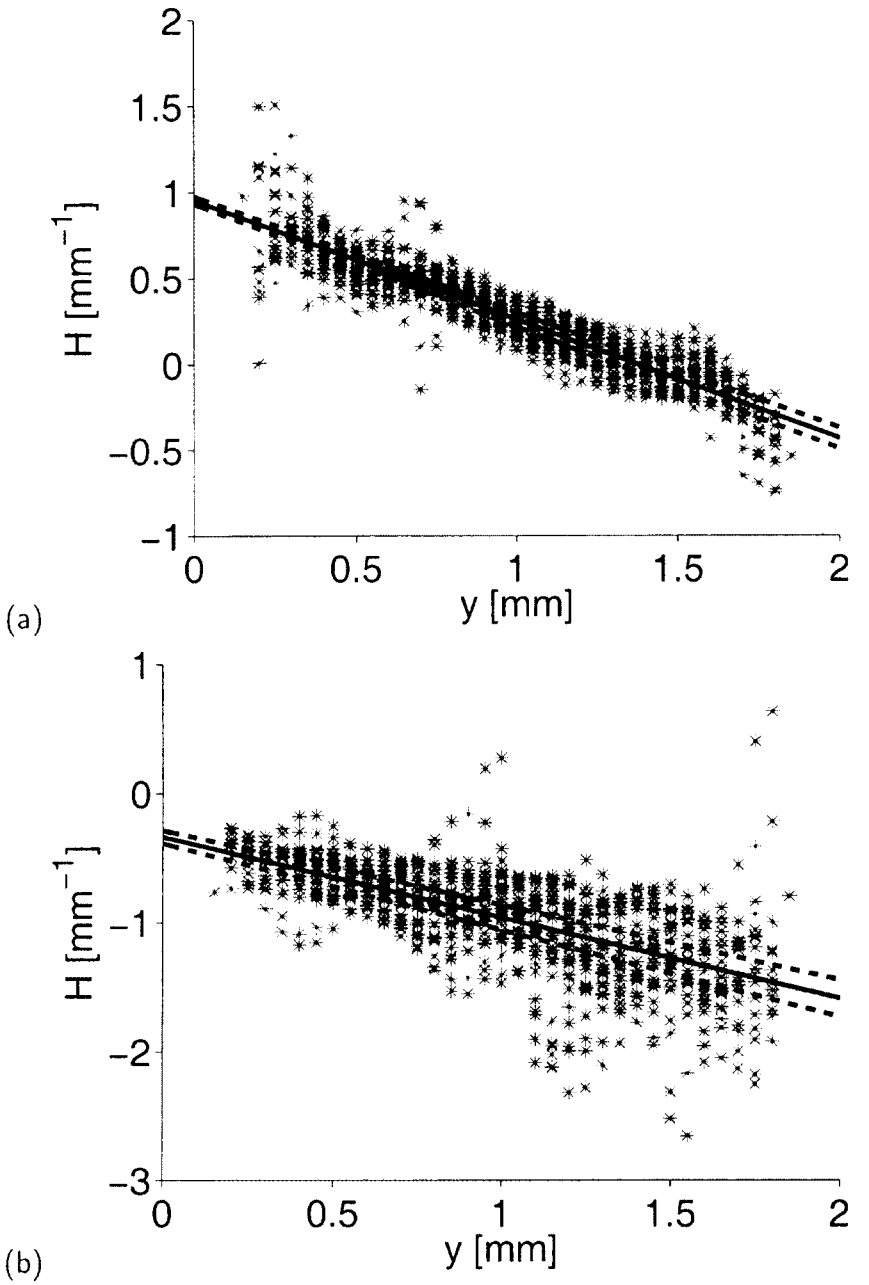

Figure 2.16: Mean curvature H on imbibition interface along the contact line at different heights y subject to Q_t of (a) 0 and (b) 0.2 ml/min. The solid lines are linear regression lines and the dashed lines are the 95% confidential bounds of the regression.

obtained $\sigma = 6.72$ dyne/cm. A limitation of our measurement was that the sessile drop was not formed on a flat surface but on the lower surface of a cylindrical acrylic tube with

a 1-cm diameter. This could explain the difference in σ between the two measurement approaches.

For each interface, we determined the average of the mean curvature and used it in Eq. (2.9) to estimate J_{dr} and J_{im}:

$$\Delta p = -2\sigma \left[\bar{H}_{dr} - \bar{H}_{im}\right] - \frac{Q_1}{k_b}\left(\frac{r_1^4}{L_{1b}}\right)^{-1} - \frac{Q_1}{k_c}\left(\frac{r_1^4}{L_{1c}}\right)^{-1} \tag{2.20}$$

where $\bar{H}_{dr}$ and $\bar{H}_{im}$ are the average mean curvatures of the drainage and the imbibition interfaces, respectively. As shown in **Figure 2.17,** $\bar{H}_{dr}$ increases, and $\bar{H}_{im}$ decreases as Q_t increases. In contrast to contact angles, the standard deviation (error bar) of the mean curvatures on both interfaces did not significantly decrease as we increased Q_t which indicates that gravity equally affects the mean curvatures for all Q_t. As shown in **Figure 2.14**, the pressure drops calculated from Eq. (2.20) were in line with the measured data and the pressure drops calculated from measured contact angles.

The various pressure predictions all differ from the measured data for $Q_t = 0.2$ ml/min. Once the blob moves, the fact that the contact angle and interface are dynamic might affect the prediction of the pressure drops based on Eq. (2.17) and Eq. (2.20). Unfortunately, the PLIF technique is still limited in its ability to measure the moving blob in 3D. We were not able to collect data for higher Q_t in the mobilization regime (only one data point from our experiments) to determine the reason for the deviation of measured data and predicted pressure drops for $Q_t = 0.2$ ml/min. To do so, one would need to record

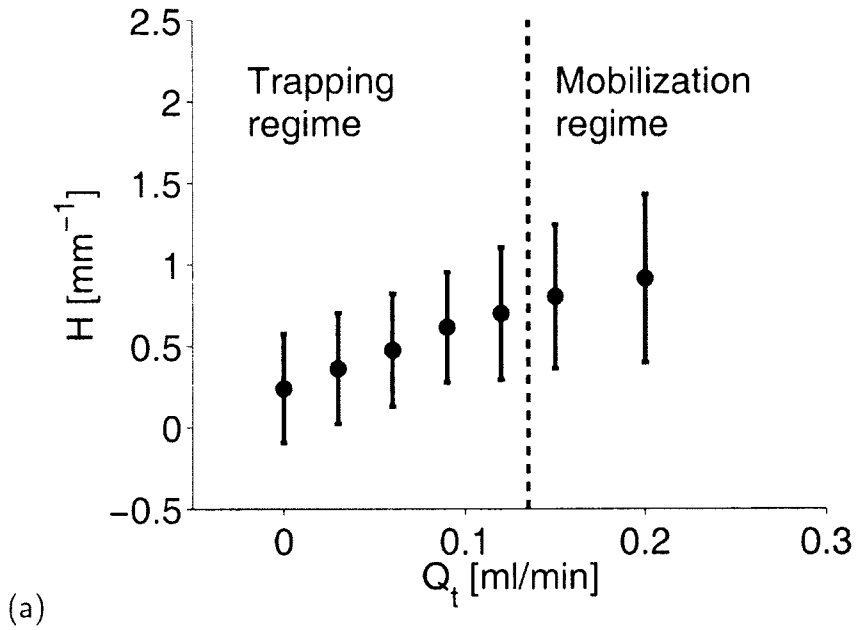

(a)

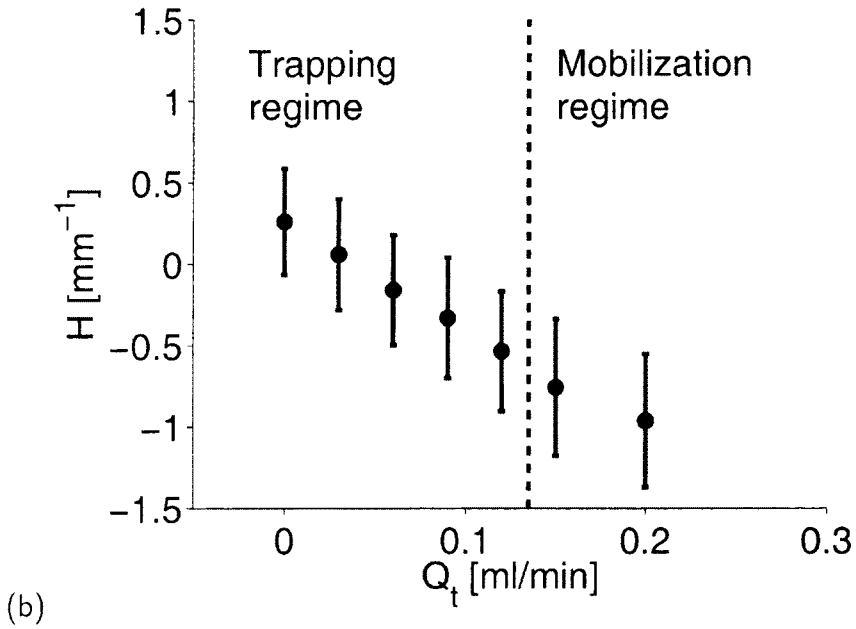

(b)

Figure 2.17: Average curvature $\bar{H}$ versus Q_t on (a) drainage and (b) imbibition interfaces.

moving blobs in real time.

2.5 Summary and discussions

Our experiments with the pore doublet model showed that the Jamin effect on a blob in a straight capillary tube can be explained entirely through contact angle hysteresis. A blob is able to sustain pressure gradients by changing its interfacial shape and its contact angles at the original contact line position. The sustained pressure gradient was not only directly measured with pressure transducers but also reasonably well predicted by our theory with measured and analyzed data from recorded blob images.

The PLIF technique was successfully used to visualize the dynamics of the meridian profile of a blob subjected to different pressure gradients created by a prescribed bypass flow. The blob meridian profiles were used to image the dynamics of the liquid-liquid interfaces and to determine 2D contact angles. The calculated pressure drops across the pore doublet model from measured 2D contact angles were in line with the directly measured ones. The top and bottom contact angles on an interface were initially different for $Q_t = 0$ due to the effects of gravity on the initial blob shape. As Q_t increased, they gradually approached the same value, which we believe to be the equilibrium advancing contact angle $\theta_A^{(eq)}$ on the imbibition interface and the equilibrium receding contact angle $\theta_R^{(eq)}$ on the drainage interface. After the blob was mobilized, the contact angles remained uniform on each of the two interfaces and assumed the dynamic contact angles $\theta_A^{(dyn)}$ or $\theta_R^{(dyn)}$. Although our theory does not describe the velocity dependence of the dynamic contact angle, it can be used to predict the trapping regime and the critical condition for blob mobilization.

Our experiments also showed the capability of the PLIF technique to acquire 3D blob images which can be used to determine 3D contact angles on the contact lines. We found that, similarly to 2D contact angles, the 3D contact angles along a contact line depend on the altitude due to contact angle hysteresis and gravity. The altitude dependence of the 3D contact angles on an interface decreased as Q_t increased, and the contact angles converged to $\theta_A^{(eq)}$ or $\theta_R^{(eq)}$ as long as the blob was trapped.

We also used 3D blob images to determine the mean curvatures of the interfaces of the blob. The mean curvature of the drainage interface increased, and the mean curvature of the imbibition interface decreased as we increased Q_t. The pressure drops calculated from mean curvatures are in line with the measured pressures and those calculated from 2D and 3D contact angles. Our PLIF-based method for calculating capillary pressure based on mean curvature measurements in a capillary tube should extend to blob mobilization studies in geometrically more complex pore shapes such as star-shaped pores [27] and to more complex porous media such as reservoir rocks. In these geometries, one cannot easily infer capillary pressure from measured contact angles due to the highly variable pore boundaries, but one can use the PLIF-based technique to measure mean curvatures. By using the Young-Laplace equation, however, one can then infer the pressure drops across a liquid-liquid interface. Our methods for determining curvature and contact angles from 3D PLIF images can also be applied to other types of images, e.g. those measured by X-ray CMT [12].

Due to the finite thickness of the laser light sheet, we could perform experiments

only in relatively large capillary tubes, such that gravity affected interfacial shapes. This was aggravated by the relatively low interfacial tension between the two index-matched liquids. Nonetheless our 1D modeling approach [Eq. (2.17) and (2.20)] agrees reasonably well with the experiments, because gravity acts in a direction that is perpendicular to the direction of flow. Although Eq. (2.17) was originally used to predict pressure drops for the case of uniform contact angles, our model still works well if the contact angles are nonuniform (by using average 2D/3D contact angles). Thus our modeling is applicable to EOR based on surfactant flushing if flow occurs in the horizontal direction, even though gravity may distort the fluid-fluid interfaces significantly due to interfacial tensions as low as 10^{-1} dyne/cm and Bond numbers exceeding 10^{-2}. Moreover, our modeling approach can be adapted to the mobilization of blobs trapped in reservoir fractures, the apertures of which can be on the order of our tube size. Then the Bond number might be similar to our experimental ones.

It is imperative to account for contact angle hysteresis when modeling blob mobilization in a straight capillary tube; otherwise there would be no blob trapping. While porous reservoir rock does not have straight pore connections, fractures in rock may posses a more or less constant aperture, at least on short length scales. Thus accounting for contact angle hysteresis might also be imperative when modeling blob mobilization in a fracture.

In our experiments, we observed significant contact angle hysteresis (about 50° for a drainage interface and 80° for an imbibition interface as shown in **Fig. 2.7**). These large

values could be due to the presumably substantial surface roughness of our pore channel made from a solid acrylic block. It seems possible that natural reservoir rock is also quite rough and chemically much more heterogeneous than our pore doublet [12]. Thus contact angle hysteresis could be significant in EOR, and it could be critical to account for it when predicting blob mobilization with standard theory based, for example, on Eqs. (2.2) and (2.3).

Finally it is of interest how contact angle hysteresis can be accounted for in emerging Darcy-scale theories for two-phase flow that can be used to describe blob mobilization during an EOR. The relative permeability should then depend on contact angle hysteresis, which decreases the mobility of residual oil blobs. Without taking contact angle hysteresis into account, the models should overestimate the relative permeability.

Bibliography

[1] A. W. Adamson and A. P. Gast. *Physical chemistry of surfaces*. John Wiley & Sons, Inc., New York, 1997.

[2] G. K. Batchelor. *An introduction to fluid dynamics*. Cambridge University Press, New York, 1967.

[3] A. Bateni, S. S. Susnar, A. Amirfazli, and A. W. Neumann. A high-accuracy polynomial fitting approach to determine contact angles. *Colloids and Surfaces A: Physicochemical and Engineering Aspects*, 219:215–231, 2003.

[4] J. J. Bikerman. *Physical surfaces*. Academic Press, New York, 1970.

[5] I. Chatzis and F. A. L. Dullien. Dynamic immiscible displacement mechanisms in pore doublets: theory versus experiment. *Journal de Physique II*, 2(11):2025–2038, 1992.

[6] C. V. Chrysikopoulos and E. T. Vogler. Acoustically enhanced ganglia dissolution and mobilization in a monolayer of glass beads. *Transport in Porous Media*, 64(1): 103–121, 2006.

[7] P. Dimon, A. P. Kushnick, and J. P. Stokes. Resonance of a liquid-liquid interface. *Journal de Physique*, 49(5):777–785, 1988.

[8] M. Dong, Q. Fan, and L. Dai. An experimental study of mobilization and creeping flow of oil slugs in a water-filled capillary. *Transport in Porous Media*, 80:455–467, 2009. doi: 10.1007/s1122-009-9374-5.

[9] D. R. Gardescu. Behavior of gas bubbles in capillary spaces. *Trans. AIME*, 86:351, 1930.

[10] Y. Gu and C. Yang. The effects of capillary force and gravity on the interfacial profile in a reservoir fracture or pore. *Journal of Petroleum Science & Engineering*, 40(1-2): 77–87, 2003.

[11] M. Hilpert. Effects of dynamic contact angle on liquid infiltration into horizontal capillary tubes: (semi)-analytical solutions. *Journal of Colloid and Interface Science*, 337(1):131–137, 2009.

[12] C. J. Landry, Z. T. Karpyn, and M. Piri. Pore-scale analysis of trapped immiscible fluid structures and fluid interfacial areas in oil-wet and water-wet bead packs. *Geofluids*, 11(2):209–227, 2011.

[13] M. Lipschultz. *Differential Geometry*. McGraw-Hill, New Jersey, 1969.

[14] B. L. Longino and B. H. Kueper. Effects of capillary pressure and use of polymer

solutions on dense non-aqueous-phase liquid retention and mobilization in a rough-walled fracture. *Environmental Science & Technology*, 33(14):2447–2455, 1999.

[15] J. C. Melrose and C. F. Brandner. Role of capillary force in determining microscopic displacement efficiency for oil recovery by waterflooding. *Can. J. Petrol. Technol.*, 13(4):54–62, 1974.

[16] J. W. Mercer and R. M. Cohen. A review of immiscible fluids in the subsurface: properties, models, characterization and remediation. *Journal of Contaminant Hydrology*, 6(2):107–163, 1990.

[17] C. D. Montemagno and W. G. Gray. Photoluminescent volumetric imaging –A technique for the exploration of multiphase flow and transport in porous media. *Geophysical Research Letters*, 22(4):425–428, 1995.

[18] N. R. Morrow. The effects of surface roughness on contact angle with special reference to petroleum recovery. *The Journal of Canadian Petroleum Technology*, 14(4): 42–53, 1975.

[19] N. R. Morrow. Interplay of capillary, viscous and buoyancy forces in the mobilization of residual oil. *The Journal of Canadian Petroleum Technology*, 18(3):35–46, 1979.

[20] N. R. Morrow. Wettability and its effect on oil recovery. *Journal of Petroleum Technology*, 42(12):1476–1484, 1990.

[21] K. M. Ng and A. C. Payatakes. Stochastic simulation of the motion, breakup and

stranding of oil ganglia in water-wet granular porous media during immiscible displacement. *American Institute of Chemical Engineers Journal*, 26(3):419–429, 1980.

[22] K. M. Ng, H. T. Davis, and L. E. Scriven. Visualization of blob mechanics in flow through porous media. *Chemical Engineering Science*, 33(8):1009–1017, 1978.

[23] K. D. Pennell, G. A. Pope, and L. M. Abriola. Influence of viscous and buoyancy force on the mobilization of residual tetrachloroethylene during surfactant flushing. *Environmental Science & Technology*, 30(4):1328–1335, 1996.

[24] L. N. Reddi and S. Challa. Vibratory mobilization of immiscible liquid ganglia in sands. *Journal of Environmental Engineering ASCE*, 120(5):1170–1190, 1994.

[25] E. Rillaerts and P. Joos. The dynamic contact angle. *Chemical Engineering Science*, 35(4):883–887, 1980.

[26] W. Rose and R. W. Heins. Moving interfaces and contact angle rate-dependency. *Journal of Colloid Science*, 17(1):39–48, 1962.

[27] A. V. Ryazanov, M. I. J. van Dijke, and K. S. Sorbie. Two-phase pore-network modeling: existence of oil layers during water invasion. *Transport in Porous Media*, 80(1):79–99, 2009.

[28] M. R. Sasges and C. A. Ward. Effect of gravity on contact angle: An experimental investigation. *Journal of Chemical Physics*, 109(9):3661–3670, 1998. doi: 10.1063/1.476962.

[29] W. O. Smith and M. D. Crane. The Jamin effect in cylindrical tubes. *J. Am. Chem. Soc.*, 52(4):1345–1349, 1930.

[30] J. J. Taber. Dynamic and static forces required to remove a discontinuous oil phase from porous media containing both oil and water. *Soc. Pet. Eng. J.*, 9(3):3–12, 1969.

Chapter 3. Theoretical and Experimental Study of Resonance of Blobs in Porous Media

Abstract

We theoretically and experimentally investigated the frequency response of blobs in porous media to an oscillatory pressure difference. To predict the frequency response analytically, we formulated a simple model pore system consisting of a blob in a capillary tube. This model accounts for the frequency-dependent viscous pressure drops in the blob and the surrounding liquid and for the dynamic capillary pressure that occurs due to contact line pinning. By using the planar laser-induced fluorescence technique, we visualized the dynamic response of blobs in porous media. As predicted by our theory, both air and liquid blobs surrounded by an immiscible liquid exhibited resonance in a capillary tube. Furthermore, we showed, for the first time, that a liquid blob in a sphere-packing medium exhibits resonance.

3.1 Introduction

Subsurface porous media are frequently saturated by two or more immiscible fluids, one of which may consist of disconnected blobs which may occupy one or more pores [26]. For instance, groundwater reservoirs often contain gas bubbles, and oil reservoirs contain residual oil blobs after having been water-flooded. The interactions between fluid blobs and seismic waves are important in several respects. The relative movement between blobs and the pore skeleton affects wave attenuation [20] according to Biot's theory [7]. Seismic waves can be used to mobilize trapped oil or non-aqueous phase liquid (NAPL) blobs [3, 37, 36, 23, 4]. Moreover, seismic waves enhance the dissolution of trapped nonwetting phase blobs [38, 11].

Hilpert et al. [20] derived theoretically the frequency response of trapped blobs and predicted that blobs may exhibit resonance. Since they examined oscillating liquid blobs in the low-frequency regime, in which the wavelength is much larger than the blob length, the liquids were assumed to be incompressible. Numerical simulations have also shown that blobs trapped in 2D porous media exhibit resonance [18]. The predicted resonance has been linked to other geophysical applications. It has been hypothesized that trapped blobs can be optimally mobilized by exciting them at their resonant frequencies [20]. Blob resonance has also been linked to a passive seismic technology used to detect hydrocarbon reservoirs. Holzner et al. [21] attribute high correlations between the presence of hydrocarbon reservoirs and low-frequency spectral anomalies computed from passively recorded seismic data to the resonance of hydrocarbon blobs. However, Broadhead [8] tested var-

ious resonance amplification models to show that the resonant frequency of blobs is too high to fall in the frequency range of hydrocarbon microtremor. To summarize, it is important to know how liquid blobs respond to excitation as a function of frequency and whether resonance actually occurs in subsurface porous media.

Few experimental studies have been performed that demonstrate the occurrence of blob resonance in porous media. Hilpert and Miller [19] used optical microscopy to show that a water slug in a PTFE tube may resonate under acoustic excitation. Bian et al. [5] used high-speed video imaging to show as well that water slugs in cylindrical tubes exhibit resonance. However, it has not been shown experimentally that blobs in the topologically complex pore spaces that occur in subsurface environments may resonate.

An image taken of a blob inside a complex 3D porous medium is usually optically distorted due to the different optical refractive indices of the solid and the liquid phases. Therefore, most studies on the dynamics of menisci/blobs in porous media were limited to steady-state forcing and were performed in capillary tubes and mono-layer sphere packings [34, 9, 11, 29, 4]. An exception is the study by Ng et al. [28] who examined blob mobilization in a sphere packing. They matched the refractive index of the liquid that surrounded the blob with the one of the solid phase and illuminated their flow cell with background light. This measure significantly improves the image quality; however, different menisci of a blob may overlap in the acquired images because the blob is not index-matched.

In this paper, we use flow visualization experiments based on the planar laser-induced fluorescence (PLIF) technique to show that blobs in capillary tubes and sphere packings

may represent resonating systems. PLIF was introduced in the late 1970's and has been used to examine many types of flow including flow in porous media [13, 32, 24, 15, 42, 45, 33, 12, 25, 1, 30, 44, 27, 35, 16, 43, 31, 22]. PLIF allows us to acquire undistorted cross-sectional images of blobs in complex porous media at a high temporal resolution. Therefore, we can resolve blob motion within an excitation cycle in case of oscillatory forcing. Using a simple model pore system that consists of a capillary tube, we derive an analytical expression for the frequency response of a trapped liquid blob in the low-frequency regime in which the liquids can be assumed to be incompressible. In contrast to previous work [20, 18], our new theory accounts for the viscous pressure drops in the fluid that surrounds the blob. This generalization is necessary, because the pressure sensors used in our experiments measure the pressure drop in the surrounding fluid.

The analytical theory is developed in Section 2. Section 3 is devoted to the introduction of the apparatus and experiment procedure. In Section 4, we present and discuss the experimental results. Section 5 summarizes our findings, which show that trapped blobs indeed exhibit resonance in porous media.

3.2 Theory

In our model pore system (a cylindrical capillary tube), a nonwetting blob is surrounded by another immiscible wetting liquid (see **Figure 3.1**). Initially, the blob is in equilibrium with contact angles θ_0. If a pressure difference across the blob, P_w, is applied that is small enough for the contact lines to remain pinned, the shape of blob menisci will change as

illustrated in **Figure 3.1**. The forcing will cause a cross-sectional mean fluid displacement $\bar{z}$ which may depend on time.

The pressure difference P_w can be decomposed into five different pressure differences:

$$P_w = P_w^- + P_w^+ + P_n + P_c^- - P_c^+ \tag{3.1}$$

where P_w^- and P_w^+ are the viscous pressure drops in the wetting liquid slugs of lengths L_w^- and L_w^+, respectively, P_n is the viscous pressure drop in the nonwetting blob of length L_n, and P_c^+ and P_c^- are the nonequilibrium capillary pressures (i.e., the difference between actual and equilibrium capillary pressure) of the right and left meniscus, respectively. Here and in the following, subscripts w and n indicate that a variable is associated with the wetting liquid and the nonwetting blob, respectively. Superscripts $+$ and $-$ indicate that a variable is associated with the right and left meniscus (positive and negative z-direction),

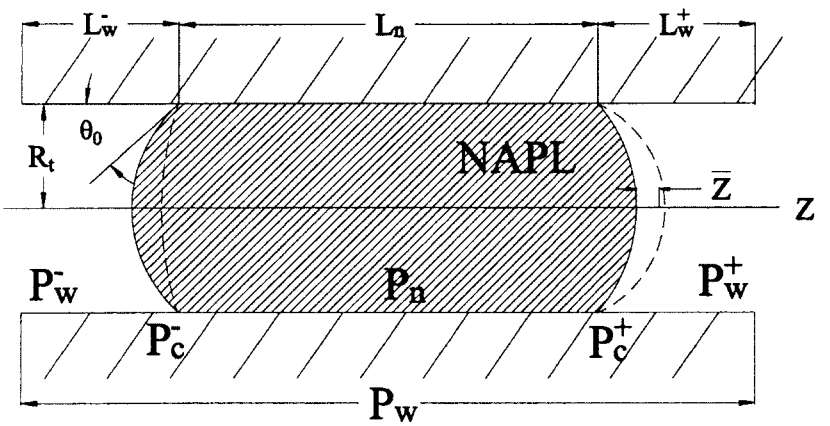

Figure 3.1: A blob in a cylindrical tube with circular cross-section and radius R_t. L_w and L_n are the lengths of the wetting and non-wetting liquid slugs, respectively. The two solid lines represent the liquid-liquid interfaces in the equilibrium state, and two dashed lines represent the interfaces in a non-equilibrium state.

respectively.

Starting with the flow in the section occupied by the nonwetting liquid, we now consider an oscillatory pressure difference $P_n(t) = P_n(\omega)e^{-i\omega t}$ with angular frequency ω that is acting on the blob of length L_n. Since the total length of the fluid slugs is sufficiently longer than the radius of the tube R_t, we can assume the flow to be axia-symmetric and oriented along the tube axis. The Navier-Stokes equation then becomes

$$\rho_n \frac{\partial u(r,t)}{\partial t} = -\frac{P_n(\omega)}{L_n} e^{-i\omega t} + \eta_n \Delta u(r,t) \tag{3.2}$$

where $u(r,t)$ is the fluid velocity, r is the radial coordinate, η_n is the dynamic viscosity, and ρ_n is the density. A harmonic solution $u(r,t) = u(r,\omega)e^{-i\omega t}$ can be derived where

$$u(r,\omega) = -\frac{iP_n(\omega)}{L_n \rho_n \omega}\left[1 - \frac{J_0\left(\sqrt{i}\frac{r}{\xi}\right)}{J_0\left(\sqrt{i}\frac{R_t}{\xi}\right)}\right]$$

is the complex velocity amplitude, J_0 is the Bessel function of order zero, and $\xi = \sqrt{\eta_n/(\rho_n\omega)}$ is the viscous penetration depth. The amplitude of the cross-sectional mean velocity is

$$\overline{u}(\omega) = -\frac{iP_n(\omega)}{L_n \rho_n \omega} h(X_n) \tag{3.3}$$

where

$$h(X_n) = -\frac{J_2(\sqrt{iX_n})}{J_0(\sqrt{iX_n})}$$

J_2 is the Bessel function of order two, $X_n = \omega/\omega_{cn}$ is a nondimensional excitation fre-

quency, and

$$\omega_{cn} = \frac{\eta_n}{\rho_n R_t^2} \tag{3.4}$$

is the characteristic frequency. We extend Eq. (3.3) to the flows in the sections occupied by the wetting liquid through

$$\overline{z}(\omega) = \frac{P_w^-(\omega)h(X_w)}{L_w^-\rho_w\omega^2} = \frac{P_w^+(\omega)h(X_w)}{L_w^+\rho_w\omega^2} = \frac{P_n(\omega)h(X_n)}{L_n\rho_n\omega^2} \tag{3.5}$$

where $X_w = \omega/\omega_{cw}$ and

$$\omega_{cw} = \frac{\eta_w}{\rho_w R_t^2} \tag{3.6}$$

The liquid displacement $\overline{z}$ is equal in each liquid section because of the assumed incompressible flow. By assuming that the menisci have the shapes of spherical caps and using the Young-Laplace equation, $P_c = 2\sigma\cos\theta/R_t$, the nonequilibrium capillary pressures in Eq. (3.1) becomes

$$P_c^{\pm}(\omega) = \pm\frac{dP_c^{\pm}}{d\theta}\frac{d\theta}{d\overline{z}_{sp}}\overline{z}_{sp}(\omega) \tag{3.7}$$

where σ is interfacial tension,

$$\frac{d\overline{z}_{sp}}{d\theta} = -\frac{R_t}{(1+\sin\theta)^2} \tag{3.8}$$

and the subscript sp of $\overline{z}$ indicates the occurrence of a spherical cap.

By substituting Eqs. (3.5) and (3.7) into Eq. (3.1), one can obtain the nondimensional

frequency response function of the blob in the tube

$$\frac{\overline{z}_{sp}(\omega)}{P_w(\omega)}[\rho_n L_n + \rho_w L_w]\omega_{cn}^2 = \underbrace{\left\{\left[\frac{1}{(1+\lambda)h(X_w)} + \frac{1}{(1+\lambda^{-1})h(X_n)}\right] X_n^2 - X_0^2\right\}^{-1}}_{\chi(X_n, X_w, X_0)} \quad (3.9)$$

where $\lambda = \rho_n L_n/(\rho_w L_w)$ is the mass ratio between the nonwetting phase blob and the two surrounding wetting liquid slugs that have a total length $L_w = L_w^- + L_w^+$, $X_0 = \omega_0/\omega_{cn}$ is the nondimensional resonant frequency of the undamped system, and

$$\omega_0 = \sqrt{\frac{4\sigma}{(L_n\rho_n + L_w\rho_w)R_t^2}\sin\theta_0(1+\sin\theta_0)^2} \quad (3.10)$$

is the corresponding dimensional resonant frequency.

However, $\overline{z}_{sp}$ is not easy to determine experimentally since this requires imaging the dynamics of an entire fluid-fluid interface. It is much easier to measure the mean displacement of the meridian profile $\overline{z}_{mp}$ of the meniscus, i.e., the cross-sectional profile that passes through the center of the meniscus. The meridian profile has been used for decades to study dynamics of 3D menisci and blobs [39, 9, 41, 17, 22]. From Eq. (3.9), we can now derive a frequency response in terms of $\overline{z}_{mp}$:

$$\chi(X_n, X_w, X_0) = \frac{\overline{z}_{mp}(\omega)}{P_w(\omega)}[\rho_n L_n + \rho_w L_w]\omega_{cn}^2 \frac{d\overline{z}_{sp}}{d\overline{z}_{mp}}(\theta_0) \quad (3.11)$$

where

$$\frac{d\bar{z}_{sp}}{d\bar{z}_{mp}}(\theta) = \frac{2}{(1+\sin\theta)^2}\left[2 - \frac{\pi - 2\theta - \sin(2\theta)}{2}\frac{\sin(2\theta)}{\cos^4(4\theta)}\right]^{-1} \tag{3.12}$$

When both $\omega \ll \omega_{cn}$ and $\omega \ll \omega_{cw}$, we can determine a simple condition for resonance by employing a Taylor series expansion of $h(X)$ around $X_{n,w} = 0$:

$$h(X_{n,w}) \approx -\frac{iX_{n,w}}{8 - 2iX_{n,w}} \tag{3.13}$$

Therefore

$$\frac{1}{|\chi|^2} \approx X_0^4 + \left[4X_0^2 - 64(\alpha\Lambda + \Lambda')^2\right] X_n^2 + O\left(X_n^4\right) \tag{3.14}$$

where $\beta = \omega_{cw}/\omega_{cn}$, $\Lambda = 1/(1+\lambda)$ and $\Lambda' = 1/(1+\lambda^{-1})$. Therefore the resonance criterion becomes

$$\frac{1}{(\beta\Lambda + \Lambda')^2} X_0^2 > 16 \tag{3.15}$$

For instance, if the kinematic viscosities of both fluids are equal, $\beta = 1$, and if the mass ratio $\lambda = 1$, the blob system exhibits resonance only if $X_0 > 4$. **Figure 3.2** illustrates the frequency response function of two blob systems with different X_0 values for $\beta = 1$ and $\lambda = 1$. Clearly, the occurrence of resonance depends on the ratio of viscosities and densities of the two liquids, β, the mass ratio λ, and the nondimensional natural resonant frequency X_0.

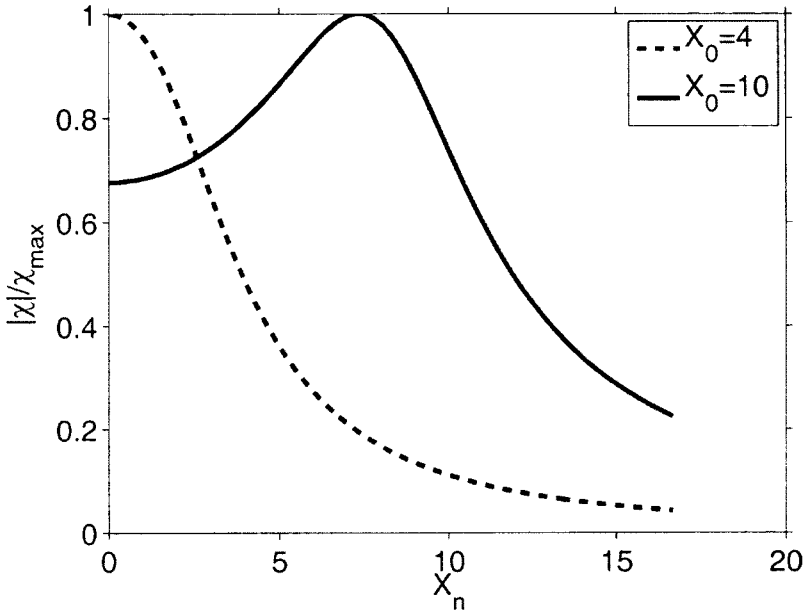

Figure 3.2: Normalized frequency response curves of an underdamped ($X_0 = 10$) and an overdamped ($X_0 = 4$) blob in a capillary tube.

3.3 Experimental methods

3.3.1 Experimental setup

To observe the movement of the menisci of a blob in a porous medium, we applied the planar laser-induced fluorescence (PLIF) technique, a noninvasive method [27, 22]. In our experimental setup (**Figure 3.3**), we matched the optical refractive indices of the liquids and the solid phase. The piston of a syringe was connected to a PC-controlled actuator (ETREMA Products. INC., AA250LLS). The syringe in turn was connected to a flow cell with flexible PTFE tubing (Cole-Parmer) in order to avoid the transmission of vibrations of the actuator to the flow cell. The other side of the flow cell was connected to the liquid reservoir which provided a constant pressure boundary condition. The flow

cell which contained a blob was illuminated by a laser light sheet.

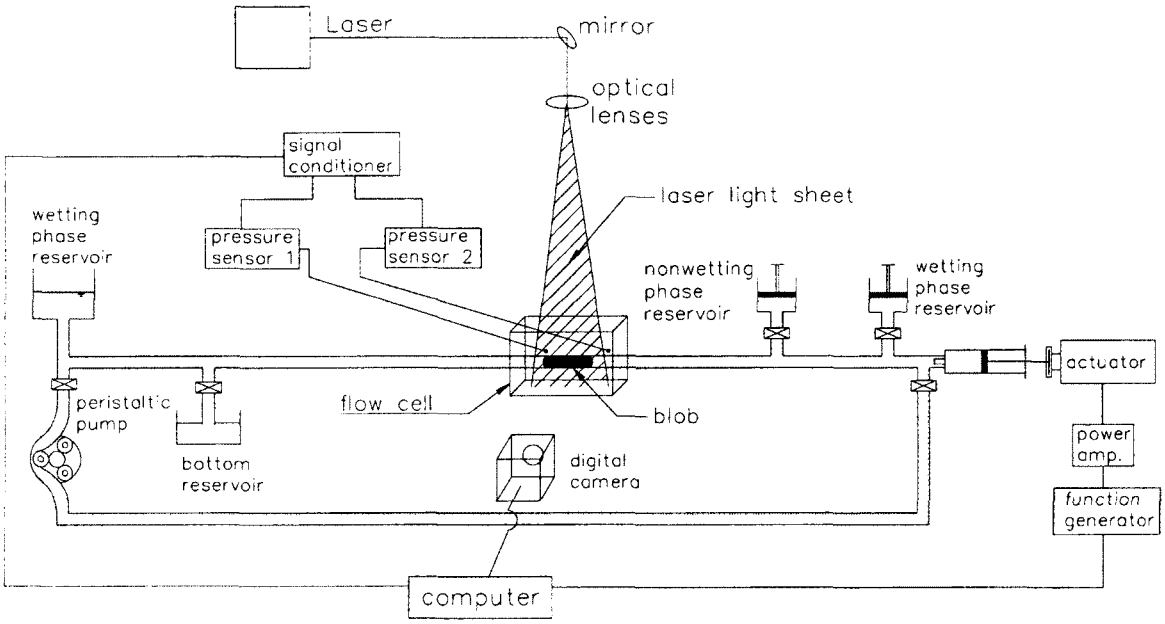

Figure 3.3: Sketch of our experimental setup.

In addition to the optically-index matched experiments, we also performed experiments with air blobs surrounded by water. Since the refractive indices of air and water are different, we used uniform background light, instead of a laser light sheet, to illuminate the flow cell. **Figure 3.4** shows a sample image of an air blob. Even though the air blob images that we took were of lesser quality than the liquid-blob images from the PLIF experiments, the experiments allowed us to test whether resonance also occurs for blobs with a significantly lower density and viscosity.

Two acrylic flow cells, "Cell T" and "Cell S", were designed to simultaneously record blob displacement and to measure the pressure drop across a blob. Cell T contains a straight capillary tube with radius of 1 mm. Cell S contains a cylindrical cavity with 10

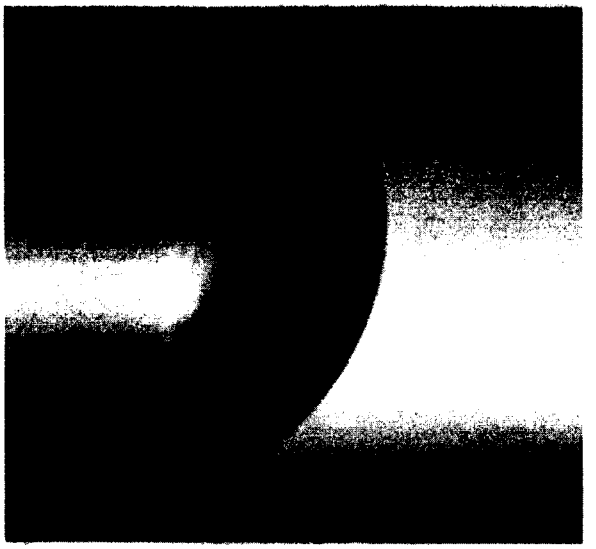

Figure 3.4: Image of one meniscus of an air blob in Cell T illuminated by uniform background light.

mm diameter and 20 mm length and was filled with acrylic beads with diameter of 3 mm. **Figure 3.5** shows Autocad^{TM} drawings of the flow cells. Into one side of each flow cell, two threaded holes were drilled for mounting pressure transducers for measuring the fluid pressure on both sides of the porous medium. A vertical hole was drilled into Cell S between the two holes for the pressure transducers. This hole allowed us to inject a blob into the sphere packing.

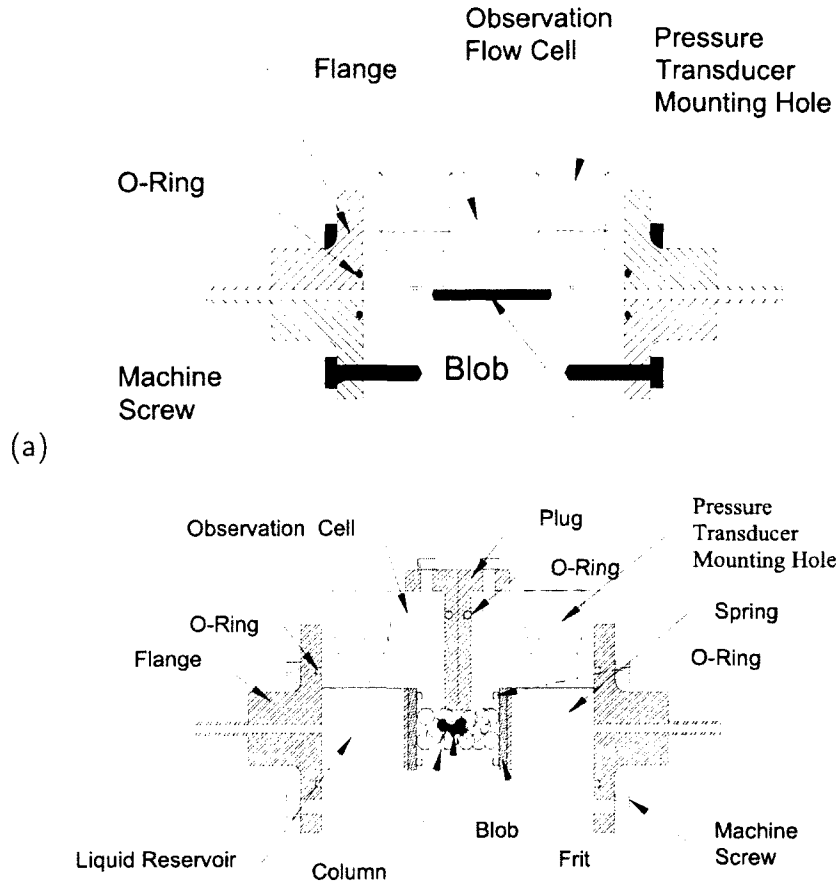

Figure 3.5: Technical drawings of (a) "Cell T" and (b) "Cell S".

3.3.2 Liquids, fluorescent dye and imaging system

For PLIF experiments, we used the two immiscible liquids *5095* and *OHZB* (Cargille Laboratories) as the wetting and non-wetting liquids, respectively. The properties of the liquids are shown in **Table 3.1**, including density, viscosity, and interfacial tension. The interfacial tension was measured by the sessile drop method [6].

Both liquids possess the refractive index of acrylic (solid phase) which is 1.49. Due

Table 3.1: Liquid phase properties at 25°C.

	Wetting phase liquid *code 5059*	Nonwetting phase liquid *OHZB*
Density ρ (g/cm^3)	0.869	2.055
Viscosity ν (cSt)	15	5
Interfacial tension σ (dyne/cm)	14.79	

to the flat outer surfaces of the flow cell, the entire domain was unobstructed for visual observation. However, the two liquids were visually identical (transparent). To distinguish them from one another, the fluorescent dye *Oxazine 1 perchlorate*, (absorption max. 645 nm, Em 680 nm [40]), was added into *OHZB* at a concentration of 0.2 mg/ml. We illuminated the fluorescent blobs in Cell T and Cell S by laser light sheets (Melles Griot^{TM} 75-mW He-Ne laser with 632 nm wavelength). Sample cross-sectional images of menisci/blobs in Cell T and Cell S are shown in **Figure 3.6**.

The dynamic response of the fluorescent blobs to oscillatory flow was imaged with a PC-controlled high-speed CMOS digital camera (Basler 504Kc) which can take images at 500 frames/sec at a full spatial resolution of 1280×1024 pixels. The shapes of the fluorescent blobs in the recorded 2D cross-sectional images were precisely delineated by edge detection tools (Matlab^{TM}).

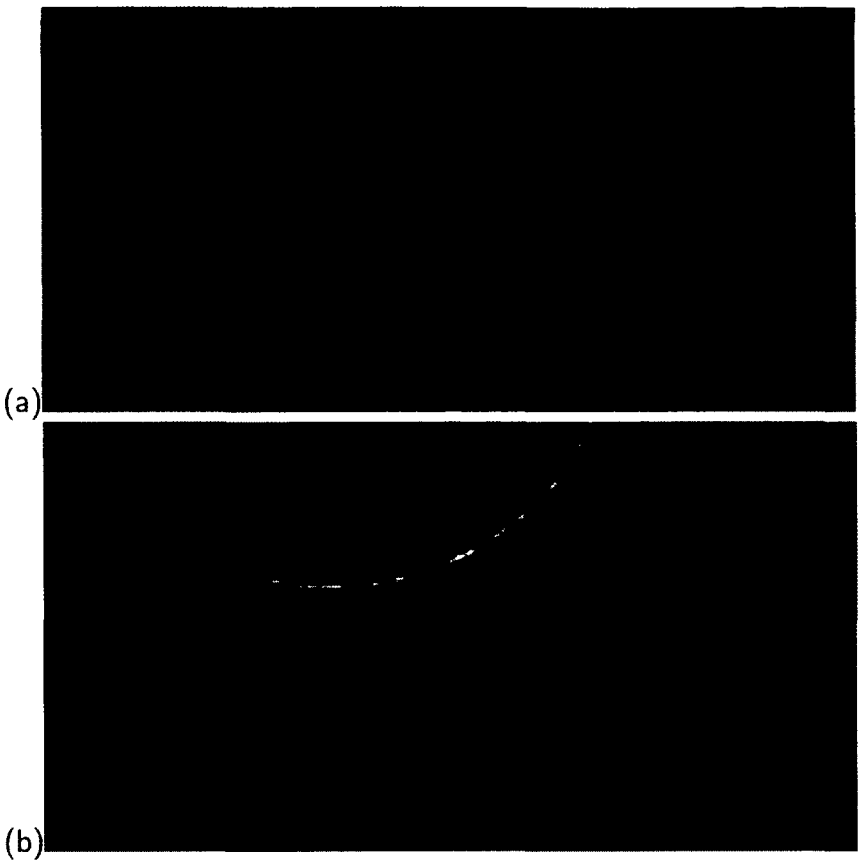

Figure 3.6: (a) A meniscus of a liquid blob in Cell T. (b) A fluorescent blob in Cell S.

3.3.3 Oscillatory flow generation and liquid pressure measurement

The piston of a syringe, which was firmly connected to the PC-controlled actuator, created oscillatory flows of variable frequency and amplitude of the liquid in the syringe. The dynamic pressure difference across the wetting liquid surrounding a blob was measured with two PCB^{TM} $106B$ piezo-electric pressure transducers (**Figure 3.5**). In Cell T, we measured the wetting liquid pressure on both ends of the tube. In Cell S, in which a blob has more than two menisci, we measured the liquid pressure on both sides of the entire

porous medium.

3.3.4 Experimental procedure and measurements

The frequency responses of liquid blobs in the two flow cells were determined by measuring both the amplitude of the meniscus movement in the imaged cross-section and the pressure difference as a function of frequency. Our experiment involved the following steps: (1) the tubes and flow cell were cleaned with deionized water and carefully dried; (2) after filling the flow cell with one liquid, we injected a fluorescent blob into the porous medium; (3) we gave the blob 2 to 3 hours of time to reach equilibrium; (4) the blob was illuminated by a laser light sheet. We used the actuator to generate oscillatory flow at a low frequency and gradually increased the oscillation amplitude by adjusting the input voltage amplitude of the amplifier until a measurable blob response was achieved; (5) we simultaneously imaged one meniscus at 200 frames per second and recorded pressure data at 600 Hz; (6) we kept the input voltage amplitude constant but increased the excitation frequency; (7) we repeated steps (4) to (6) until the excitation frequency reached a chosen a priori maximum value; (8) finally, we analyzed the images to determine contact angles and meniscus displacement; we also determined the pressure difference and then calculated the frequency response of the blob to the imposed oscillatory flows using Eq. (3.11).

3.4 Experimental results and analysis

We were not able to identify the exact meniscus locations of an air blob in the proximity of the three-phase contact lines because of the relatively low image quality due to the incomplete index matching. However, we were still able to identify the majority of the menisci and hence $\overline{z}_{mp}(\omega)$ of the blob. Along with the measured $P_w(\omega)$ data and the measured blob length $L_n = 0.5$ cm and $L_w = 2.5$ cm, we were able to determine the absolute value of the nondimensional frequency response $|\chi|$ of the air blob from Eq. (3.11), where we used $\rho_n = 1.2$ kg/m^3 for the density of air, $\eta_n = 18.27 \times 10^{-6}$ Pa s for the viscosity of air, $\rho_w = 1000$ kg/m^3 for the density of water, and $\eta_w = 1.00 \times 10^{-3}$ Pa s for the viscosity of water (blue circles in **Figure 3.7**.) Resonance occurred at about 14 Hz.

3.4.1 Air-blob in the Cell T

With the measured equilibrium contact angle ($\theta_0 = 25°$) and surface tension of water $\sigma = 72 \times 10^{-3}$ N/m , we were able to calculate ω_{cn}, ω_{cw}, and ω_0 from Eqs. (3.4), (3.6), and (3.10) (**Table 3.2**). By substituting ω_{cn}, ω_{cw}, and ω_0 into Eq. (3.9), we predicted the frequency response shown as a dashed blue line in **Figure 3.7** based on our simple pore model. The predicted resonant frequency is close to the measured one, but the amplitude of the predicted and measured resonance peaks differ significantly. We attribute this deviation to the depinning and sliding of the contact lines. Ideally, when the contact lines are pinned, a change in meniscus shape goes along with a change in

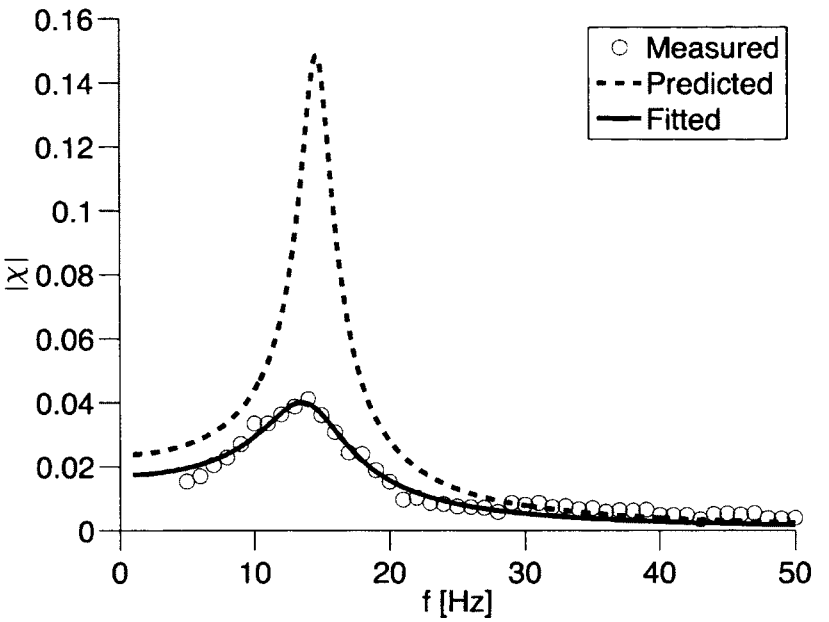

Figure 3.7: The predicted, measured, and fitted absolute value of the nondimensional frequency response χ of the air blob.

contact angle. The recorded images suggest, however, that the menisci were moving with no change in shape when the contact angles were larger or smaller than certain values. Even though the images did not allow us to observe contact line movement, we suspect that during an excitation cycle contact lines depinned and then started sliding, because we observed phases during which a meniscus moved while not changing its shape. The critical values of the contact angles at which depinning occurs are the advancing/receding equilibrium contact angles. The depinning and subsequent sliding of the contact lines leads to nonlinear meniscus movement not captured by our model. Specifically, when depinning happens the relation between changes in $\overline{z}_{sp}$ and θ in Eq. (3.8) is violated. Moreover, depinning/sliding leads to additional damping not captured in our model [9]. Dimon et al. [14] and Hilpert and Miller [19] suspected similar behavior in their experiments which also

examined resonance of menisci.

Our theory neglects the effect of gravity on the shape of the menisci and the compressibility of the air blob. Here we examine the validity of these assumptions. The small ratio of the hydrostatic pressure across the interface to a typical capillary pressure, $\Delta P_g/|P_c| \approx 0.15$, shows that gravity does not significantly affect interfacial shape due to the strong interfacial tension. The pressure in the blob will be relatively uniform as long as the wave length is much larger than the length of the blob. For the blob lengths used in our experiments, this condition was fulfilled when $f \ll 500$ Hz. Since our excitation frequency ranged from 5 to 40 Hz, the air pressure inside the blob can indeed be treated as spatially uniform. However, the air inside the blob might not be treated as incompressible which is assumed in our model. Chen and Prosperetti [10] showed that, even in small tubes, thermal damping can dominate viscous damping for a compressible oscillating gas (air) bubble. Therefore, the difference between our prediction and measured data might also be due to the compressibility of the air and the thermal damping which is not considered in our model. Our model should be improved by taking compressibility and Chen and Prosperetti [10]'s theory into account. However, most contaminants are in the form of liquid blobs which are almost incompressible. Therefore, a comprehensive model for both compressible and incompressible gas/liquid blobs will be addressed in future work.

Eventually, we fitted our model to the measured data by using ω_{cn}, ω_{cw}, and ω_0 as fitting parameters. The values of fitted parameters are shown in **Table 3.2**. The largest difference between the measured and fitted parameters stems from the parameter that

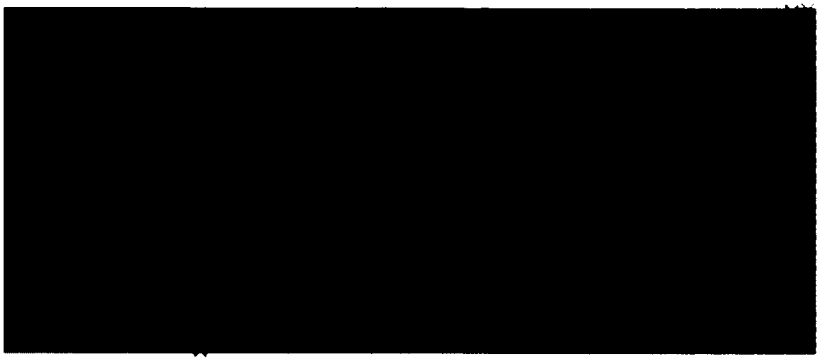

Figure 3.8: A sample image of a meniscus of a liquid blob in Cell T. Red crosses indicate the location of the meniscus. The fitted line is shown in blue.

represents friction, ω_{cw}. This discrepancy agrees with our speculation that the additional damping due to the depinning/sliding of the menisci might contribute the most to the difference between our theoretical prediction and measured data.

3.4.2 Index-matched liquid blob in the Cell T

By exploiting the PLIF technique, we could obtain cross-sectional images of a blob that are free from optical distortions as shown in **Figure 3.6a**. Once the laser light sheet was adjusted to pass through the tube axis, we were able to image the meridian profile of the meniscus/blob. We fitted polynomial functions to the median profiles. Fitted curves were carefully compared to the original images to ensure that images were segmented correctly **(Figure 3.8)**. From the polynomial curves used to represent the fluid-fluid interfaces and the segmentation of the straight tube walls, we were not only able to determine $\overline{z}_{mp}$, but also the contact angles of the meridian profiles [2, 22].

We determined the absolute value of χ shown as blue circles in **Figure 3.9a** according

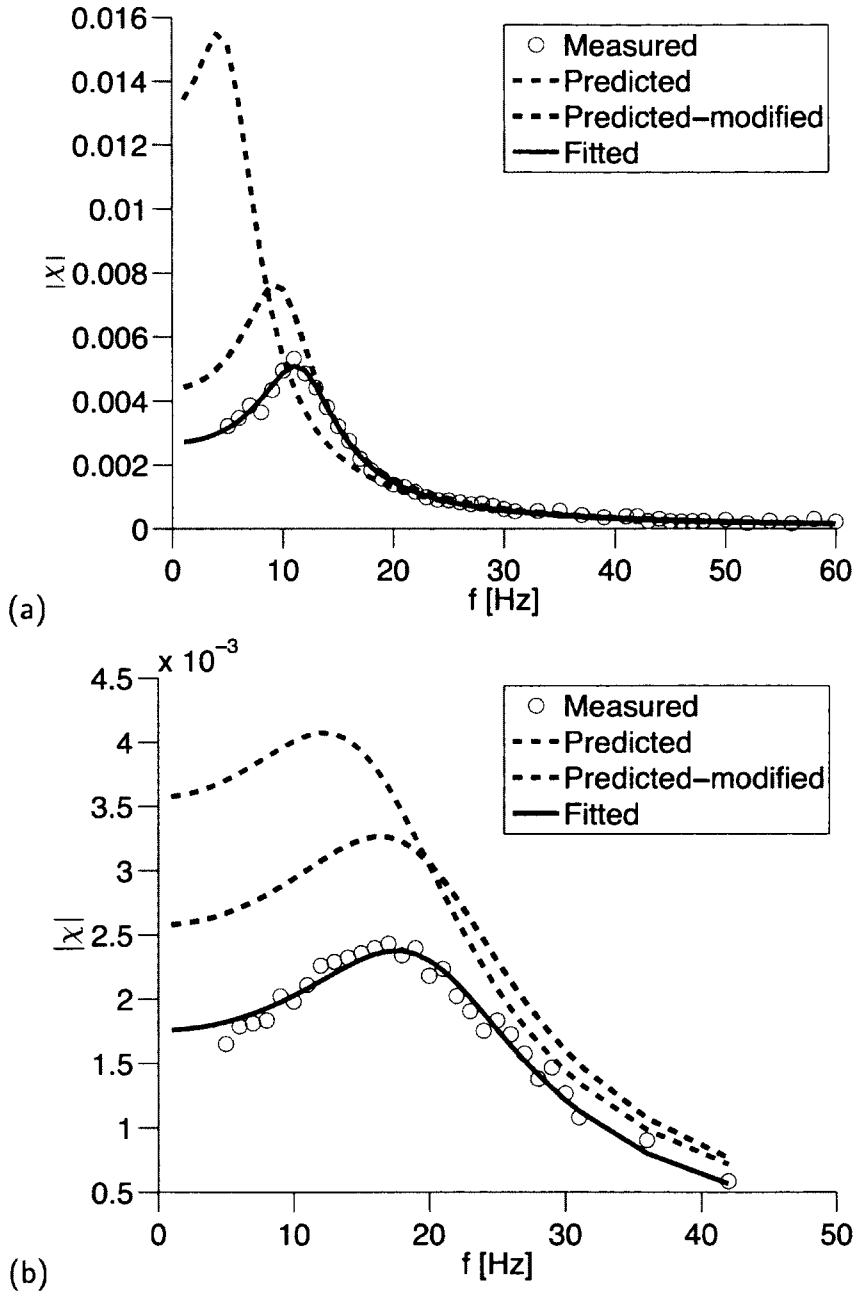

Figure 3.9: Absolute value of nondimensional frequency response χ of a blob in porous media: (a) a capillary tube (b) a sphere packing. Circles: measured data. Solid lines: fitted curves. Blue dashed lines: original theoretical prediction. Black dashed lines: modified theoretical prediction.

to Eq. (3.11) from the measured $\overline{z}_{mp}(\omega)$ and $P_w(\omega)$ data and the measured blob length $L_n = 0.62$ cm. Resonance occured at about 11 Hz. We predicted the theoretical $|\chi|$ from Eq. (3.9) and the calculated value of ω_{cn}, ω_{cw}, and ω_0 which are determined from Eqs. (3.4), (3.6), and (3.10) and listed in **Table 3.2**. Since the contact angles were not uniform on the distorted menisci, we used the average of top and bottom equilibrium contact angles measured from the meridian profile, $\theta_0 = 140°$, in Eq. (3.10). As shown in **Figure 3.9a**, both the measured and the predicted $|\chi|$ clearly show a resonant peak, but the predicted resonant frequency is lower than the measured one.

We suspected that the difference between the measured and predicted $|\chi|$ was due to the effects that gravity had on the shape of the menisci. **Figure 3.6a** shows that the two contact angles (top and bottom) are not equal and that the meniscus does not possess the shape of a spherical cap. Since $\Delta P_g/|P_c| \approx 2.2$, gravity is apparently not negligible and distorts the profile of the meniscus. It would have been good to reduce the effects of gravity by choosing two liquids with a higher interfacial tension and a lower density difference, or a capillary tube with smaller diameter. Since only few pairs of immiscible liquids have the same refractive index as acrylic, we could not avoid the high density difference. The resolution of our high-speed camera also posed a limitation. In order to obtain high-resolution images, we chose a tube with a relatively large diameter of 2 mm. This large diameter allowed gravity to affect the blob shape.

Some of the assumptions in the model from Section 2 were violated due to the action of gravity. Specifically, contact angles were not uniform, and the menisci were not spherical

caps. We therefore generalized our theory to account for gravity. We found that the $d\overline{z}_{sp}/d\theta$ in Eq. (3.8) is affected most. To examine Eq. (3.8), one should analyze measured changes in contact angle, $\Delta\theta$, against the measured displacement $\overline{z}_{sp}$. Since we could not measure $\overline{z}_{sp}$ directly, we expressed $d\overline{z}_{sp}/d\theta$ in terms of $d\overline{z}_{mp}$ and $d\theta$:

$$\frac{d\overline{z}_{sp}}{d\theta} = \frac{d\overline{z}_{sp}}{d\overline{z}_{mp}} \frac{d\overline{z}_{mp}}{d\theta} \tag{3.16}$$

where, from Eqs. (3.8) and (3.12),

$$\frac{d\overline{z}_{mp}}{d\theta} = \frac{R_t}{2}\left(2 - \frac{\pi - 2\theta - \sin(2\theta)}{2}\frac{\sin(2\theta)}{\cos^4(4\theta)}\right) \tag{3.17}$$

Although the governing equation of the shape of a meniscus under the effect of gravity is mathematically described by a non-linear ODE [17, 22], **Figure 3.10** shows that the measured relationship between $\Delta\theta$ and $\overline{z}_{mp}$ is still linear but not predicted well by Eq. (3.17) which assumes the meniscus shape of a spherical cap. Therefore, for the gravity-distorted meniscus, we added a coefficient α to correct Eq. (3.17) and determined it by linear regression. **Figure 3.10** shows the fitted line with estimated value of α. In the modified model, Eq. (3.8) becomes,

$$\frac{d\overline{z}_{sp}}{d\theta} = -\alpha\frac{R_t}{(1+\sin\theta)^2} \tag{3.18}$$

and Eq. (3.10) becomes

$$\omega_0 = \sqrt{\frac{4\sigma}{(L_n\rho_n + L_w\rho_w)R_t^2}\alpha\left[\sin\theta_0(1+\sin\theta_0)^2\right]} \tag{3.19}$$

Figure 3.9a shows that the modified theory, which uses the resonant frequency according to Eq. (3.19) with $\alpha = 3.01$, yields much better predictions than the theory which uses Eq. (3.10). The $dP_c/d\theta$ might also be affected by gravity, but Hsu et al. [22] showed that $P_c = 2\sigma\cos\theta/R_t$ is still approximately valid for a gravity-distorted meniscus if the average of top and bottom contact angles is used for θ_0.

The difference between the prediction of our modified model and the measured data decreases but is still noticeable. We believe that the modified Eq. (3.17) (with α) can be improved by using a nonlinear form with additional parameters to better describe the relationship between $\overline{z}_{mp}$ and $\Delta\theta$, but this generalization was beyond the scope of this paper. Contrary to the air-water experiments, we did not detect any depinning/sliding of the meniscus at contact points on the meridian profile (even though other portions of the contact line might have slid). However, our theory neglects the viscous pressure drops due to the the complex flow in the vicinity of the meniscus.

With fitting parameters ω_{cn}, ω_{cw}, and ω_0, **Figure 3.9a** also shows the best fit of the measured points with our theory Eq. (3.9). The values of the fitted parameters are shown in **Table 3.2**. By introducing α to correct the effects of gravity, the modified theoretical ω_0 according to Eq. (3.19) is much closer to the fitted ω_0 than the original theoretical ω_0.

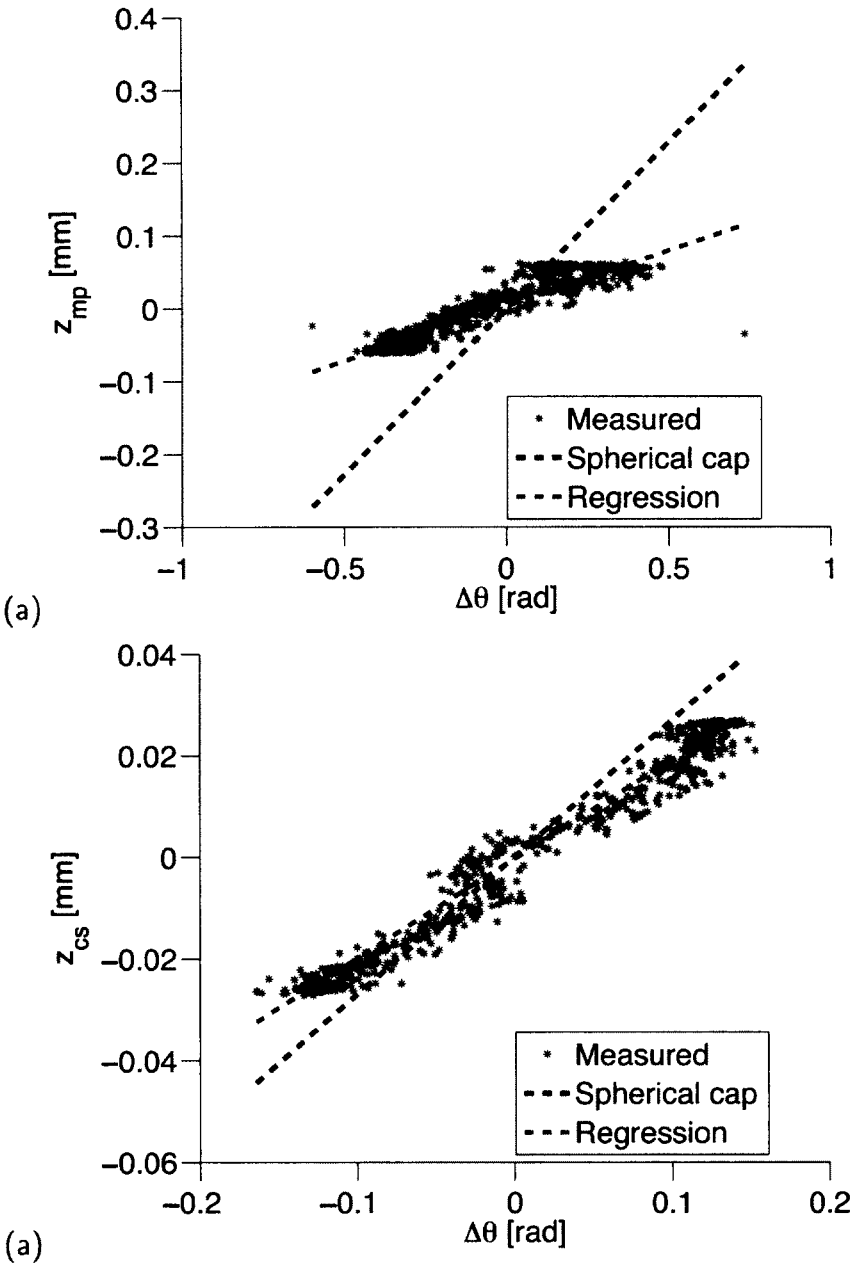

Figure 3.10: $\overline{z}_{mp}$ versus θ in (a) Cell T and (b) Cell S: stars are measured data; black dashed lines aew predictions based on the spherical cap assumption and Eq. (3.17); red dashed lines stem from the linear regression.

Hence, the difference between the theoretical and fitted ω_0 is mainly due to the effect of gravity on the shape of the menisci.

Table 3.2: Comparison of measured and fitted values for ω_{cw}, ω_{cn} ,and ω_0

		Analytical model				Fitted response		
Cell	Fluids	ω_{cn} (s^{-1})	ω_{cw} (s^{-1})	ω_0 (s^{-1})	ω_0 (α) (s^{-1})	ω_{cn} (s^{-1})	ω_{cw} (s^{-1})	ω_0 (s^{-1})
Cell T	Air-water	15.2	1.0	99.3		14.6 ± 0.8	5.6 ± 1.1	103.2 ± 2.9
	5095-OHZB	5.0	15.0	43.5	75.4	5.7 ± 0.1	12.7 ± 3.1	88.4 ± 1.0
Cell S	*5095-OHZB*	7.8	23.4	130.8	142.5	8.8 ± 0.3	21.4 ± 2.1	157.9 ± 4.0

3.4.3 Index-matched liquid blob in the Cell S

As for the liquid blob in Cell T, we used the PLIF technique to visualize the menisci of the blob in Cell S. Contrary to a blob in a tube, in a sphere packing the shape of the menisci is far from a spherical cap. Moreover, the number of the menisci is not limited to two, and the meridian profile might not be well-defined. The cross-section in the blob with the largest displacement was picked as the imaging target in order to facilitate image analysis and increase image resolution.

Figure 3.6b shows an image of the cross-section of the fluorescent blob in Cell S that yielded the largest displacement with an amplitude $\overline{z}_{cs}$. Since the selected "cross-section" here is no longer a meridian profile of the blob, we use the subscript cs, instead of mp. $L_n = 0.3$ cm is defined as the length of the blob in the selected cross-section in **Figure 3.6b**. $R_t = 0.8$ cm is the radius of the pore throat which is also measured from **Figure 3.6b**. From the measured $\overline{z}_{cs}$ and $P_w(\omega)$ data, we determined, based on Eq. (3.11),

the measured frequency responseq $|\chi|$, which is shown as blue circles in **Figure 3.9b**. Obviously the blob exhibited resonance.

Figure 3.6b shows that the contact angles (top and bottom) on the menisci are not equal, and the shape of the menisci are non-spherical. Gravity distorted the profile of the meniscus because $\Delta P_g/|P_c| \approx 2.8$. As in Sec. 3.4.2, we corrected for the effects of gravity by plotting measured $\overline{z}_{cs}$ and $\Delta\theta$ data and determining the coefficient $\alpha = 1.39$. By taking the average contact angle of top and bottom contact angles as the representive contact angle, $\theta_0 = 100.3°$, the frequency responses predicted by our model according to Eq. (3.9) with and without α are shown in **Figure 3.9b**. Adding α to our model improves the predicted $|\chi|$ curve and in particular the predicted resonant frequency.

The major reasons for the difference between predicted and measured $|\chi|$ are the geometry of the model and the location of the pressure measurement. The geometry of our model is based on a capillary tube, but in Cell S the blob was trapped among packed spheres. The number of menisci was also larger than two. Also, the blob is usually not symmetric. Thus, an imaged cross-section is usually not a meridian profile. Moreover, contact angles determined from 2D images are not always equal to the real 3D ones. To image the whole blob oscillation in 3D would help explain the difference between our modeling and the measured result, but unfortunately 3D visualization techniques are currently limited to measuring the blob in stasis or moving at an extremely slow pace. Despite the model shortcomings, it still provides a rough and actually better than-order-of-magnitude estimate of blob resonance in a sphere packing.

3.5 Summary

We formulated a simple 1D model pore system to describe the response of a blob in a capillary tube to an oscillatory external pressure difference. This model theoretically predicts the resonance of the blob. We concluded that the occurance of resonance depends on the density and viscosity of two liquids, interfacial tension, contact angle, and the radius of the tube.

Our PLIF experiments confirm our prediction that a blob in a horizontally oriented capillary tube resonates. This is consistent with experiments by Bian et al. [5], even though in some of our experiments the menisci were distorted by gravity. In addition, we showed that an air blob surrounded by water exhibits resonance. This result could be useful for natural gas detection/extraction in porous media by seismic waves.

We demonstrated the ability of the PLIF technique to visualize the dynamic response of menisci in porous media to oscillatory flow. Moreover, the measured profiles of the dynamic menisci were used to determine an additional coefficient for incorporating the effects of gravity on the shape of menisci into our theory. By doing that, we significantly reduced the difference between the prediction of our simple 1D model and the measured data.

Furthermore, the frequency response of a liquid blob in a sphere packing to oscillatory flows was measured for the first time. The results showed that a blob may exhibit resonance. Although the geometries of the measured blob and our 1D pore model have significant differences, the predicted resonant frequency is in fair agreement with the

measured one.

A fully analytical solution of the frequency response of a blob in a sphere packing or a sand packing has not yet been derived. Computational fluid dynamic techniques, for example those based on the lattice-Boltzmann method [18], could be used to predict the frequency response of blobs; however, such simulations require significant amounts of CPU time. In contrast, our 1D pore model provides a simple means of predicting the occurrence of resonance of blobs in porous media and arriving at rough estimates of the frequency response.

3.6 Acknowledgments

This work was supported by NSF Grant EAR-0739038.

Bibliography

[1] P. E. Arratia and F. J. Muzzio. Planar laser-induced fluorescence method for analysis of mixing in laminar flows. *Industrial & Engineering Chemistry Research*, 43(20): 6557–6568, 2004.

[2] A. Bateni, S. S. Susnar, A. Amirfazli, and A. W. Neumann. A high-accuracy polynomial fitting approach to determine contact angles. *Colloids and Surfaces A: Physicochemical and Engineering Aspects*, 219:215–231, 2003.

[3] I. A. Beresnev and A. P. Johnson. Elastic-wave stimulation of oil production: A review of methods and results. *Geophysics*, 59(6):1000–1017, 1994.

[4] I. A. Beresnev, A. Gaul, and R. D. Vigil. Direct pore-level observation of permeability increase in two-phase flow by shaking. *Geophysical Research Letters*, 38:L20302, 2011. doi: 10.1029/2011GL048840.

[5] X. Bian, M. Perlin, W. W. Schultz, and M. Agarwal. Axisymmetric slosh frequencies of a liquid mass in a circular cylinder. *Physics of Fluids*, 15:3659–3664, 2003.

[6] J. J. Bikerman. *Physical surfaces*. Academic Press, New York, 1970.

[7] M. A. Biot. Theory of propagation of elastic waves in a fluid-saturated solid, II.

Higher-frequency range. *Journal of the Acoustical Society of America*, 28:179–191, 1956.

[8] M. K. Broadhead. Oscillating oil drops, resonant frequencies, and low-frequency passive seismology. *Geophysics*, 75(1):1–7, 2010.

[9] E. Charlaix and H. Gayvallet. Dynamics of a harmonically driven fluid interface in a capillary. *Journal de Physique II*, 2(11):2025–2038, 1992.

[10] X. M. Chen and A. Prosperetti. Thermal processes in the oscillation of gas bubble in tubes. *Journal of Acoustical Society of America*, 104:1389–1398, 1998.

[11] C. V. Chrysikopoulos and E. T. Vogler. Acoustically enhanced ganglia dissolution and mobilization in a monolayer of glass beads. *Transport in Porous Media*, 64(1): 103–121, 2006.

[12] J. P. Crimaldi and J. R. Koseff. High-resolution measurements of the spatial and temporal scalar structure of a turbulent plume. *Experiments in Fluids*, 31(1):90–102, 2001.

[13] C. Dewey. Qualitative and quantitative flow field visualization utilizing laser-induced fluorescence. *In: Proceedings of the AGARD conference of non-intrusive instrumentation in fluid flow research, AGARD-CP-193*, 1976.

[14] P. Dimon, A. P. Kushnick, and J. P. Stokes. Resonance of a liquid-liquid interface. *Journal de Physique*, 49(5):777–785, 1988.

[15] P. E. Dimotakis, R. C. Miakelye, and D. A. Papantoniou. Structure and dynamics of round turbulent jets. *Physics of Fluids*, 26(11):3185–3192, 1983.

[16] M. M. Fontenot and R. D. Vigil. Pore-scale study of nonaqueous phase liquid dissolution in porous media using laser-induced fluorescence. *Journal of Colloid and Interface Science*, 247:481–489, 2002.

[17] Y. Gu and C. Yang. The effects of capillary force and gravity on the interfacial profile in a reservoir fracture or pore. *Journal of Petroleum Science & Engineering*, 40(1-2): 77–87, 2003.

[18] M. Hilpert. Capillarity-induced resonance of blobs in capillary porous media: analytical solutions, lattice-Boltzmann modeling, and blob mobilization. *Journal of Colloid and Interface Science*, 309:493–504, 2007.

[19] M. Hilpert and C. T. Miller. Experimental investigation on the resonance of a liquid column in a capillary tube. *Journal of Colloid and Interface Science*, 219(1):62–68, 1999.

[20] M. Hilpert, G. H. Jirka, and E. J. Plate. Capillarity-induced resonance of oil blobs in capillary tubes and porous media. *Geophysics*, 65:874–883, 2000.

[21] R. Holzner, P. Eschle, S. Dangel, M. Frehner, C. Narayanan, and D. Lakehal. Hydrocarbon microtremors interpreted as nonlinear oscillations driven by oceanic back-

ground waves. *Communications in Nonlinear Science and Numerical Simulation*, 14: 160–173, 2009.

[22] S. Y. Hsu, R. Glantz, and M. Hilpert. Pore-scale analysis of the effects of contact angle hysteresis on blob mobilization in a pore doublet. *International Journal of Oil, Gas and Coal Technology*, in-press, 2012.

[23] W. Li, D. V. Vigil, I. A. Beresnev, P. Iassonov, and R. Ewing. Vibration-induced mobilization of trapped oil ganglia in porous media: experimental validation of a capillary-physics mechanism. *Journal of Colloid and Interface Science*, 289:193–199, 2005.

[24] H. T. Liu, J. T. Lin, D. P. Delisi, and F. A. Robben. Application of a fluorescence technique to dye-concentration measurements in a turbulent jet. *In: Proceedings of the symposium on flow measurement in open channels and closed conduits. NBS Special Publication*, 484:423–446, 1977.

[25] R. Matsumoto, H. F. Zadeh, and P. Ehrhard. Quantitative measurement of depth-averaged concentration fields in microchannels by means of a fluorescence intensity method. *Experiments in Fluids*, 39(4):722–729, 2005.

[26] A. S. Mayer and C. T. Miller. The influence of porous medium characteristics and measurement scale on pore-scale distributions of residual nonaqueous-phase liquids. *Journal of Contaminant Hydrology*, 11(3/4):189–213, 1992.

[27] C. D. Montemagno and W. G. Gray. Photoluminescent volumetric imaging –A technique for the exploration of multiphase flow and transport in porous media. *Geophysical Research Letters*, 22(4):425–428, 1995.

[28] K. M. Ng, H. T. Davis, and L. E. Scriven. Visualization of blob mechanics in flow through porous media. *Chemical Engineering Science*, 33(8):1009–1017, 1978.

[29] P. K. Niven and K. Singh. Mobilization and rupture of LNAPL ganglia during freeze-thaw: two-dimensional cell experiments. *Environmental Science & Technology*, 42: 5467–5471, 2008.

[30] R. Onishi and S. Komori. Thermally stratified liquid turbulence with a chemical reaction. *AIChE Journal*, 52(2):456–468, 2006.

[31] H. Ovdat and B. Berkowitz. Pore-scale study of drainage displacement under combined capillary and gravity effects in index-matched porous media. *Water Resources Research*, 42:W06411, 2006. doi: 10.1029/2005WR004553.

[32] F. Owen. Simultaneous laser measurement of instantaneous velocity and concentrations in turbulent mixing flows. *In: Proceedings of the AGARD conference of non-intrusive instrumentation in fluid flow research, AGARD-CP-193*, 1976.

[33] G. Pan and H. Meng. Experimental study of turbulent mixing in a tee mixer using PIV and PLIF. *AIChE Journal*, 47(12):2653–2665, 2001.

[34] A. C. Payatakes. Dynamics of oil ganglia during immiscible displacement in water-wet

porous media. *Annual Review Fluid Mechanics*, 14:365–393, 1982. doi: 10.1146/annurev.fl.14.010182.002053.

[35] M. Rashidi, L. Peurrung, A. F. B. Tompson, and T. J. Kulp. Experimental analysis of pore-scale flow and transport in porous media. *Advances in Water Resources*, 19 (3):163–180, 1996.

[36] L. N. Reddi. Feasibility of in situ implementation of vibrations to mobilize NAPL ganglia. *Journal of Soil Contamination*, 3(1):29–46, 1994.

[37] L. N. Reddi and S. Challa. Vibratory mobilization of immiscible liquid ganglia in sands. *Journal of Environmental Engineering ASCE*, 120(5):1170–1190, 1994.

[38] P. M. Roberts, A. Sharma, V. Uddameri, M. Monagle, D. E. Dale, and L. K. Steck. Enhanced DNAPL transport in a sand core during dynamic stress stimulation. *Environmental Science & Technology*, 18(2):67–69, 2001.

[39] W. Rose and R. W. Heins. Moving interfaces and contact angle rate-dependency. *Journal of Colloid Science*, 17(1):39–48, 1962.

[40] F. W. D. Rost. *Fluorescence microscopy*. Cambridge University Press, New York, 1992.

[41] M. R. Sasges and C. A. Ward. Effect of gravity on contact angle: An experimental investigation. *Journal of Chemical Physics*, 109(9):3661–3670, 1998. doi: 10.1063/1.476962.

[42] K. Shiono and T. Feng. Turbulence measurements of dye concentration and effects of secondary flow on distribution in open channel flows. *Journal of Hydraulic Engineering ASCE*, 129(5):373–384, 2003. doi: 10.1061/(ASCE)0733-9429(2003)129:5(373).

[43] M. Stöhr, K. Roth, and B. Jähne. Measurement of 3D pore-scale flow in index-matched porous media. *Experiments in Fluids*, 35:159–166, 2003.

[44] C. D. Troy and J. R. Koseff. The instability and breaking of long internal waves. *Journal of Fluid Mechanics*, 543:107–136, 2005.

[45] D. R. Webster, S. Rahman, and L. P. Dasi. Laser-induced fluorescence measurements of a turbulent plume. *Journal of Engineering Mechanics ASCE*, 129(10):1130–1137, 2003.

Chapter 4. Incorporation of Dynamic Capillary Pressure into the Green-Ampt Model for Infiltration

Abstract

The Green-Ampt model describes infiltration of water into soil. A sharp front separates the saturated from the unsaturated zone, and capillary pressure is assumed to remain constant during infiltration. We generalize this model to account for a capillary pressure that depends on the flow velocity. Based on dimensional analysis and physical considerations, we posit a functional form for dynamic capillary pressure and assume the nonequilibrium capillary pressure to depend on the capillary number in the form of a power law. Our model for dynamic capillary pressure describes measurements of capillary pressure versus Darcy velocity by Weitz et al. (PRL 1987) and Geiger and Durnford (SSSAJ 2000). Moreover, the dimensional analysis allows us to collapse three dynamic capillary pressure curves that Geiger and Durnford measured for sands of different grain size onto one curve. Furthermore our model describes capillary rise experiments performed by Tabuchi well (Rec. Land Reclam. Res. 1971). The final stages of these experiments, during which the fronts approached the equilibrium water table, cannot be described by the classical

Green-Ampt model. We also derive an implicit analytical solution for the front velocity.

Abbreviations: GA, Green-Ampt

4.1 Introduction

Infiltration of a liquid into soil is an important vadose zone process. It occurs when rain water infiltrates into dry soil, when a liquid contaminant is spilled onto the ground, or when underground pipes and storage tanks leak liquids into soil. The Green-Ampt (GA) model (1911) for water infiltration into porous media assumes a sharp moving interface between the water-saturated porous medium with a uniform satiated water content θ_s behind the interface and the unsaturated porous medium with a uniform initial water content θ_i in front of the interface. In the remainder of the paper, we will refer to this interface as the wetting front or simply the front. Furthermore, the following assumptions are made in the GA approach: (1) Flow in the water-saturated zone behind the advancing front is governed by Darcy's law; (2) The soil air pressure, p_a, ahead of the front is uniform (due to the low viscosity of air) and constant; (3) There is a boundary condition for hydraulic head, h_0, which typically does not depend on time and which, for downward infiltration, could be caused by ponding of water; and (4) The hydraulic pressure head h_p at the front is constant. In this paper, we will let fall this assumption since we will assume capillary pressure p_c to depend on the front velocity.

Let us formally present the GA approach, because we will generalize it with regard to Item 4 in the above list. Our coordinate system is defined such that for both downward and upward infiltration (capillary rise), the distance l between the front and the hydraulic head boundary condition is positive, $l \geq 0$. Therefore the Darcy velocity q and the front velocity $\dot{l}$ are positive for both downward and upward infiltration, that is, $q > 0$ and $\dot{l} > 0$.

Figure 4.1 illustrates these two infiltration scenarios. Darcy's law describes flow behind the front:

$$q = -K\frac{h(l) - h_0}{l} \tag{4.1}$$

where K is the hydraulic conductivity at satiation, and $h(l)$ is the hydraulic head at the front. The latter can be decomposed into a pressure and an elevation head:

$$h(l) = \begin{cases} h_p(l) + l & \text{for upward infiltration} \\ h_p(l) - l & \text{for downward infiltration} \end{cases} \tag{4.2}$$

where we place the datum at the inlet of the column. Likewise we can decompose the hydraulic head boundary condition. Assuming that it is due to ponding of water, the hydraulic head boundary condition becomes

$$h_0 = \frac{p_a}{\rho g} + H_0 \tag{4.3}$$

where H_0 is the ponding depth. Since the water content increases from θ_i to θ_s as the front passes through, one can relate the front velocity to the Darcy velocity:

$$q = (\theta_s - \theta_i)\dot{l} \tag{4.4}$$

This consideration assumes that water associated with θ_i is stagnant, both ahead of and behind the front. Substituting Eq. (4.2) into Eq. (4.1) and then equating Eqs. (4.1) and

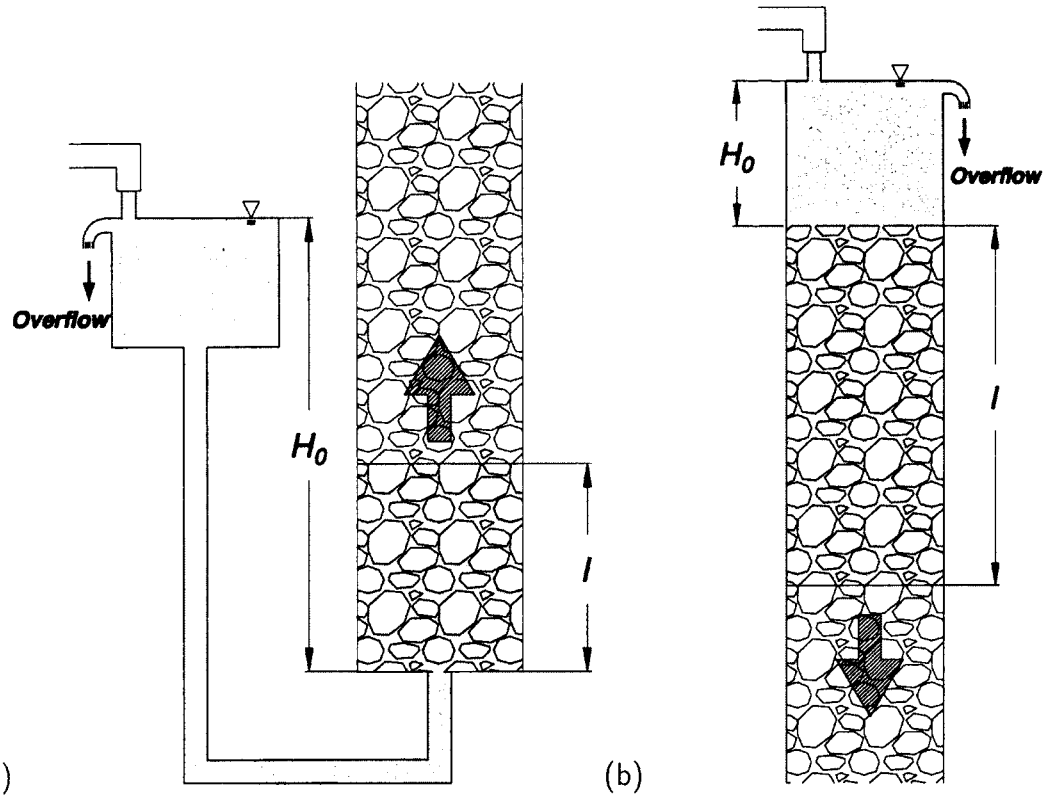

Figure 4.1: Illustration of the GA approach for water infiltration into porous media. (a) Upward infiltration. (b) Downward infiltration.

(4.4) yields an ordinary differential equation for the front position l:

$$\frac{\theta_s - \theta_i}{K} \dot{l} = \begin{cases} \dfrac{h_0 - h_p(l) - l}{l} & \text{for upward infiltration} \\ \\ \dfrac{h_0 - h_p(l) + l}{l} & \text{for downward infiltration} \end{cases} \tag{4.5}$$

The GA approach assumes the pressure head at the front to remain constant during infiltration, $h_p(l) = h_p = \text{const}$. Using the method of separation of variables and subsequent integration, one can obtain the well-known solutions to Eq. (4.5) [10]. For upward infiltration, the front moves from the initial position, $l(t = 0) = 0$, into the

porous medium and asymptotically approaches the equilibrium height of the water table, $H_{eq} = h_0 - h_p$, which can be obtained by setting $\dot{l} = 0$ in Eq. (4.5). For downward infiltration, the front moves from the initial position $l(t = 0) = 0$ at an initially infinite velocity into the soil and then approaches the steady-state velocity $K/(\theta_s - \theta_i)$.

Iwata et al. [18] suggest that deviations between the late stage of infiltration experiments performed by Tabuchi [35] and modeling based on the GA approach could be explained by a contact angle and hence a hydraulic pressure head at the front, $h_p(l)$, which are not constant but depend on flow rate. Tabuchi performed upward infiltration experiments in porous medium columns and plotted $q\,l$ versus l. According to Eq. (4.5), $q\,l$ should scale linearly with l for upward infiltration,

$$q\,l = K(h_0 - h_p - l) \tag{4.6}$$

because h_p is constant. The symbols in **Figure 4.2** show the results of three infiltration experiments performed by Tabuchi. The points in the origin correspond to the beginning of the infiltration experiments when $l = 0$. The points at the very right correspond to the end of the experiments, when l approached H_{eq}. The middle portions of the three curves can be modeled by straight lines. If one does not account for a dynamic pressure head h_p, then the negative slope of such a line should equal the hydraulic conductivity K according to Eq. (4.6). At the final points at the right, however, the slopes of the experimental curves increase significantly (from a negative value to zero), which cannot

be explained by Eq. (4.6). Iwata et al. [18] attribute this anomaly to a contact angle that depends on the flow velocity and that affects the "capillary force."

Liquid-air displacement experiments in capillary tubes have indeed shown that contact angle (and hence p_c) is a function of the velocity of the liquid-air interface [17, 32]. Such experiments are backed up by theoretical studies [1, 2, 21]. Therefore the capillary pressure at the front, $p_c(l) = p_a - p_w(l)$, cannot be expected to be constant during infiltration, where $p_w(l)$ is the water pressure measured directly behind the infiltration front (using a tensiometer) and p_a is measured ahead of the front. Hence, the pressure head at the front, $h_p(l)$, cannot be expected to be constant since it depends on p_c through $h_p(l) = p_w(l)/(\rho g) = [p_a - p_c(l)]/(\rho g)$.

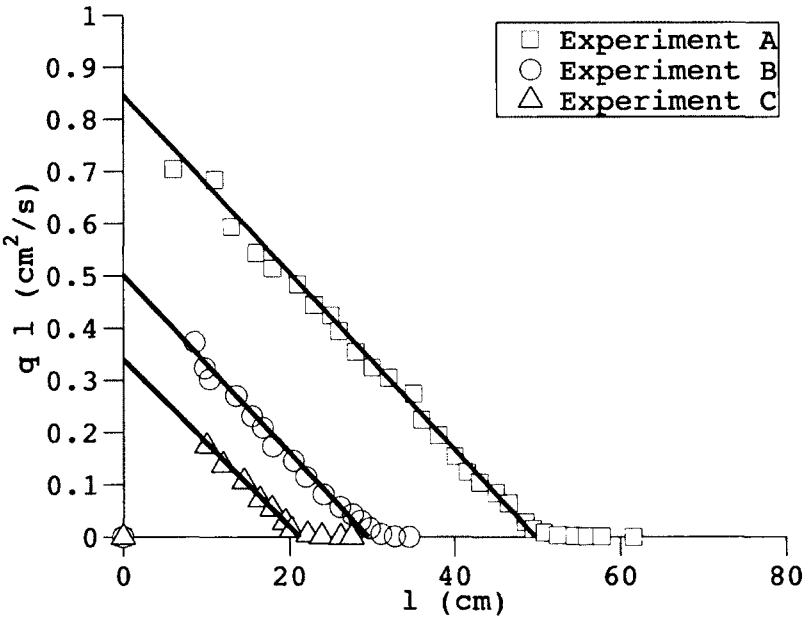

Figure 4.2: Relation between ql and l for three capillary rise experiments performed by Tabuchi [35]. The center portions of the three data sets can be described by straight lines. The data deviate from the straight lines both at the beginning ($l = 0$) and at the end (highest l values) of the infiltration experiments.

Various studies indicate that the capillary pressure p_c at an infiltration front also depends on flow rate at the Darcy scale. Weitz et al. [39] performed column experiments, in which water displaced decane in a glass bead packing at a constant flow rate, and proposed that p_c at the displacement front is velocity dependent according to the following power law:

$$p_c \approx \frac{\sigma}{r_{th}} \left(1 - K\mathrm{Ca}^{\beta}\right) \tag{4.7}$$

where σ is the interfacial tension, r_{th} is a characteristic throat radius, K and β are fit parameters, $\mathrm{Ca} = \eta v/\sigma$ is the capillary number, η is the dynamic viscosity, and v is the interstitial fluid velocity. Downward infiltration experiments by Geiger and Durnford [9], during which the Darcy velocity q was held constant, have also shown that capillary pressure at the infiltration front depends on q. Geiger and Durnford, however, did not attempt to develop a model for capillary pressure as a function of q, nor did they perform a dimensional analysis. Siebold et al. [32] explain differences between capillary rise experiments in powder packings and the Washburn theory for infiltration into a capillary tube by a contact angle that depends on the flow velocity. DiCarlo [5] also observed that the capillary pressure at an infiltrating water front depends on the flow velocity. Although speculating that the constants in Eq. (4.7) should depend on the initial water content θ_i, DiCarlo did not analyze the infiltration data with Eq. (4.7). Weisbrod et al. [38] found that the early stage of upward infiltration can be best described by a GA model that uses a "dynamic" contact angle that is significantly larger than the equilibrium contact angle;

however, this dynamic contact angle was assumed to be constant.

So far, nobody has formulated any generalizations of the GA model which account for a dynamic capillary pressure at the wetting front that depends on the front velocity. In Section 4.2, we will do so and also present a conceptual model for the Darcy-scale dynamic capillary pressure at an infiltration front that is based on dimensional analysis and pore-scale physics. This model will shed light on the nature of r_{th} in Eq. (4.7). Note that we do not seek to generalize the more general Richards theory (1931) for two-phase flow in porous media, because it is not obvious how a capillary pressure which is only defined at an infiltration front can be incorporated into a Eulerian theory in which capillary pressure is defined everywhere. Generally, our new theory requires a numerical solution; however, for the special case where the nonequilibrium capillary pressure depends on the flow velocity through a power law, we can derive semi-analytical solutions. In Section 4.3, we reanalyze the infiltration experiments performed by Geiger and Durnford and infer functional forms for dynamic capillary pressure. In Section 4.4, we show that our new theory describes the late stage of the aforementioned infiltration experiments by Tabuchi better than the classical GA approach. In Section 4.5, we illustrate the pronounced effects of a dynamic capillary pressure on downward and upward infiltration. Finally in Section 4.6, we compare the data on dynamic capillary pressure at an infiltration front that we gathered to one another and explain differences with our conceptual model.

4.2 Theory

4.2.1 Conceptual model for Darcy-scale dynamic capillary pressure

Contrary to the classical GA approach, we do not assume capillary pressure at the wetting front, p_c, to remain constant during infiltration. Instead we assume p_c to depend on the velocity of the wetting front, $\dot{l}$, through a velocity-dependent contact angle ϑ. To arrive at a model for dynamic capillary pressure p_c, we identify physical variables on which p_c could possibly depend. To that end, we first consider pore-network models, which represent a geometrically complex porous medium by means of simply shaped pore bodies connected by simply shaped pore throats. For spherical pore bodies, a capillary pressure at which wetting fluid displaces nonwetting fluid during quasi-static imbibition (e.g., water infiltration into a water-wet porous medium) is frequently assumed to be [20, 16]

$$p_c = \frac{2\sigma}{R}\cos\vartheta \tag{4.8}$$

where R is the pore body radius, and ϑ is the contact angle. Friedman [8], who modeled a flow-rate-dependent capillary pressure-saturation relation, assumed that such a relationship is valid even if ϑ depends on flow rate. The pore spaces that we consider in this work are much more complex than pore networks with spherical pore bodies. In fact, in sand the geometry is often reversed: solid sand grains are often roughly spherical in shape,

while the pore bodies have complicated angular shapes.

For a granular porous medium such as a soil, we thus modify Eq. (4.8) and assume the following dependencies for the Darcy-scale dynamic capillary pressure at the front:

$$p_c = p_c(\text{Geometry}, \theta_i, \sigma, \vartheta) \tag{4.9}$$

where "Geometry" represents variables that quantify pore-body size, either directly in terms of a pore-size distribution, or indirectly in terms of a grain-size distribution and porosity. The contact angle ϑ in Eq. (4.9) is assumed to be a function of the capillary number Ca, $\vartheta = \vartheta(\text{Ca})$ where $\text{Ca} = \eta \dot{l}/\sigma$. Note that one could have also used the Darcy velocity q to define Ca. Microscopic observations, however, suggest that the contact angle depends on the velocity of the air-water interface, $\dot{l}$, and not on q. We also accounted for a dependence on the initial water content θ_i, because infiltration experiments by DiCarlo [5] have shown that the dynamic capillary pressure depends on θ_i, with dynamic effects being more pronounced for small θ_i values. In a porous medium of uniform grain size D, the "Geometry" variables in Eq. (4.9) are D and the porosity ε. Dimensional analysis of Eq. (4.9) then implies that the nondimensional capillary pressure is given by

$$\frac{p_c D}{\sigma} = \mathcal{P}(\varepsilon, \theta_i, \vartheta) \tag{4.10}$$

where $\mathcal{P}$ is a nondimensional function. Inspired by Eq. (4.8), we assume that p_c depends

on contact angle ϑ through the cosine. Hence

$$\frac{p_c D}{\sigma} = \mathcal{E}(\varepsilon, \theta_i) \cos \vartheta \tag{4.11}$$

where $\mathcal{E}$ is a nondimensional function of ε and θ_i.

In order to describe the dependence of dynamic contact angle ϑ on the flow velocity, we assume the nondimensional uncompensated Young force [4] to be a function of Ca:

$$\cos \vartheta_{eq} - \cos \vartheta = \mathcal{F}(\mathrm{Ca}, \cdots) \tag{4.12}$$

where $\mathcal{F}(0) = 0$, and ϑ_{eq} is the advancing equilibrium contact angle. Therefore

$$\frac{p_c D}{\sigma} = \underbrace{\mathcal{E}(\varepsilon, \theta_i) \cos \vartheta_{eq}}_{P_{eq}} \underbrace{- \mathcal{E}(\varepsilon, \theta_i) \mathcal{F}(\mathrm{Ca}, \cdots)}_{P_{neq}} \tag{4.13}$$

where P_{eq} and P_{neq} are the nondimensional equilibrium and nonequilibrium capillary pressures, respectively. Equation (4.12) reflects the fact that a capillary system, which is in non-equilibrium, relaxes to an equilibrium state in the form of a flow process for which $\mathrm{Ca} \neq 0$. Note that even though we motivated Eq. (4.12) based on pore-scale arguments, the contact angle ϑ is like in the imbibition study by Weisbrod et al. [38] an average or effective contact angle.

The dots in Eq. (4.12) represent additional parameters on which $\mathcal{F}$ might depend. Based on Cox's (1986) theory of dynamic contact angle on flat impermeable surfaces that

shows that the contact angle depends slightly (through a logarithm) on the ratio of the slip length to a macroscopic length scale, ϵ, we expect $\mathcal{F}$ to depend on ϵ too. Here the slip length quantifies the surface region around the three-phase contact line (formed by the two fluids and the solid surface) in which the no-slip boundary condition for the fluids is not obeyed. Little is known about the dynamic contact angle of fluid-fluid interfaces in sphere packings. The situation is more complicated than on flat solid surfaces, because contact lines may be destroyed and created when fluid-fluid interfaces jump from one grain to another [24]. A nondimensional pore size R/D could be used to quantify the dimension of the contact line jumps and therefore could be one of the variables that represent the dots in Eq. (4.12).

In this study, we will consider the following power law model for the $\mathcal{F}$ function:

$$\mathcal{F}(\mathrm{Ca}) = \alpha \mathrm{Ca}^{\beta} \tag{4.14}$$

where $\alpha \geq 0$ and $\beta > 0$ are model parameters that are porous medium specific and that are, for example, related to a slip length. The power law model has also been used to describe a dynamic contact angle on impermeable surfaces according to Eq. (4.12) [27, 23, 31]. Equation (4.13) now becomes

$$\frac{p_c D}{\sigma} = \mathcal{E}(\varepsilon, \theta_i) \left[\cos \vartheta_{eq} - \alpha \mathrm{Ca}^{\beta}\right] \tag{4.15}$$

Note that Eq. (4.15) is supported by experiments by Weitz et al. [39] because it conforms

to Eq. (4.7) if $r_{th} = D/[\mathcal{E}(\varepsilon, \theta_i) \cos \vartheta_{eq}]$ and $\mathcal{E}(\varepsilon, \theta_i)\, \alpha/D = K/r_{th}$.

4.2.2 Modified Green-Ampt approach

To account for a dynamic capillary pressure in the equation of motion (4.5), we add and subtract $p_a/(\rho g)$ in the enumerator on the right hand side, and use Eqs. (4.3) and (4.15):

$$\frac{(\theta_s - \theta_i)}{K} \dot{l}\, l = \begin{cases} S_0 + H_0 - \dfrac{\sigma}{D\rho g} \mathcal{E}(\varepsilon, \theta_i)\, \alpha \mathrm{Ca}^{\beta} - l \\ \qquad \text{for upward infiltration} \\ \\ S_0 + H_0 - \dfrac{\sigma}{D\rho g} \mathcal{E}(\varepsilon, \theta_i)\, \alpha \mathrm{Ca}^{\beta} + l \\ \qquad \text{for downward infiltration} \end{cases} \tag{4.16}$$

where

$$S_0 = \frac{\sigma}{D\rho g} \mathcal{E}(\varepsilon, \theta_i) \cos \vartheta_{eq} \tag{4.17}$$

is the equilibrium suction head. Equation (4.16) generalizes the GA approach to account for a dynamic capillary pressure where the nonequilibrium capillary pressure depends on Ca in form of a power law. (Other functional forms are possible too.) We will solve this ODE subject to the initial condition $l(t = 0) = 0$ which applies to the Tabuchi [35] experiments.

To nondimensionalize the ODE, we introduce a nondimensional time

$$\tau = \frac{K}{(\theta_s - \theta_i) H_{eq}} t \tag{4.18}$$

and a nondimensional front position

$$\lambda = l / H_{eq} \tag{4.19}$$

where $H_{eq} = H_0 + S_0$ is the equilibrium height of the water table for the case of upward infiltration. In this paper, we assume that $H_{eq} > 0$. For a dynamic capillary pressure when $Ca > 0$, this assumption is a necessary condition for liquid infiltration as can be seen by evaluation of Eq. (4.16) for $t = 0$. For a constant capillary pressure when Ca $= 0$, the condition only excludes the case of steady-state downward infiltration. The nondimensional equation of motion becomes

$$1 - \mathrm{Bo}_\star^{-1} \mathcal{E}(\varepsilon, \theta_i)\, \widehat{\alpha} \lambda'^{\beta} = \begin{cases} \lambda\,(\lambda' + 1) & \text{for upward infiltration} \\ \\ \lambda\,(\lambda' - 1) & \text{for downward infiltration} \end{cases} \tag{4.20}$$

where

$$\widehat{\alpha} = \alpha \left(\frac{K}{\theta_s - \theta_i} \frac{\eta}{\sigma} \right)^{\beta} \tag{4.21}$$

and $\lambda' = d\lambda/d\tau = (\theta_s - \theta_i)\, \dot{l}/K$ is the nondimensional front velocity, and

$$\mathrm{Bo}_* = \frac{D H_{eq} \rho\, g}{\sigma} \tag{4.22}$$

is a modified Bond number that is similar to the Bond number $\mathrm{Bo} = \rho g L^2/\sigma$ which uses only one typical length scale L.

4.2.3 Semi-analytical solution for the Green-Ampt approach: power law model for dynamic contact angle

Equation (4.16) and its nondimensional version Eq. (4.20) constitute implicit ODEs for the front position $l(t)$. These ODEs can be relatively easily solved numerically once the functional form of p_c, including the ϑ dependence on Ca, is known. We can, however, obtain a semi-analytical solution of Eq. (4.20) by adopting methods that were originally used to derive analytical solutions for infiltration into inclined capillary tubes [14]. Here semi-analytical means that we obtain an analytical solution for the front velocity λ'; however, the front position λ has to be determined through numerical integration of λ'.

Equation (4.20) is difficult to solve analytically, because it is nonlinear (unless $\beta = 1$). We can, however, obtain an implicit analytical solution for the interface velocity λ' by dividing Eq. (4.20) by $\lambda' + 1$ for upward infiltration and by $\lambda' - 1$ for downward infiltration, and by differentiating the resulting equations with respect to τ. We then obtain an ODE

for the interface velocity λ' for which we now introduce the symbol ζ:

$$\zeta = \begin{cases} \dfrac{\mathrm{Bo}_*^{-1}\mathcal{E}(\varepsilon,\theta_i)\,\widehat{\alpha}(1-\beta)\,\zeta^{\beta} - \mathrm{Bo}_*^{-1}\mathcal{E}(\varepsilon,\theta_i)\,\widehat{\alpha}\beta\zeta^{\beta-1} - 1}{(\zeta+1)^2}\zeta' \\ \qquad \text{for upward infiltration} \\ \\ \dfrac{\mathrm{Bo}_*^{-1}\mathcal{E}(\varepsilon,\theta_i)\,\widehat{\alpha}(1-\beta)\,\zeta^{\beta} + \mathrm{Bo}_*^{-1}\mathcal{E}(\varepsilon,\theta_i)\,\widehat{\alpha}\beta\zeta^{\beta-1} - 1}{(\zeta-1)^2}\zeta' \\ \qquad \text{for downward infiltration} \end{cases} \tag{4.23}$$

This ODE needs to be solved subject to the initial condition

$$\zeta(\tau=0) = \zeta_0 = \left(\frac{\mathrm{Bo}_*}{\mathcal{E}(\varepsilon,\theta_i)\widehat{\alpha}}\right)^{1/\beta} \tag{4.24}$$

which can be obtained by setting $\lambda(\tau=0)=0$ and $\tau=0$ in Eq. (4.20).

Separation of the variables in Eq. (4.23) and subsequent integration yields an analytical

solution for the nondimensional travel time τ as a function of the front velocity ζ:

$$\tau(\zeta) = \begin{cases} \mathrm{Bo}_*^{-1}\mathcal{E}(\varepsilon,\theta_i)\,\widehat{\alpha}\,(1-\beta)\,I(\beta,1,\zeta,\zeta_0) \\ -\mathrm{Bo}_*^{-1}\mathcal{E}(\varepsilon,\theta_i)\,\widehat{\alpha}\,\beta\,I(\beta-1,1,\zeta,\zeta_0) - I(0,1,\zeta,\zeta_0) \\ \qquad \text{for upward infiltration} \\ \\ \mathrm{Bo}_*^{-1}\mathcal{E}(\varepsilon,\theta_i)\,\widehat{\alpha}\,(1-\beta)\,I(\beta,-1,\zeta,\zeta_0) \\ +\mathrm{Bo}_*^{-1}\mathcal{E}(\varepsilon,\theta_i)\,\widehat{\alpha}\,\beta\,I(\beta-1,-1,\zeta,\zeta_0) - I(0,-1,\zeta,\zeta_0) \\ \qquad \text{for downward infiltration} \end{cases} \tag{4.25}$$

where

$$I(\mu,\Gamma,\zeta,\zeta_0) = \int_{\zeta_0}^{\zeta} \frac{\xi^{\mu-1}}{(\xi+\Gamma)^2}\,d\xi \tag{4.26}$$

is an integral which has been evaluated by Hilpert [14]. For non-integer μ values, the

value of the integral is given by

$$I(\mu,\Gamma,\zeta,\zeta_0) = \begin{cases} \Gamma^{\mu-2}\left[B\left(\mu, 2-\mu, \frac{1}{1+1/\zeta}\right)\right]_{\zeta_0}^{\zeta} \\ \quad \text{for upward infiltration} \\ \quad \zeta \geq 0 \quad \text{and} \quad \zeta_0 \geq 0 \\ \\ |\Gamma|^{\mu-2}\left[B\left(\mu,-1,\zeta\right)\right]_{\zeta_0}^{\zeta} \\ \quad \text{for downward infiltration,} \\ \quad 0 \leq \zeta < 1 \quad \text{and} \quad 0 \leq \zeta_0 < 1 \\ \\ -|\Gamma|^{\mu-2}\left[B\left(2-\mu,-1,\frac{1}{\zeta}\right)\right]_{\zeta_0}^{\zeta} \\ \quad \text{for downward infiltration,} \\ \quad \zeta > 1 \quad \text{and} \quad \zeta_0 > 1 \end{cases} \tag{4.27}$$

where $B(\nu,\eta,T) = \int_0^T t^{\nu-1}/(1+t)^{\nu+\eta}dt$ is the incomplete beta function. See Spanier and Oldham [33] or Hilpert [14, Appendix] for more details on $B(\nu,\eta,T)$.

We can obtain the interface position λ as function of τ by numerically inverting $\tau(\zeta)$ and then integrating $\zeta(\tau)$:

$$\lambda(\tau) = \lambda(0) + \int_0^{\tau} \zeta(\xi)d\xi \tag{4.28}$$

Using Eqs. (4.25) and (4.28), we can now predict the wetting front position λ and the velocity ζ during infiltration, respectively.

4.3 Reanalysis of the Geiger and Durnford experiments on dynamic capillary pressure

We have analyzed the infiltration experiments performed by Geiger and Durnford [9] in order to test our general model for dynamic capillary pressure given by Eq. (4.13) and our more specific model for the Ca dependence of dynamic capillary pressure given by Eq. (4.15). For two Ottawa silica sands labeled as F-14 and F-95, Geiger and Durnford measured the dynamic suction head $S = p_c/(\rho g)$ (labeled as $-h_w$ in their paper) as a function of Darcy velocity q. For the F-95 sand, Geiger and Durnford extracted relatively uniform size fractions, which are labeled as 60–80, 80–100 and 100–140 according to the US standard sieve size system. Table 4.1 shows the properties of the F-95 sands. To focus our study, we only analyzed the data for the three size fractions of the F-95 sand.

Table 4.1: Properties of sands used in the infiltration experiments by Geiger and Durnford.

Medium	D_{50} [μm]	K [cm/s]	Bulk density [g/cm^3]	Porosity ε [−]
F-95	145	6.9×10^{-3}	1.69	0.36
60–80	214	1.7×10^{-2}	1.68	0.37
80–100	162	1.1×10^{-2}	1.66	0.37
100–140	127	7.7×10^{-3}	1.63	0.39

Geiger and Durnford presented the measurements for the three size fractions in a plot of the dimensional suction head S versus the nondimensional Darcy velocity $q^* = q/K$ (see **Figure 4.3a**). The three curves look similar, and it seems possible to collapse the data through a dimensional analysis. To that end, we can assume the three size fractions

to possess the same ϑ_{eq} value, because the fractions all consist of silica minerals. We also assume that the size fractions have about the same porosity ε according to Table 4.1. Since the sands were air-dry, $\theta_i \approx 0$ for all size fractions. With these assumptions, the three plots of S vs. q^* shown in **Figure 4.3a** should collapse onto one another according to Eq. (4.13). For the grain diameter D, we used the measured D_{50} values reported in Table 4.1. We estimated the non-measured air-water interfacial tension by $\sigma = 72 \times 10^{-3}$ N/m [7]. **Figure 4.3b** shows that the three nondimensional $p_c D/\sigma$ vs. $\eta q/\sigma$ curves can indeed be represented by a single curve. This fact can in a way be attributed to Miller similarity [26] among the three sands investigated or to the result of our dimensional analysis which, contrary to Miller and Miller's, explicitly accounts for a dynamic capillary pressure.

We now use the $p_c D/\sigma$ vs. $\eta q/\sigma$ data shown in **Figure 4.3b** to parameterize the power law model for dynamic capillary pressure given by Eq. (4.15). We approximate the $\mathcal{E}$ values of the three experiments by a single value E, since the porosities and the initial water contents of the three sands are about equal, $E \approx \mathcal{E}(\varepsilon, \theta_i)$. The dynamic capillary pressure for the 60–80, 80–100, and 100–140 experiments should then be described by

$$\frac{p_c D}{\sigma} = P_{eq} - f_{neq} \left(\frac{\eta q}{\sigma} \right)^{\beta} \tag{4.29}$$

where the nondimensional equilibrium capillary pressure $P_{eq} = E \cos \vartheta_{eq}$, $f_{neq} = E\alpha/(\theta_s - \theta_i)^{\beta}$ and β are parameters or products of parameters that have not been measured in-

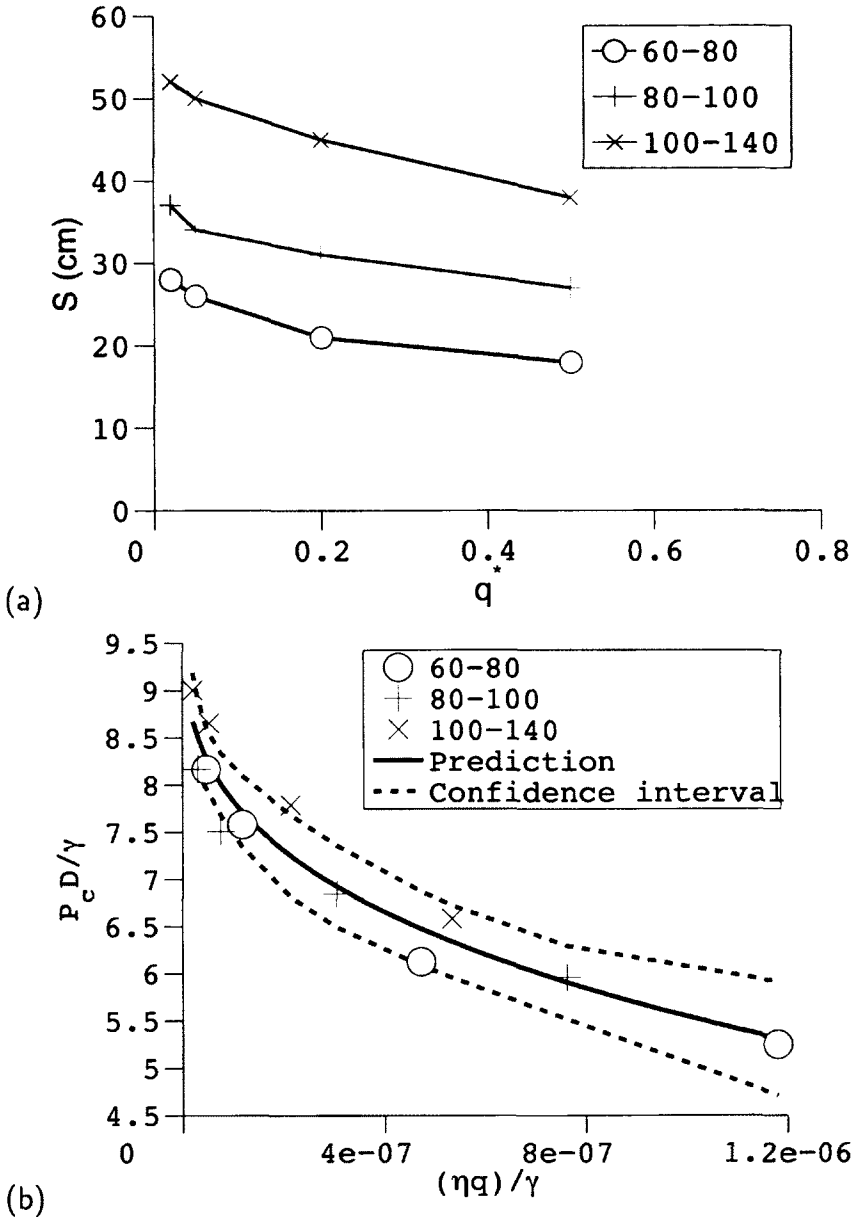

Figure 4.3: (a) Dynamic capillary pressure data from Geiger and Durnford [9]. (b) Fit of the experimental data to our model for dynamic capillary pressure.

dependently by Geiger and Durnford and that need to be fitted. We used the S vs. q^* data of all size fractions to determine P_{eq}, f_{neq} and β through a nonlinear regression analysis. **Figure 4.3b** shows the model prediction including the 95% confidence interval.

Most of experimental data points lie within the confidence interval, suggesting that the model given by Eq. (4.29) predicts the experimental data well. The values of the inversely determined fit parameters including 95% confidence intervals are shown in Table 4.2 (Fit scenario "A"). The relatively large confidence intervals of the fit parameters are likely due to the lack of experimental data as the following consideration suggests.

Seeking to explain the reason for these large confidence intervals, we reduced the number of fit parameters by setting the exponent β to pre-determined values. Relatively little is known about β values in sand. Therefore, in the first place, we considered β to be a fit parameter. We can, however, get clues about β from Weitz's Darcy-scale study which yielded $\beta = 0.5 \pm 0.1$ for water displacing decane in a glass beads column. We also can guess β from pore-scale studies which assume that the dynamic contact angle ϑ on flat surfaces and in circular capillary tubes can be described by $\cos\vartheta_{eq} - \cos\vartheta \sim \mathrm{Ca}^{\beta}$. Theoretical and experimental studies show that β varies between $1/5$ and 1 [31]. Tanner's (1979) law for droplet spreading on a horizontal surface gives $\beta = 2/3$. Capillary tube experiments by Mumley et al. [27] show that $\beta \approx 1/2$ when Ca is around $10^{-5} - 10^{-2}$. Given this wide range of β values, we chose β values of $1/2$, $2/3$ and $1/10$, and used only P_{eq} and f_{neq} as fit parameters. The values of the inversely determined fit parameters are shown in Table 4.2 (Fit scenarios "B", "C" and "D"). All three values of β nicely describe the experimental data. Similar to the case where we fitted β, most of the experimental data points lie within the 95% confidence interval (plots not shown). The residual sum of squares (SSE) of the model prediction is only slightly higher if β is set to a fixed value (see

Table 4.2: Fit of our model for dynamic capillary pressure given by Eq. (4.29) to experimental data by Geiger and Durnford.

	Fit parameters			
Fit scenario	P_{eq}	f_{neq}	β	SSE
A	10.05±3.85	314.73 ± 1663.31	0.31±0.440	1.18
B	9.04±0.45	3605.80 ± 790.62	1/2	1.30
C	8.64±0.41	32729.10 ± 7947.36	2/3	1.56
D	15.56±1.84	39.25 ± 8.69	1/10	1.32
E	8.23±0.43	2.92e+6 ± 9.12e+5	1	2.41
F	7.95±0.49	2.56e+9 ± 1.11e+9	3/2	4.00
G	7.80±0.55	2.24e+12± 1.21e+12	2	5.47

Table 4.2). This fact is likely due to the relatively small range of experimental Ca values which does not allow accurate identification of the exponent β. More accurate β values could likely be determined by performing measurements of dynamic capillary pressure for a much wider range of Ca values.

Even though β is typically assumed to be smaller than one, we also attempted to fit the Geiger and Durnford data by using selected values of $\beta \geq 1$. The resulting fits (Fit scenarios "E"–"G") were not good, however, and led to the large SSE values reported in Table 4.2.

The main finding of this section is that one can collapse the data obtained by Geiger and Durnford for three different size fractions through dimensional analysis. Moreover, our power model for dynamic capillary pressure explains the experimental data, because most experimental data lie within the 95% confidence intervals of the predictions. We could not accurately estimate β; however, a good model fit requires $\beta < 1$.

4.4 Modeling capillary rise experiments by Tabuchi

In **Fig. 4.2**, we have shown the results of the three capillary rise experiments performed by Tabuchi [35]. The three experiments were performed for the different ponding depths H_0 listed in Table 4.3. The final stages of the infiltration experiments, when the wetting fronts approached the equilibrium water table, could not be explained with Eq. (4.6), which assumes capillary pressure to be constant during infiltration. We now investigate whether these final stages can be better described by the modified GA approach which incorporates a dynamic capillary pressure. To do so, we fit the model given by the first case in Eq. (4.20) to each of the three experimental curves. Let us first discuss the parameters that do not require fitting.

The length scale H_{eq} used to relate the dimensional measured front position l to the nondimensional front position λ is known from each of the three experiments. We can assume that the fronts reached the equilibrium water table at the end of the experiments. Hence the three H_{eq} values, which we report in Table 4.3, equal the maximum l values of the three experimental $q\,l$ vs. l curves in **Fig. 4.2**. Moreover, the measured $q\,l$ data can be related to their nondimensional counterpart $\lambda\lambda' = q\,l H_{eq}/K$ because the hydraulic conductivity was reported in Tabuchi [35], $K = 1.8 \times 10^{-2}$ cm/s. More parameters appear in Bo_*, $\mathcal{E}$ and $\widehat{\alpha}$ on the left hand side of Eq. (4.20). The grain-size distribution was relatively uniform and varied between 0.1 and 0.2 mm [35]. We used the arithmetic mean grain size, $D = 0.15$ mm. For the fluid properties, we used $\eta = 10^{-3}$ Pa s, $\sigma = 72 \times 10^{-3}$ N/m and $\rho = 1000$ kg/m^3.

Table 4.3: Some parameters of the three capillary rise experiments performed by Tabuchi.

Experiment	H_0 [cm]	H_{eq} [cm]
A	40	61.57
B	20	34.52
C	12	27.52

This leaves us with the following unknowns: α, β, $(\theta_s - \theta_i)$ and the functional form of $\mathcal{E}$. Since the three Tabuchi experiments were performed in only one soil column, the value of $\mathcal{E}$ becomes a fit parameter $E = \mathcal{E}(\varepsilon, \theta_i)$ where ε is the porosity and θ_i the initial water content of the soil column. Lumping products of unknown parameters in Eq. (4.20), only two fit parameters remain: $f_{neq} = E\alpha/(\theta_s - \theta_i)^\beta$ and β.

Tabuchi did not perform independent experiments to parameterize the dynamic capillary pressure. We first tried using the parameterization from the Geiger and Durnford experiments that we obtained in the previous section. The resulting model predictions (not presented) did not, however, explain the Tabuchi experiments well. This finding is not surprising, because Geiger and Durnford [9] and Tabuchi [35] used different types of soils which cannot be expected to possess the same dynamic capillary pressure parameterizations. Thus we inversely determined both β and f_{neq}. By performing a nonlinear regression analysis, we determined the best-fit values of β and f_{neq} shown in Table 4.4 (Fit Scenario I). **Figure 4.4a** shows that the corresponding best-fit simulations describe the Tabuchi experiments well. For intermediate l values, the data are nicely described by more or less straight lines. Unlike the classical GA approach, our modified approach captures

both the beginning ($l = 0$) and the end of an infiltration experiment ($l = H_{eq}$). At the beginning, $q\,l = 0$, as it should be because $l = 0$ and $q < \infty$ according to Eq. (4.24). At the end, the front correctly approaches the equilibrium water table with an infinitesimally small Darcy velocity, $l \longrightarrow H_{eq}$ and $q \longrightarrow 0$.

Conversely the classical GA approach does not describe the experiments well as shown in **Fig. 4.4b**. The classical GA model overestimates the Darcy velocity q, because the predicted value of $q\,l$ is larger than the measured one for all values of l. Furthermore, the classical GA approach predicts $q\,l = KH_{eq} > 0$ for $l = 0$. This is because the initial rate of infiltration and Darcy velocity are infinite for the time $t = 0$ and front position $l = 0$. Thus the finite $q\,l$ value for $l = 0$ makes sense from the perspective of the classical GA approach. An infinite front velocity, however, does not make physical sense. To remedy the poor model prediction, we can interpret H_{eq} and K (slope of the $q\,l$ vs. l curve) as fit

Table 4.4: Values of fit parameters used to model the three Tabuchi experiments for the three different fit scenarios.

		Fit parameters		
Fit scenario	Experiment	f_{neq}	β	SSE ($\times 10^{-3}$)
I	A	6.30 ± 1.57	0.062 ± 0.019	3.60
	B	3.38 ± 2.75	0.088 ± 0.052	4.37
	C	4.27 ± 1.28	0.075 ± 0.021	0.31
II	A	1640.67 ± 343.06	1/2	162.03
	B	839.59 ± 189.56	1/2	45.35
	C	1532.27 ± 391.80	1/2	25.16
III	A	12933.07 ± 3740.14	2/3	249.32
	B	6972.92 ± 2109.79	2/3	69.51
	C	15412.30 ± 5509.69	2/3	38.28

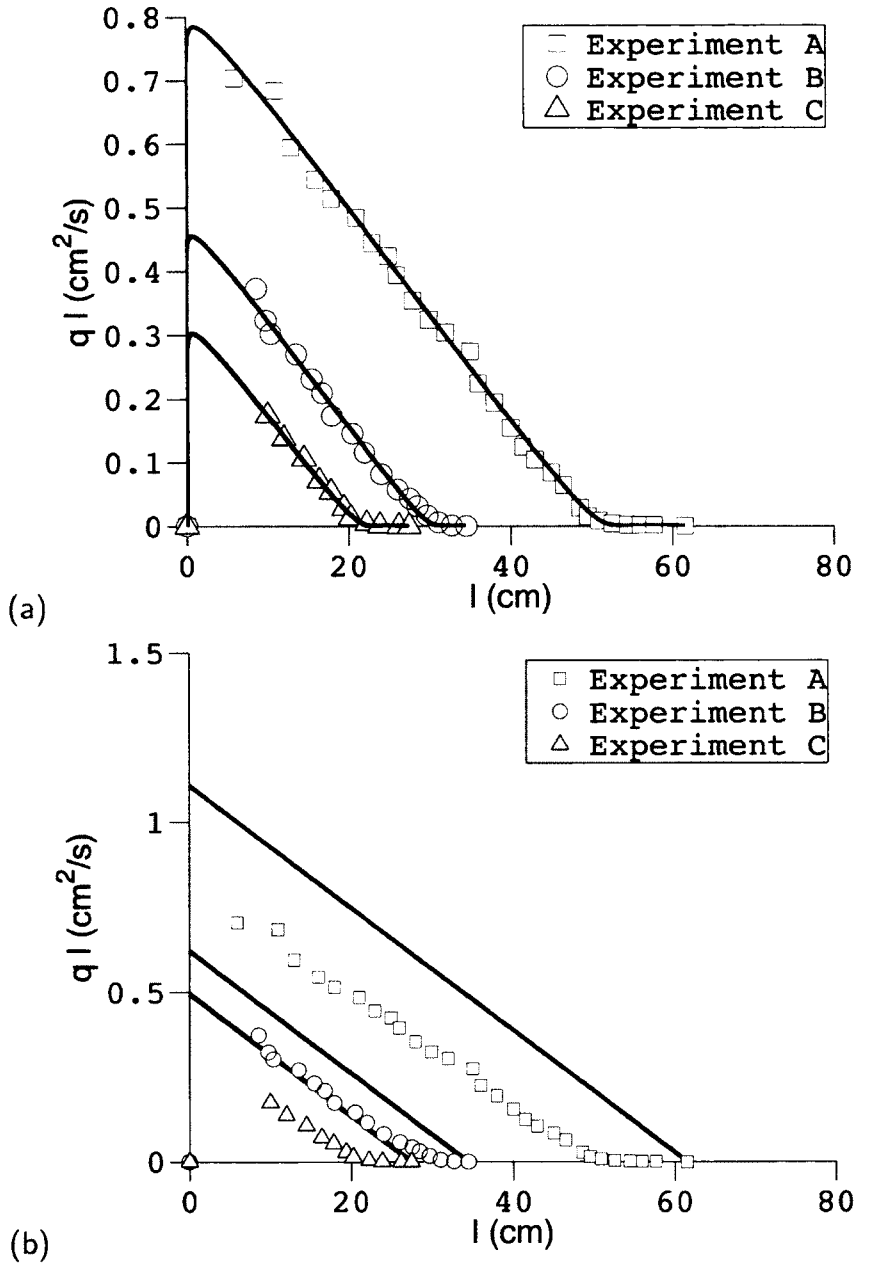

Figure 4.4: (a) Modeling of the capillary rise experiments by Tabuchi with the modified GA approach. Fit parameters: β and f_{neq} (Fit scenario I). (b) Modeling the capillary rise experiments by Tabuchi with the classical GA approach. The agreement is poor because the model prediction uses the measured equilibrium height of the water table, H_{eq}.

parameters. Then the classical GA model describes most of the experimental data points well as shown in **Fig. 4.2**. However, we cannot learn anything from this fitting exercise since K and H_{eq} are known in this example. Even worse is that the model fit does not yield the correct value for H_{eq}, a quantity of considerable hydrological importance.

As in the analysis of the Geiger and Durnford [9] experiments in Sec. 4.3, we also considered two fixed values for the exponent β in the power law model for dynamic capillary pressure: 1/2 and 2/3. Then f_{neq} is the only fit parameter. Table 4.4 lists the inversely determined f_{neq} values (Fit scenarios II and III). For the prescribed values of β, the modified GA approach does not describe the Tabuchi experiments well (plots not shown). Contrary to the analysis of the Geiger and Durnford [9] data, it is crucial to consider β to be a fit parameter. We believe that this is due to the comparatively large range of capillary numbers Ca that occurs during capillary rise, ranging from a quite large initial value down to zero as the equilibrium water table is approached.

4.5 Effects of dynamic capillary pressure on transient infiltration

While the $q\,l$ vs. l plots presented in the previous section have been useful to examine the Tabuchi [35] data, the plots do not clearly illustrate the effects of a dynamic capillary pressure on infiltration. To that end, it is better to illustrate the differences in the temporal behavior of the front position l and Darcy velocity q between the classical and modified GA

approach. We will do so for both downward and upward infiltration. For the simulations that account for a dynamic capillary pressure, we used the hydraulic properties of the porous medium system used in the Tabuchi capillary rise experiments. Specifically, we used the parameterization of dynamic capillary pressure that used β as a fit parameter (Fit scenario I in Table 4.4). We estimated the non-measured mobile water content, which is needed to dimensionalize time t, to be $\theta_s - \theta_i = 0.3$.

To obtain a constant capillary pressure, we set $f_{neq} = 0$. Hence $\widehat{\alpha} = 0$ and, following Green and Ampt [10], one can derive an implicit analytical solution for λ to the nondimensional equation of motion given by Eq. (4.20):

$$\tau(\lambda) = \begin{cases} -\lambda - \log(1-\lambda) & \text{for upward infiltration} \\ \\ \lambda - \log(1+\lambda) & \text{for downward infiltration} \end{cases} \tag{4.30}$$

Figure 4.5a shows the simulation results for upward infiltration. We use a ponding depth $H_0 = 0.4$ m. This value was also used in Tabuchi's Experiment A (see Table 4.3). Thus the $l(t)$ and $q(t)$ curves for a dynamic capillary pressure can actually be used to construct the $q\,l$ versus l plot for Experiment A shown in **Fig. 4.4a**. For both a constant and a dynamic capillary pressure, the front asymptotically approaches the equilibrium water table, $l \longrightarrow H_{eq}$. At the same time, the Darcy velocity vanishes, $q \longrightarrow 0$. For a constant capillary pressure, the front approaches the equilibrium water table at a higher speed than for a dynamic capillary pressure. In fact the speed is initially infinite. This is

a well-known unphysical feature of the classical GA approach.

Figure 4.5b shows the simulation results for downward infiltration where we used a ponding depth $H_0 = 0$ m. For both capillary pressure models, the Darcy velocity q decreases from an initially high value and asymptotically approaches the steady-state Darcy velocity given by the hydraulic conductivity K. This behavior is well known from the classical GA approach. The front position l scales linearly with time t in the late stage of infiltration as q becomes constant. As for upward infiltration, q is initially infinite for a constant capillary pressure and higher than for a dynamic capillary pressure. The difference in q between the two model predictions results in significant differences in the front position l both in the early and late stage of infiltration.

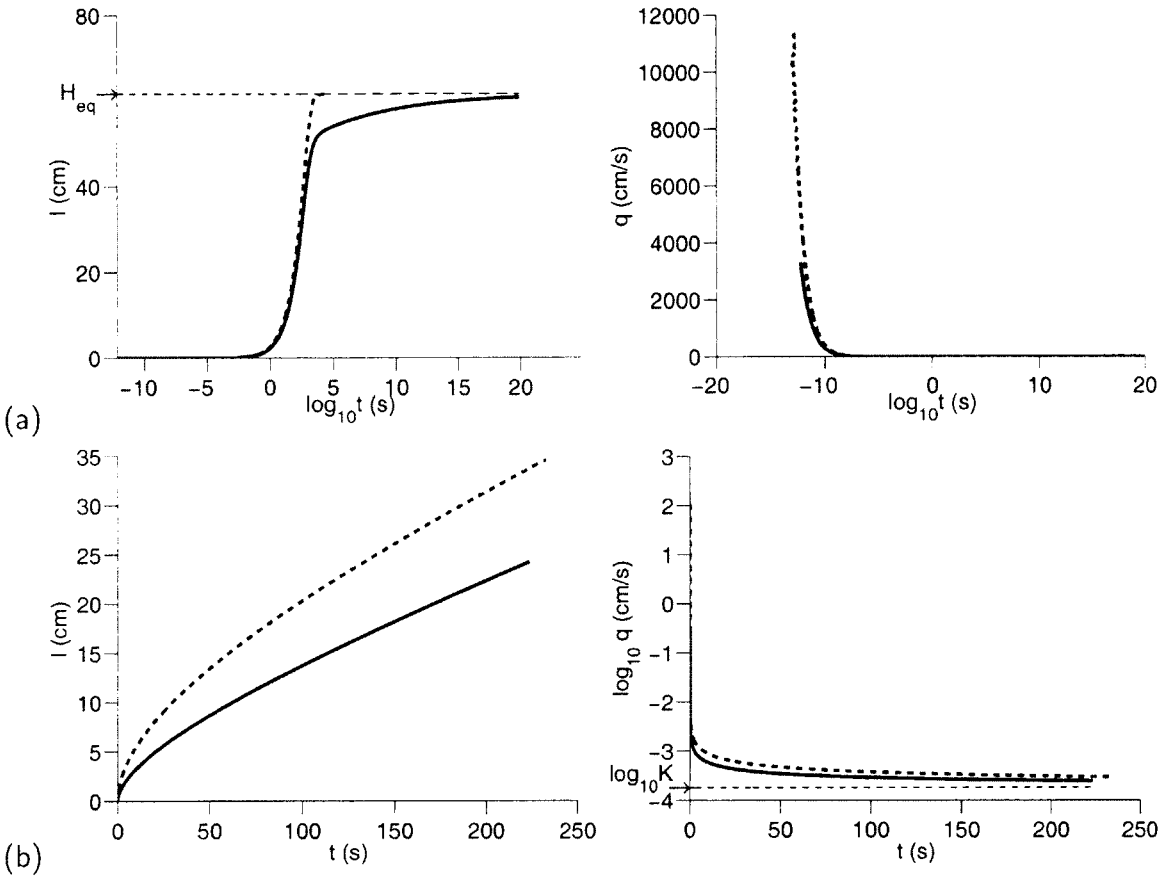

Figure 4.5: Effects of dynamic capillary pressure on (a) upward infiltration and (b) downward infiltration. Left column: front position l versus time t. Right column: Darcy velocity q versus t. Solid lines: modified GA model. Dashed lines: classical GA model.

4.6 Comparison of dynamic capillary pressure relations

Finally we compared the data on capillary pressure as a function of Ca that we assembled to one another, that is, the Weitz et al. and the Geiger and Durnford data as well as the dynamic capillary pressures that we inversely determined from the Tabuchi experiments. For the comparison, we nondimensionalized the Weitz et al. data so that it conforms to Eq. (4.29). To do so, we multiplied Eq. (4.7) by D/σ. Consistency with Eq. (4.29) requires $P_{eq} = D/r_{th}$ and $f_{neq} = DK/r_{th}$. Since $\sigma = 41$ dyn/cm, $D = 0.5$

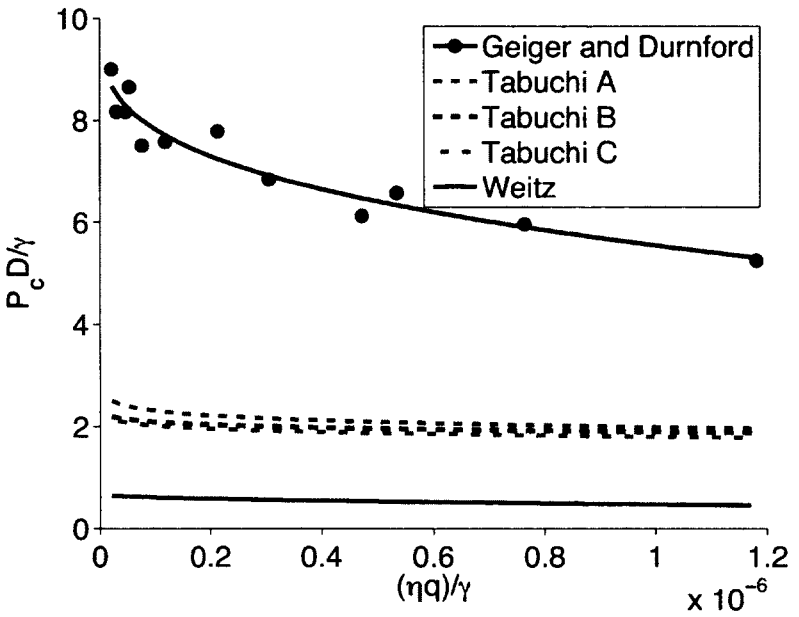

Figure 4.6: Nondimensional capillary pressure versus $\eta q/\sigma$ for the Geiger and Durnford, the Tabuchi, and the Weitz et al. experiments.

mm, $K = 300 \pm 50$ and $r_{th} = 0.745 \pm 0.068$ mm for the Weitz et al. experiments, we determined $P_{eq} = 0.67 \pm 0.06$ and $f_{neq} = 201 \pm 38$.

The comparison in **Figure 4.6** shows that the $p_c D/\gamma$ vs. $\eta q/\sigma$ curves have similar shapes, with $p_c D/\gamma$ decreasing as $\eta q/\sigma$ increases. The three curves inversely determined from the three Tabuchi experiments are close to one another, suggesting that the inverse parameter identification is robust. **Figure 4.6** also illustrates that the three individual experiments have very different P_{eq} values. This is quite likely due to different equilibrium contact angles ϑ_{eq}, on which P_{eq} depends according to Eq. (4.15). The nondimensional capillary pressures of the Geiger and Durnford experiments are about four times higher than those of the Tabuchi experiments, although both experiments used air and water as the fluids. This difference is likely due to the different types of porous media used in

the experiments. The grains are of different mineralogy suggesting, for example, different equilibrium contact angles ϑ_{eq}, which can easily explain a factor of four. Moreover, the grains may have a different surface roughness, which should also affect P_{eq} and f_{neq}. The P_{eq} value of the Weitz et al. experiments is much lower than those of the Geiger and Durnford as well as the Tabuchi experiments, potentially because the decane-water-glass bead system is closer to neutral wettability than the air-water systems.

4.7 Discussion and summary

In the classical GA model, capillary pressure at the wetting front is assumed to remain constant during infiltration. We generalized this model to account for a capillary pressure that depends on the flow velocity. Based on dimensional analysis and physical considerations, we posited the functional form for dynamic capillary pressure given by Eqs. (4.13) and (4.15). This mathematical model describes measurements of capillary pressure versus Darcy velocity by Weitz et al. [39] and Geiger and Durnford [9] well. Moreover, our dimensional analysis allows us to collapse three dynamic capillary pressure curves that have been obtained by Geiger and Durnford for sands of different grain size onto one curve. The relatively small range of capillary numbers Ca used in the Geiger and Durnford experiments did not, however, allow us to determine accurately the parameterization of the power law model for the nonequilibrium capillary pressure, that is, the exponent β.

The functional form that we suggest seems to improve the one suggested by Weitz et al., because our model explicitly accounts for a contact angle ϑ. In the Weitz et al. model,

the equilibrium capillary pressure is given by σ/r_{th} according to Eq. (4.7). Since this formula does not account for ϑ, Weitz et al. fitted a characteristic throat radius that is larger than the grain diameter, $R_t = 0.745$ mm > 0.5 mm $= D$, which does not make geometrical and physical sense. By assuming that the Darcy-scale dynamic capillary pressure depends on ϑ, which is clearly supported by pore-scale physics, this inconsistency can be avoided. This assumption is also supported by the infiltration study by Weisbrod et al. [38].

The modified GA approach describes the capillary rise experiments performed by Tabuchi well (see **Figure 4.4a**). In contrast, the final stages of these experiments, during which the front approached the equilibrium water table, cannot be described by the classical GA model (see **Figure 4.2** and **Figure 4.4b**). Since Tabuchi did not independently measure the relationship between the dynamic capillary pressure and capillary number, we inversely determined this relationship from the data for the capillary rise experiments. We did so separately for each of the three experiments that Tabuchi performed for three different ponding depths H_0. The values of the three resulting sets of fit parameters are quite close to one another and suggest that the power law model for dynamic capillary pressure according to Eqs. (4.15) and (4.29) is a suitable choice not only for the Weitz et al. and Geiger and Durnford but also for the Tabuchi experiments.

Our assumed equation for dynamic capillary pressure in a porous medium, Eq. (4.15), is mathematically equivalent to power law models for dynamic contact angle on impermeable flat surfaces or in capillary tubes. However, the values of the exponent that we determined

for the soils used in the Tabuchi experiments, $0.062 \leq \beta \leq 0.087$, is much lower than the values of β on impermeable surfaces (see Sec. 4.3). For glass beads, however, Weitz et al. determined $0.4 < \beta < 0.6$, which corresponds to β values on impermeable surfaces. This suggests that β is a function of porous medium properties (e.g. surface roughness) and fluid properties.

In Section 4.5, we have shown that a dynamic capillary pressure significantly affects transient downward and upward infiltration. For both downward and upward infiltration, the Darcy velocity q initially diverges in the classical GA model. This unphysical behavior is well known and also occurs in the classical Lucas-Washburn theory for infiltration into a capillary tube [25, 37, 15]. As is the case for infiltration into capillary tubes [13, 14], a capillary pressure that depends on the flow velocity avoids the infinite initial velocity in the GA approach.

When modeling the front position l and the front velocity $\dot{l}$ as a function of time t, we pursued a semi-analytical approach. Following the lines of Hilpert [14], we derived the implicit analytical solution given by Eq. (4.25) for the front velocity. We then obtained the front position numerically by inverting the implicit solution and integrating it. The semi-analytical approach may be computationally less expensive than solving the ODE given by Eq. (4.20) numerically.

While we generalized the GA approach to account for a flow-velocity dependent capillary pressure at the infiltration front, there are also efforts underway that generalize Richards' equation for variably-saturated flow. Such a theory can be used to describe the

diffuse wetting front that occurs during water infiltration including saturation overshoot which also has been linked to a dynamic capillary pressure [6]. Some of these efforts account for a dynamic capillary pressure in the form of a rate law, which assumes the actual capillary pressure p_c to relax towards an equilibrium capillary pressure, p_c^{eq}, as follows [34, 12]:

$$\frac{\partial s}{\partial t} = -\tau(p_c - p_c^{eq}) \tag{4.31}$$

where s is the water saturation, and τ is a relaxation parameter that depends on other system variables. While this relaxation model can be built into thermodynamically consistent theories for multiphase flow [11, 19], determination of τ is subject of ongoing research [3, 28, 30, 22], and the rate law has so far not been rigorously derived. Our functional form for dynamic capillary pressure at the wetting front could potentially inform efforts in determining a functional form for the nonequilibrium capillary pressure to be used in Richards' equation. One needs to be careful when comparing Eq. (4.15) to Eq. (4.31), because they are formulated in a Lagrangian and a Eulerian framework, respectively. It seems conceivable, however, that the left hand side of Eq. (4.31) could potentially depend on the water or the front velocity through a power law. It would be interesting to check whether the Tabuchi experiments and in particular the $q\,l$ versus l plots can be modeled by Richards' theory, with or without accounting for a dynamic capillary pressure.

Finally, we would like to comment on the conjecture of Iwata et al. [18] that the final stages of capillary rise experiments performed by Tabuchi could potentially be explained by a dynamic contact angle. By relating the dynamic contact angle to a dynamic capillary

pressure at the wetting front and analyzing published infiltration experiments, we have provided evidence that the conjecture of Iwata et al. is correct, even though we could not directly observe the contact angle. In retrospect, the conjecture is quite visionary, particularly as still today the vast majority of flow models used in hydrology and petroleum engineering, formulated at both the pore-scale and the Darcy-scale, assumes a constant contact angle which does not depend on flow velocity.

4.8 Acknowledgments

This work was supported by NSF Grants EAR-0739038 and CBET-0730932. We would like to thank Dr. Sho Shiozawa and Ms. Keiko Nakano from the Graduate School of Agricultural and Life Sciences at the University of Tokyo for providing us with a hardcopy of the paper by Tabuchi [35].

Bibliography

[1] T.D. Blake and J.M. Haynes. Kinetics of liquid/liquid displacement. *Journal of Colloid and Interface Science*, 30(3):421–423, 1969.

[2] R.G. Cox. Dynamics of the spreading of liquids on a solid surface. Part 1. Viscous flow. *Journal of Fluid Mechanics*, 168:169–194, 1986.

[3] H.K. Dahle, M.A. Celia, and S.M. Hassanizadeh. Bundle-of-tubes model for calculating dynamic effects in the capillary-pressure-saturation relationship. *Transport in Porous Media*, 58:5–22, 2005.

[4] P.G. de Gennes, X. Hua, and P. Levinson. Dynamics of wetting: Local contact angles. *Journal of Fluid Mechanics*, 212:55–63, 1990.

[5] DiCarlo. Capillary pressure overshoot as a function of imbibition flux and initial water content. *Water Resources Research*, 43:W08402, 2007. doi: 10.1029/2006WR005550.

[6] D.A. DiCarlo. Modeling observed saturation overshoot with continuum additions to standard unsaturated theory. *Advances in Water Resources*, 28:1021–1027, 2005.

[7] R. W. Fox, A. T. McDonald, and P. J. Pritchard. *Introduction to Fluid Mechanics*. Academic Press, Incorporated, 2004.

[8] S.P. Friedman. Dynamic contact angle explanation of flow rate-dependent saturation-pressure relationships during transient liquid flow in unsaturated porous media. *Journal of Adhesion Science and Technology*, 13(12):1495–1518, 1999.

[9] S.L. Geiger and D.S. Durnford. Infiltration in homogeneous sands and a mechanistic model of unstable flow. *Soil Science Society of America Journal*, 64(2):460–469, 2000.

[10] W.H. Green and G.A. Ampt. Studies on soil physics Part I – The flow of air and water through soils. *Journal of Agricultural Science*, 4(Part 1):1–24, 1911.

[11] S. M. Hassanizadeh and W. G. Gray. Toward an improved description of the physics of two-phase flow. *Advances in Water Resources*, 16(1):53–67, 1993.

[12] S.M. Hassanizadeh, M.A. Celia, and H.K. Dahle. Dynamic effects in the capillary pressure-saturation relationship and their impacts on unsaturated flow. *Vadose Zone Journal*, 1:38–57, 2002.

[13] M. Hilpert. Effects of dynamic contact angle on liquid infiltration into horizontal capillary tubes: (semi)-analytical solutions. *Journal of Colloid and Interface Science*, 337(1):131–137, 2009.

[14] M. Hilpert. Effects of dynamic contact angle on liquid infiltration into inclined

capillary tubes: (semi)-analytical solutions. *Journal of Colloid and Interface Science*, 337:138–144, 2009.

[15] M. Hilpert. Explicit analytical solutions for liquid infiltration into capillary tubes: dynamic and constant contact angle. *Journal of Colloid and Interface Science*, 344: 198–208, 2010.

[16] M. Hilpert, J. F. McBride, and C. T. Miller. Investigation of the residual-funicular nonwetting-phase-saturation relation. *Advances in Water Resources*, 24(2):157–177, 2001.

[17] R. L. Hoffman. A study of the advancing interface. *Journal of Colloid and Interface Science*, 50(2):228–241, 1975.

[18] S. Iwata, T. Tabuchi, and B.P. Warkentin. *Soil-water interactions: mechanisms and applications*. Marcel Dekker, New York, 2nd edition, 1995.

[19] A.S. Jackson, C.T. Miller, and W.G. Gray. Thermodynamically constrained averaging theory approach for modeling flow and transport phenomena in porous medium systems: 6. Two-fluid-phase flow. *Advances in Water Resources*, 32(6):779–795, 2009.

[20] G. R. Jerauld and S. J. Salter. The effect of pore-structure on hysteresis in relative permeability and capillary pressure: Pore-level modeling. *Transport in Porous Media*, 5(2):103–151, 1990.

[21] J.F. Joanny and M.O. Robbins. Motion of a contact line on a heterogeneous surface. *The Journal of Chemical Physics*, 92:3206–3212, 1990.

[22] V. Joekar-Niasar, S.M. Hassanizadeh, and H.K. Dahle. Non-equilibrium effects in capillarity and interfacial area in two-phase flow: Dynamic pore-network modelling. *Journal of Fluid Mechanics*, 655:38–71, 2010.

[23] P. Joos, P. van Remoortere, and M. Bracke. The kinetics of wetting in a capillary. *Journal of Colloid and Interface Science*, 136, 1990.

[24] T.X. Lu, J.W. Biggar, and D.R. Nielsen. Water movement in glass bead porous media. 1. Experiments of capillary rise and hysteresis. *Water Resources Research*, 30:3275–3281, 1994.

[25] R. Lucas. Ueber das Zeitgesetz des kapillaren Aufstiegs von Flüssigkeiten [On the time law of the capillary rise of liquids]. *Kolloid-Zeitschrift*, 23(1):15–22, 1918.

[26] E. E. Miller and R. D. Miller. Physical theory of capillary flow phenomena. *Journal of Applied Physics*, 27(4):324–332, 1956.

[27] T.E. Mumley, C.J. Radke, and M.C. Williams. Kinetics of liquid/liquid capillary rise. I. Experimental observations. *Journal of Colloid and Interface Science*, 109(2): 398–412, 1986.

[28] D.M. O'Carroll, T.J. Phelan, and L.M. Abriola. Exploring dynamic effects in capillary pressure in multistep outflow experiments. *Water Resources Research*, 41:1–14, 2005.

[29] L. A. Richards. Capillary conduction of liquids in porous media. *Physics*, 1:318–333, 1931.

[30] T. Sakaki, D.M. O'Carroll, and T.H. Illangasekare. Direct quantification of dynamic effects in capillary pressure for drainage-wetting cycles. *Vadose Zone Journal*, 9: 424–437, 2010.

[31] E. Schäffer and P. A. Wong. Contact line dynamics near the pinning threshold: A capillary rise and fall experiment. *Physical Review E*, 61(5):5257–5277, 2000.

[32] A. Siebold, M. Nardin, J. Schultz, A. Walliser, and M. Oppliger. Effect of dynamic contact angle on capillary rise phenomena. *Colloids and Surfaces A: Physicochemical and Engineering Aspects*, 161(1):81–87, 2000.

[33] J. Spanier and K.B. Oldham. *An atlas of functions*. Taylor & Francis/Hemisphere, Bristol, PA, USA, 1987.

[34] F. Stauffer. Time dependence of the relations between capillary pressure, water content and conductivity during drainage of porous media. *IAHR Symp. on Scale Effects in Porous Media. Thessaloniki Greece 29 Aug.-1 Sept. 1978. IAHR, Madrid, Spain*, 1978.

[35] T. Tabuchi. Infiltration and capillarity in the particle packing [in Japanese]. *Rec. Land Reclam. Res.*, 19:1–121, 1971.

[36] L. H. Tanner. The spreading of silicone oil drops on horizontal surface. *J. Phys. D*, 12:1473–1484, 1979.

[37] E. W. Washburn. The dynamics of capillary flow. *Physical Review*, 17:273–283, 1921.

[38] N. Weisbrod, T. McGinnis, M.L. Rockhold, and M.R. Niemet. Effective darcy-scale contact angles in porous media imbibing solutions of various surface tensions. *Water Resources Research*, 45(W00D39), 2009. doi: 10.1029/2008WR006957.

[39] D. A. Weitz, J.P. Stokes, R.C. Ball, and A.P. Kushick. Dynamic capillary pressure in porous media: Origin of the viscous-fingering length scale. *Physical Review Letters*, 59(26):2967–2970, 1987.

Chapter 5. Summary, engineering application, and future work

5.1 Summary

Chapter 2 examined the effect of contact angle hysteresis on the mobilization of a blob in a model pore doublet. Contact angle hysteresis was linked to the Jamin effect, which explains both the trapping of residual NAPL blobs and their mobilization. Experiments with a model pore doublet showed that the Jamin effect on a blob in a straight capillary tube can be explained entirely through contact angle hysteresis. The blob can sustain pressure gradients, without moving away from its original position, by changing its interfacial shape (curvatures) and contact angles. Once the contact angles reached the receding/advancing contact angles, the pressure which the blob sustained was the critical pressure for mobilizing the blob.

By taking advantage of PLIF technique, I was able to measure the contact angles in 2D and 3D, as well as curvatures of blob menisci. A 3D blob image was reconstructed from a series of images on parallel planes across the blob. The contact angles and the curvatures of menisci in 3D were then determined by analyzing the 3D blob images. The results show that the contact angles measured in both 2D and 3D along a contact line depend

on the altitude due to contact angle hysteresis and gravity. Based on the Poiseulle flow assumption and the Young-Laplace equation, the pressure drops calculated from mean curvatures and 2D/3D contact angles are in line with the measured pressure drops.

The method introduced in Chapter 2 for determining capillary pressure based on mean curvature measurements in a capillary tube can be extended to calculating capillary pressure in geometrically complex porous media, such as reservoir rocks. In these geometries, one cannot easily infer capillary pressure from measured contact angles due to the highly variable pore boundaries, but one can use this method to measure mean curvatures and then calculate the capillary pressure. In addition, the methods in Chapter 2 for determining curvature and contact angles from 3D images can also be applied to other types of images, e.g., those measured by X-ray CMT.

Approaches to accounting for contact angle hysteresis are of interest in emerging Darcy-scale theories for multiphase flow that can be used to describe blob mobilization during an EOR or ground water remediation. For example, the relative permeability can be affected by contact angle hysteresis, which decreases the mobility of residual oil blobs. Without taking contact angle hysteresis into account, models would overestimate the relative permeability.

The simple 1D model pore system, discussed in Chapter 3, was formulated to describe the response of a blob in a capillary tube to an oscillatory external pressure difference. In this model, the three-phase contact points of the blob are assumed to be pinned, and the flow is assumed to be axial-symmetric, oriented along the tube axis, and incompressible.

This model theoretically predicts the resonance of the blob, and the occurrence of resonance which depends on the density and viscosity of liquids, interfacial tension, contact angle, and the radius of the tube.

Using the PLIF technique, the response of the blobs to oscillatory pressure differences was visualized and measured. The results agreed with the prediction of the 1D model that a blob can resonate in a horizontally-oriented capillary tube. Furthermore, the experiments showed that a blob also resonates in a sphere packing, a phenomenon which has not yet been documented in the literature. Although the geometrical difference between the 1D model and the blob in the sphere packing is significant, the predicted resonant frequency agrees fairly well with the measured one.

Because of the complicated shape of a blob in a sphere packing, a fully analytical expression of the frequency response of the blob has not yet been derived. Computational fluid dynamic techniques, such as those based on the lattice-Boltzmann (LB) method [6], could be used to predict the frequency response of blobs, but, such simulations require significant computational time. In contrast, the 1D pore model provides a simple means of predicting the occurrence of blob resonance in porous media and arriving at rough estimates of the frequency response.

The work presented in Chapters 2 and 3, demonstrats the ability of the PLIF technique to visualize and quantify the dynamics/movement of blobs or menisci in porous media. In Chapter 2, the PLIF technique was successfully used to visualize the meridian profile of a blob subjected to different pressure gradients created by a prescribed bypass flow in

a model pore doublet. The experiments presented in Chapter 3 determined the dynamic response of menisci in porous media to oscillatory pressure differences and showed the ability of PLIF to record the images with high temporal resolution. These high quality images were used develop the relationship between changing contact angles and blob displacement. Based on the relationship, an additional coefficient was determined to incorporate the effects of gravity on the shape of menisci. This significantly reduced the difference between the predictions of the simple 1D model and the measured data.

The Green-Ampt (GA) model was generalized to account for a capillary pressure that depends on the Darcy velocity. Based on a dimensional analysis and physical considerations, a functional form was proposed for dynamic capillary pressure given by a power law. This mathematical model successfully describes measurements of capillary pressure versus Darcy velocity taken by Weitz et al. [16] and Geiger and Durnford [5]. Moreover, by dimensional analysis, the three dynamic capillary pressure curves that were obtained by Geiger and Durnford for sands of different grain size can be represented on a single curve.

The modified GA approach describes the capillary rise experiments performed by Tabuchi [15] well. In contrast, the final stages of these experiments, during which the front approached the equilibrium water table, cannot be described by the classical GA model. Since Tabuchi did not independently measure the relationship between the dynamic capillary pressure and capillary number, I inversely determined this relationship from the data for the capillary rise experiments. I did this separately for each of the three experiments that Tabuchi performed for three different ponding depths. The values of the

three resulting sets of fit parameters are quite close to one another and suggest that the power law model for dynamic capillary pressure is a suitable choice not only for Weitz et al. [16] and Geiger and Durnford [5] but also for the Tabuchi experiments.

The equation for dynamic capillary pressure in a porous medium is mathematically equivalent to power law models for dynamic contact angle on impermeable flat surfaces or in capillary tubes. However, the values of the exponent, β, that I determined for the soils used in the Tabuchi experiments is much lower than the one for impermeable surfaces. In contrast, Weitz et al. [16] determined $0.4 < \beta < 0.6$ for glass beads, which corresponds to β values on impermeable surfaces. This suggests that β is a function of porous medium properties (e.g. surface roughness) and fluid properties.

A semi-analytical approach was taken to modeling the front position and the front velocity as a function of time. Following the method of Hilpert [7], I derived the implicit analytical solution for the front velocity. The front position was numerically obtained by inverting the implicit solution and integrating it. The semi-analytical approach may be computationally less expensive than solving the ODE numerically.

Finally, Iwata et al. [10] conjectured that the final stages of capillary rise experiments performed by Tabuchi could potentially be explained by a dynamic contact angle. By relating the dynamic contact angle to a dynamic capillary pressure at the wetting front and analyzing published infiltration experiments, I have provided evidence that the conjecture of Iwata et al. [10] is correct, even though I could not directly observe the contact angle. It should be noted that the majority of flow models, at both the pore-scale and the Darcy-

scale, used in hydrology and petroleum engineering today still assume a constant contact angle that is independent of flow velocity.

5.2 Engineering applications

In environmental engineering, the mobilization of residual NAPL blobs is one of the major issues of groundwater remediation. Hunt et al. [9] showed that simple pumping is not sufficient to mobilize trapped NAPL blobs without changing the fluid properties or using unrealistically high flow rates. A variety of enhanced groundwater remediation methods have been developed that either mobilize the NAPL as a liquid or enhance the mass transfer process from the NAPL into the surrounding groundwater. These methods include surfactant flushing [13], polymer flooding [11], freeze-thaw [12], and vibratory or acoustical enhancement [14, 3].

A theory proposed by Hilpert et al. [8] hypothesized that the mobilization of trapped blobs can be enhanced by exploiting capillarity-induced resonance. The findings in Chapters 2 and 3 that the blob can sustain pressure drops and that the trapped blob can exhibit resonance in porous media support the potential of exploiting blob resonance to improve the method of vibratory enhancement.

The work presented in Chapter 2, showed that a NAPL blob can be mobilized when the contact angles reach their limiting value (receding/advancing contact angle). When a blob in a porous medium is subjected to vibratory pressure differences of uniform amplitude, the frequency response of the blob (shown in Chapter 3) indicated that the displacement

amplitude of the menisci will be more extensive with excitation at the resonant frequency than at other frequencies. Since the contact points are pinned, the change of the menisci due to resonance will increase/decrease the contact angles enormously. Once the contact angles reach the receding/advancing contact angles, the blob will have a good chance of mobilization. Nevertheless, the contact-line motion is not well-understood, and the concept mentioned above may be just one of many possible scenarios of blob mobilization.

5.3 Future work

Building on the results presented in Chapter 2, it would be interesting to examine the transition behavior of a trapped blob that is subsequently mobilized by static and dynamic pressure gradients. For static pressure gradients, Dong et al. [4] found that the blob moved away from its original position only after a wetting liquid film formed around the blob and the blob snapped. However, our data showed that the menisci of the blob moved without forming a film due to sliding contact lines. The difference between the two blob mobilization scenarios has not been well-studied. With the model pore doublet (Chapter 2), experiments can be performed to determine or under different the flow conditions, (e.g., different capillary number or Bond number), for different blob behaviors. In addition, the occurrence of different mobilization scenarios might be examined for the different topographical and chemical conditions on the surface of the solid phase. A similar experimental procedure can be used for dynamic pressure gradients, e.g., oscillatory pressure differences. It is expected that the inertial force will be a major factor in the blob

moving mechanism.

The experimental work presented in Chapter 3 showed a blob resonating in a sphere packing, but there is as yet no theoretical description of this resonance, nor of the resonance of a blob in a generic porous medium (e.g., a sand packing). The 1D model prescribed in Chapter 3 can be extended to a 3D model, but the main challenge for deriving an analytical solution of the 3D model will be to account for the complicated shape of the blob. This difficulty might be overcome by solving the problem numerically.

As mentioned in Section 5.2, a theory can be built by combining the findings in Chapters 2 and 3 to model the enhancement of blob mobilization due to blob resonance. Theories have been developed for enhancing blob mobilization by using oscillatory pressure differences [2, 1]. However, they do not take blob resonance into account, and the models are limited to certain types of blob mobilization. To determine the effect of blob resonance on blob mobilization, the model in Chapter 3 could be embedded into these existing models or built into a new model which can well describe different transition behaviors of blob mobilization.

To advance the applicability of the work described in Chapter 3, one might wish to study the simultaneous responses of several residual blobs to oscillatory pressure differences in porous media. In real groundwater reservoirs, the sizes and shapes of the residual NAPL blobs are non-uniform, as are the resonant frequencies of the blobs. Deriving an analytical expression and performing experiments/simulations for the response of blobs of variable site distribution in porous media to vibratory excitation will help to optimize the excitation

process for mobilizing multiple residual blobs for EOR or groundwater remediation.

Although I generalized a modified Green-Ampt approach to account for a flow-velocity dependent capillary pressure at the infiltration front (Chapter 4), there are also studies that generalize Richards' equation for variably-saturated flow. The functional form in Chapter 4 for dynamic capillary pressure at the wetting front could potentially inform efforts to determine a functional form for the nonequilibrium capillary pressure to be used in Richards' equation. Furthermore, it would be interesting to check whether the Tabuchi experiments, and in particular the $q\,l$ versus l plots, can be modeled by Richards' theory, with or without accounting for a dynamic capillary pressure.

The 3D PLIF-based technique in Chapter 2 can be applied to measure the dynamic contact angle in porous media. The power law model of dynamic capillary pressure proposed in Chapter 4 can be validated by the results of simultaneously measuring the contact angle and the velocity of the water front in porous media. These data can also be used to determine the power law exponent β and to link the dynamic contact angle to the dynamic capillary pressure. Since temporal resolution will be the critical restriction for this contact angle measurement, the 3D PLIF-based method will have the edge in competing with other noninvansive methods such as microCT.

Bibliography

[1] V. S. Averbakh, S. N. Vlasov, and Yu. M. Zaslavsky. Motion of a liquid droplet in a capillary under the action of static force and an acoustic field. *Radiophysics and Quantum Electronics*, 43(2):142–147, 2000.

[2] I. A. Beresnev. Theory of vibratory mobilization on nonwetting fluids entrapped in pore constrictions. *Geophysics*, 71(6):47–56, 2006.

[3] C. V. Chrysikopoulos and E. T. Vogler. Acoustically enhanced ganglia dissolution and mobilization in a monolayer of glass beads. *Transport in Porous Media*, 64(1): 103–121, 2006.

[4] M. Dong, Q. Fan, and L. Dai. An experimental study of mobilization and creeping flow of oil slugs in a water-filled capillary. *Transport in Porous Media*, 80:455–467, 2009. doi: 10.1007/s1122-009-9374-5.

[5] S.L. Geiger and D.S. Durnford. Infiltration in homogeneous sands and a mechanistic model of unstable flow. *Soil Science Society of America Journal*, 64(2):460–469, 2000.

[6] M. Hilpert. Capillarity-induced resonance of blobs in capillary porous media: analyt-

ical solutions, lattice-Boltzmann modeling, and blob mobilization. *Journal of Colloid and Interface Science*, 309:493–504, 2007.

[7] M. Hilpert. Effects of dynamic contact angle on liquid infiltration into inclined capillary tubes: (semi)-analytical solutions. *Journal of Colloid and Interface Science*, 337:138–144, 2009.

[8] M. Hilpert, G. H. Jirka, and E. J. Plate. Capillarity-induced resonance of oil blobs in capillary tubes and porous media. *Geophysics*, 65:874–883, 2000.

[9] J. R. Hunt, N. Sitar, and K. S. Udell. Nonaqueous phase liquid transport and cleanup 1. Analysis of mechanisms. *Water Resources Research*, 24(8):1247–1258, 1988.

[10] S. Iwata, T. Tabuchi, and B.P. Warkentin. *Soil-water interactions: mechanisms and applications*. Marcel Dekker, New York, 2nd edition, 1995.

[11] B. L. Longino and B. H. Kueper. Effects of capillary pressure and use of polymer solutions on dense non-aqueous-phase liquid retention and mobilization in a rough-walled fracture. *Environmental Science & Technology*, 33(14):2447–2455, 1999.

[12] P. K. Niven and K. Singh. Mobilization and rupture of LNAPL ganglia during freeze-thaw: two-dimensional cell experiments. *Environmental Science & Technology*, 42: 5467–5471, 2008.

[13] K. D. Pennell, G. A. Pope, and L. M. Abriola. Influence of viscous and buoyancy

force on the mobilization of residual tetrachloroethylene during surfactant flushing. *Environmental Science & Technology*, 30(4):1328–1335, 1996.

[14] L. N. Reddi and S. Challa. Vibratory mobilization of immiscible liquid ganglia in sands. *Journal of Environmental Engineering ASCE*, 120(5):1170–1190, 1994.

[15] T. Tabuchi. Infiltration and capillarity in the particle packing [in Japanese]. *Rec. Land Reclam. Res.*, 19:1–121, 1971.

[16] D. A. Weitz, J.P. Stokes, R.C. Ball, and A.P. Kushick. Dynamic capillary pressure in porous media: Origin of the viscous-fingering length scale. *Physical Review Letters*, 59(26):2967–2970, 1987.

Vita

Research and Teaching Experience

- Research Assistant, Johns Hopkins University, 2006-present

  - Research Project: "Enhanced Oil Recovery by Using Seismic Waves"

    We derived an analytical model that describes the frequency response of blobs in a capillary tube to seismic-wave excitation. By using the Planar Laser-Induced Fluorescent (PLIF) and refractive index-matching techniques, we visualized the dynamics of blob interfaces and showed, for the first time, that an oil blob in a porous medium can exhibit resonance. Measurements agreed well with our theory. By exploiting resonance, we can potentially improve EOR methods based upon seismic wave stimulation.

  - Research Project: "The Effect of Contact Angle Hysteresis on Blob Mobilization"

    Our experiments with a pore doublet model showed that a blob can be trapped in a straight capillary tube entirely through contact angle hysteresis. A blob is able to sustain pressure gradients by changing its interfacial shape and its

contact angles at the original contact line position. By exploiting PLIF and tomographic reconstruction techniques, we also developed methods to measure contact angles and mean curvatures in 3D.

  - Research Project: "Dynamic Capillary Pressure in Porous Media"

    We generalized the classical Green-Ampt model to account for a capillary pressure that depends on the capillary number in the form of a power law. Our modified model well describes measurements of capillary pressure versus Darcy velocity as well as infiltration experiments, which cannot be described by the classical Green-Ampt model.

- Teaching Assistant for Applied Mathematics for Engineering, Johns Hopkins University, 2007-2011

- Research Assistant, National Taiwan University, 2003 - 2004

  - Research Project: "Establishment of drought prediction and decision-making risk management for Dan Shui River basin"

- Teaching Assistant, Palau Community College, Aimeliik, Republic of Palau, 2001 - 2002

- Teaching Assistant for Engineering Mathematics, National Taiwan University, 2000

Honors

- Studying Abroad Scholarship, Ministry of Education, R.O.C, Taiwan, 2009-2010
- Travel Grant, GRO, the Johns Hopkins University, 2008
- The Outstanding Award of the Taiwan Youth Oversea Service, 2003
- Research stipend to conduct research for M.S. degree, Taiwan National Science Council, 1999-2001
- Chemical Industrial Union Association Scholarship, Taipei City, 1998

Peer-Reviewed Publications

- Accepted and published
  - S.Y. Hsu, R. Glantz, and M. Hilpert, "Pore-Scale analysis of the effects of contact angle hysteresis on blob mobilization in a pore doublet," *International Journal of Oil, Gas and Coal Technology* (in press)
  - S.-Y. Hsu and M. Hilpert, "Incorporation of Dynamic Capillary Pressure into the Green-Ampt Model for Infiltration," *Vadose Zone Journal*, vol 10, no. 2, p. 642-653, 2011,DOI: 10.2136/vzj2010.0069
  - Tung, C.-P., Hsu, S.-Y., Liu, C.-M. and Li, J.-S., "Application of the Genetic Algorithm for Optimizing Operation Rules Of the LiYuTan Reservoir in Tai-

wan," *Journal of the American Water Resources Association*, Vol.39, No.3, 649-657, 2003, doi: 10.1111/j.1752-1688.2003.tb03682.x

- Under review / in preparation
  - E. Pellichero, R. Glantz, M. Burns, D. J. Mallick, S.-Y. Hsu, and M. Hilpert "Dynamic capillary pressure during water infiltration: Experiments and modeling," *Water Resources Research* (in revision)
  - S.-Y. Hsu, J. Katz, and M. Hilpert, "Theoretical and experimental study of resonance of blobs in porous media" (under review)

Presentations at Conferences

- Hilpert, M., M. Burns, S.Y. Hsu, and E. Pellichero: "Effects of dynamic capillary pressure on water infiltration: experiments and Green-Ampt modeling." Presented at the American Geophysical Union Fall Meeting, San Francisco, CA. December 5–9, 2011.
- Hsu, S.-Y., R. Glantz, and M. Hilpert: "Pore-scale analysis of the effects of contact angle hysteresis on blob mobilization in a pore doublet." 64th Annual Meeting of the APS Division of Fluid Dynamics, Baltimore, MD. November 20–22, 2011.
- Hsu, S.-Y., and M. Hilpert: "Numerical and experimental studies on enhanced mobilization of residual NAPL blobs in porous media by seismic waves." Presented at

the Seventh International Conference for Mesoscopic Methods in Engineering and Science Edmonton, Alberta, Canada. July 12–16, 2010.

- Hsu, S.Y. and M. Hilpert: "Pore-scale study of enhanced mobilization of residual NAPL blobs in porous media by seismic waves." Presented at the American Geophysical Union Fall Meeting, San Francisco, CA. December 15–19, 2008.

- Hilpert, M., and S.Y. Hsu: "Effects of seismic waves on the distribution of two immiscible fluids in porous media: frequency dependence, resonance, and blob mobilization." Invited talk at the 8th International Electrokinetics Conference (ELKIN2008), Santa Fe, NM. May 18–23, 2008.

- Hsu, S. and M. Hilpert: "Numerical and experimental investigation on the mobilization of residual NAPL by seismic waves." Presented at the American Geophysical Union Fall Meeting, San Francisco, CA. December 10–14, 2007.

- Ching-Pin Tung, Shao-Yiu Hsu, Chia-Chung Chang, Application to reservoir operation rule-curves ASCE Conferences EWRI 2004.

- Tung, C. P., Hong, N. M., Chou, C. C., Hsu, S.Y., and Li, J. S, Application of simulated annealing to groundwater parameter zonation, World Water & Environmental Resource Congress, in Orlando, Florida, May 20-24, 2001.

- Ching-Pin Tung, Shao-Yiu Hsu, Chung-Che Tan, Application of simulated annealing to estimate area rainfall, the 11th Hydraulic Engineering Conference, Taipei, 2000.

Computational languages and softwares

LabView, MATLAB, Fortran, Visual Basic, Microsoft Office

Professional Activities: Service and Membership

- Referee for
  - *Journal of Fluid Mechanics*
  - *International Journal of Multiphase Flow*
- Volunteer at the 64th Annual Meeting of American Physical Society Division of Fluid Dynamics
- Member of
  - American Geophysical Union (AGU)
  - American Physical Society (APS)